UNIVERSITY OF CALIFORNIA SAN DIEGO

Novel Materials for Next Generation Lithium Batteries

A dissertation submitted in partial satisfaction of the requirements
for the degree Doctor of Philosophy

in

Materials Science and Engineering

by

Xing Xing

Committee in charge:

Professor Ping Liu, Chair
Professor Renkun Chen
Professor Zheng Chen
Professor Olivia Greave
Professor Tod Pascal

2020

The Dissertation of Xing Xing is approved, and it is acceptable in quality and form for publication on microfilm and electronically:

_____

_____

_____

_____

_____

Chair

University of California San Diego

2020

DEDICATION

I dedicate this thesis to my parents. I hope that this achievement will complete the dream that you had for me all those many years ago when you chose to give me the best education you could.

TABLE OF CONTENTS

LIST OF FIGURES

ACKNOWLEDGEMENTS

First, I would like to express my sincere appreciation and thanks to my advisor and mentor, Prof. Ping Liu. Without his great support and guidance, this dissertation could not have been completed. His advices are invaluable on my research as well as career and life. I would also like to thank my committee members, Prof. Olivia Graeve, Prof. Renkun Chen, Prof. Zheng Chen and Prof. Tod Pascal for their valuable time and comments.

Second, I would like to thank all the present past lab members. Special thanks to Dr. Heedae Lim, Dr. Byoungsun Lee and Dr. Haodong Liu for the tremendous help and inspiring discussions.

In the end, special thanks to my family. Great help and encouraging from my parents and my wife Yiqing Huang have supported me to overcome all the challenges and hardship.

Chapter 2, in full, has been submitted for publication of the material: Xing Xing, Yejing Li, Haodong Liu, Zhaohui Wu, Sicen Yu, John Holoubek, Hongyao Zhou and Ping Liu*, “Lithium-free 3D hybrid anode for all-solid-state batteries" The dissertation author was primary authors of this publication.

Chapter 3, in full, is a reprint of materials published in the following paper: Xing Xing, Yejing Li, Xuefeng Wang, Victoria Petrova, Haodong Liu* and Ping Liu*, “Cathode electrolyte interface enabling stable Li-S batteries" *Energy Storage Materials.*, **2019**, 21, 474-480. The dissertation author was the primary author for the data presented and was the

primary author of this publication. The permissions to reproduce this material were granted by the Elsevier B.V., copyright 2019.

Chapter 4, in part is currently being prepared for submission for publication: Xing Xing, and Ping Liu*, “Long calendar life silicon thin film anode enabled by V_2O_5". The dissertation author was the primary author of this publication.

VITA

Education

2020 Doctor of Philosophy, Material Science and Engineering, University of California San Diego, La Jolla, California

2015 Master of Science, Chemical Engineering, University of California San Diego, La Jolla, California

2013 Bachelor of Science, Applied Chemistry, Tianjin University, Tianjin, China

Publications

1. **X Xing**, Y Li, X Wang, V Petrova, H Liu, P Liu, "Cathode electrolyte interface enabling stable Li–S batteries", *Energy Storage Materials 21, 474-480.*
2. HD Lim, HK Lim, **X Xing**, BS Lee, H Liu, C Coaty, H Kim, P Liu, "Solid electrolyte layers by solution deposition", *Advanced Materials Interfaces 5 (8), 1701328.*
3. HD Lim, X Yue, **X Xing**, V Petrova, M Gonzalez, H Liu, P Liu, "Designing solution chemistries for the low-temperature synthesis of sulfide-based solid electrolytes", *Journal of Materials Chemistry A 6 (17), 7370-7374.*
4. Y Li, X Wang, H Zhou, **X Xing**, A Banerjee, J Holoubek, H Liu, YS Meng, P Liu, "Thin Solid Electrolyte Layers Enabled by Nanoscopic Polymer Binding", *ACS Energy Letters 5 (3), 955-961.*
5. YJ Kim, **X Xing**, DY Choi, CH Hwang, C Choi, G Kim, S Jin, KJ Hwang, J Park, "Study of the photocatalytic properties of bio-mimicked hollow SnO 2 microstructures synthesized with Ceiba pentandra (L.) Gaertn.(kapok) as a natural template", *New Journal of Chemistry 39 (10), 7754-775*8.
6. KJ Hwang, YJ Kim, **X Xing**, Y Youn, YJ Kwon, SD Yoon, SC Kim, WG Shim, "Synthesis of Walnut Shaped V2O3 Particles and Its Photocatalytic Activity for Methylene Blue Degradation Under Visible Light Irradiation", Journal of *Nanoscience and Nanotechnology 20 (7), 4322-4326.*
7. BS Lee, S Cui, **X Xing**, H Liu, X Yue, V Petrova, HD Lim, R Chen, P Liu, "Dendrite suppression membranes for rechargeable zinc batteries", *ACS applied materials & interfaces 10 (45), 38928-38935.*
8. H Liu, X Yue, **X Xing**, Q Yan, J Huang, V Petrova, H Zhou, P Liu, "A scalable 3D lithium metal anode", *Energy Storage Materials 16, 505-511.*

9. BS Lee, Z Wu, V Petrova, **X Xing**, HD Lim, H Liu, P Liu, "Analysis of rate-limiting factors in thick electrodes for electric vehicle applications", *Journal of the Electrochemical Society 165 (3), A525.*
10. C Liu, H Wang, **X Xing**, Y Xu, JA Ma, B Zhang, "Selective C4–F bond cleavage of pentafluorobenzene: synthesis of N-tetrafluoroarylated heterocyclic compounds", *Tetrahedron Letters 54 (35), 4649-4652.*
11. H Liu, H Zhou, BS Lee, **X Xing**, M Gonzalez, P Liu, "Suppressing lithium dendrite growth with a single-component coating", *ACS applied materials & interfaces 9 (36), 30635-30642.*
12. H Liu, Z Zhu, Q Yan, S Yu, X He, Y Chen, R Zhang, L Ma, T Liu, M Li, R Lin, Y Chen, Y Li, **X Xing**, TJ Choi, L Gao, HSY Cho, K An. J Feng, R Kostecki, K Amine, T Wu, J Lu, H L Xin, SP One, P Liu, "A disordered rock salt anode for fast-charging lithium-ion batteries", *Nature 585 (7823), 63-67.*

ABSTRACT OF THE DISSERTATION

Novel Materials for Next Generation Lithium Batteries

by

Xing Xing

Doctor of Philosophy in Materials Science and Engineering

University of California San Diego, 2020

Professor Ping Liu, Chair

Lithium-ion batteries are one of the most promising energy storage devices for their light weight and superior cycling stability. However, the state-of-the-art lithium-ion batteries cannot satisfy the ever-increasing market demand of high energy density electrochemical energy devices. Advanced lithium batteries based on novel electrode materials could provide higher energy density thus become a hot research topic.

This dissertation will discuss the designs and applications of novel electrode materials to address the performance challenges for different types of energy storage devices. Chapter 2 provides a new strategy to fabricate a “lithium-free” all-solid-state battery. The 3D hybrid anode design improves the cycling stability of all-solid-state batteries by overcoming the commonly observed cell failure due to the electrode volume change and lithium dendrite growth. This design provides a promising approach towards a high energy density, long life, and low-cost all-solid-state battery technology. In Chapter 3, a concentrated ether-based electrolyte with LiTFSI and $LiNO_3$ as co-salts is proposed, which enables stable cycling of a Li-SPAN battery. In addition to providing excellent protection for lithium metal anodes by forming the solid electrolyte interface (SEI), the electrolyte promotes the formation of a crystalline cathode electrolyte interface (CEI) on the SPAN surface composed of LiF and $LiNO_2$. The CEI effectively prevents the formation of soluble polysulfide species and enables stable cycling of the Li-SPAN batteries. In Chapter 4, a V_2O_5-Si multi-layer composite anode is proposed and fabricated. The mixed conductive V_2O_5 layer effectively confines the volume change of Si layer and prevents the parasitic reactions between Si and electrolyte. This strategy enables the anode a long cycle life as well as a long calendar life while maintaining high energy density.

Chapter 1: Introduction

1.1 Energy storage

Global demand for energy is increasing rapidly with the growth of population today[1–8]. However, energy production/consumption which rely on the combustion of fossil fuels has a severe impact on the human society and world ecology. Renewable energy production is the anticipated solution to this problem as an alternative energy source since the energy consumption is designed to be more sustainable and more environmentally friendly. However, the mismatched demand and supply due to their intermittent nature is the major challenge. Energy storage technologies are the solution to overcome this challenge[9–15], including electrochemical devices, pumped hydro, compressed air, etc. Among them, batteries are the most suitable and potential cost-effective options to sustain renewable energy systems[16–21].

Different types of battery energy storage technologies have been developed and used in different fields. The selection of the type depends on the nature of the application, including energy density, power, and cost. Compared with traditional battery technology, lithium-ion batteries have the capability to charge faster, last longer, and have a higher power density in a lighter package[22,23]. Therefore, lithium-ion batteries become the fastest growing and most promising battery chemistry in development and promotion of electrical vehicles (EVs), the energy grids and portable electronic devices.

The lithium-ion battery functionality is based on the lithium-ion movement between the positive and negative electrodes. Positive electrodes release the lithium ions

to the negative electrode through the electrolyte during charging, which happens in opposite direction when the battery is discharging. In general, commercial lithium-ion batteries use an intercalated lithium compound as the active material at the positive electrode and typically graphite as negative electrode material.

Over the past 25 years, the specific energy of electrode materials in commercial lithium-ion batteries has steadily increased. However, the modern market demands an even higher specific energy, to 500 Wh kg^{-1} at cell level[24]. At present, many approaches are being pursued in developing next-generation long-life batteries, such as lithium-sulfur batteries and lithium-oxygen batteries. All the technologies have their own advantages and challenges. In this dissertation, the research mainly focuses on all-solid-state batteries, lithium-SPAN (sulfurized polyacrylonitrile) batteries, and silicon anode material optimizations.

1.2 All-solid-state batteries

Lithium-ion batteries have revolutionized the energy storage technology market and enabled the ever-increasing use of portable electronic devices and EVs. However, current lithium-ion batteries with intercalation electrodes and liquid electrolyte reach a specific energy of 260 Wh kg^{-1} on the cell level and will approach the theoretical limit in few years. Lithium metal anodes are considered to be the ultimate solution for high energy density batteries with its gravimetric (2061 mAh cm^{-3}) and volumetric capacity (3860 mAh

g^{-1})[14,15]. However, cells with lithium metal and liquid electrolyte are facing dendrite growth and poor cycling coulombic efficiency (CE) problems.

The recent discovery of new types of highly lithium-ion conducting solid-state electrolytes (SSEs) has triggered a surge of interest in all-solid-state batteries (ASSBs). in addition, SSEs seem to be more promising to enable application of lithium metal anode by mechanically suppressing lithium dendrite growing. Thus, the application of SSEs by replacing the liquid electrolyte in the lithium batteries might provide an alternative pathway to satisfy the demand for higher energy density, longer cycle lives and acceptable safety properties[7,15,16,20,24].

The concept of solid-state ionic conductor began in 1830s, when Faraday discovered the conduction property of heated solid Ag_2S and PbF_2[25]. The first lithium-ion conductor Li_3N wtith a high ionic conductivity of 10^{-3} S cm^{-1} at room temperature (RT) was discovered in 1950s, which were extensively exploited for ASSBs[26]. In 1960s, a fast 2D solidum-ion-transport phenomenon was discovered in alumina, which was utilized in the later development of sodium-sulfur batteries. Solid polymeric ionic conductor appeared in 1973 and the scope of solid-state ionic was no longer limited to inorganic materials, when Fenton et al. found that polyethylene oxide (PEO)-based complexes were alkali-metal conductive[27]. Sulfide-type solid ionic conductors were first reported in 1986. In 1992, lithium phosphorus oxynitride (LiPON) was fabricated as a thin film-type ionic conductor in Oak Ridge National Laboratory. The next year, Inaguma et al. discovered

the high conductivity of more than $2*10^{-5}$ 10^{-3} S cm^{-1} at RT in perovskite-type $Li_{0.5}La_{0.5}TiO_3$ (LLTO)[28]. Later, in 1997 NASICON-type SSEs including $Li_{1+x}Al_xGe_{2-x}(PO_4)_3$ (LAGP) and $Li_{1+x}Al_xTi_{2-x}(PO_4)_3$ (LATP) were reported by Fu. A Garnet-type fast ionic conductor of $Li_7La_3Zr_2O_{12}$ (LLZO) was developed by Murugan et al. in 2007. Its $3*10^{-4}$ S cm^{-1} conductivity at RT and good chemical and thermal stability provides more opportunities in ASSBs[29]. In 2011, Kanno et al. developed a superionic conductor of $Li_{10}GeP_2S_{12}$ (LGPS), which delivers $1.2*10^{-2}$ S cm^{-1} conductivity at RT[30].

The development of high bulk ionic conductivity SSEs is expected to lead to emerging applications of ASSBs. In 2014, a ASSB using LiPON SE with $LiNi_{0.5}Mn_{1.5}O_4$ (LNM) cathode and lithium metal anode was fabricated in Dudney's group[31]. Later, Li/LGPS/LNM ASSB at RT was reported by Kanno et al., which showed an initial discharge capacity of 80 mAh g^{-1} with an average voltage of 4.3 V[32]. In 2018, Wang's group developed a Li/LLZO/$LCoO_2$ ASSB and showed an highly improved cycling performance[33]. In 2020, Samsung reported a ASSB with Ag-C composite as anode exhibiting the best cycling performance with highest Coulombic efficiency (CE) to date, which is an important step to practical use of ASSBs[34].

However, towards industrial commercialization, more investigations are in demand to further address the fabrication challenges and interface instability problems. The main fabrication challenges including the thin SSE layer fabrication and poor interfacial contact hinder the improvements on cell-level energy density in ASSBs. Various SSE fabrication

methods were designed and attempted to solve these problems and achieved great progresses, including solution processing[35,36] and mechanical property improvements[37–39].

In addition, due to large volume change of lithium plating/stripping and lithium dendrite growth, the improvements of the interface stability are also needed to achieve reversible, low-resistance and stable interfaces between SSE and lithium metal anode. There are strategies reported to bypass this interface instability to achieve a better ASSB performance. Firstly, an interlayer between electrode and anode, which is stable with mixed ion and electron conductivity, could guide the lithium plating/stripping behavior and achieve stable cycling performance of the ASSB[40,41]. Secondly, a lithium-rich solid solution/alloy could completely change the transport inside the anode and highly affect the interface stability[34,42]. Thirdly, a 3D microstructure anode design, which moves the lithium plating/stripping position away from the interface, can mitigate the short circuit problem and prevent the interface instability[38,43].

In order to achieve commercial viability, the key AASB research targets can be quantified: < 40 Ohm/cm^2 internal resistance, < 50 μm thick SSE, > 5 mAh/cm^2 areal capacity and 500 Wh/kg energy density. Realizing these targets is difficult, but once achieved, will transform our energy future.

1.3 Lithium-SPAN batteries

Rechargeable lithium-sulfur batteries have recently received tremendous attention due to their high theoretical energy density (2600 Wh kg^{-1}) and low cost with abundant natural resources, which shows the promising potential to further improve the cell level energy density of lithium-ion batteries[44–47]. However, the commercialization of lithium-sulfur batteries is hindered by several major problems[39,48–65]. First, both elemental sulfur and discharge product lithium sulfide are intrinsically poor electrical and ionic conductors, causing a low active material utilization and poor rate performance. Second, the dissolution of long-chain lithium polysulfides in organic electrolyte results in fast capacity decay and poor CE[45–47,66].

Sulfurized carbon as a class of sulfur contained cathode material attracted considerable interest in overcoming the drawbacks of elemental sulfur cathode and developing high energy density batteries. Among the numerous candidates, sulfurized polyacrylonitrile (SPAN) has been the most intensively studied with its low synthesis cost and excellent cycling performance[67–73].

The synthesis of SPAN was first reported by Wang's group in 2002[67]. A mixture of elemental sulfur and polyacrylonitrile (PAN) was heated at ~300 degree Celsius and in argon environment for hours to gain SPAN powders. This work was followed by other groups in investigating the structural characterization, the optimization of synthesis condition and the applications in various electrolyte systems[74–82].

However, the chemical structure has not been fully understood. During heating, PAN polymer backbones are dehydrogenated by losing hydrogen sulfide molecules. The resulting carbon double bonds after cyclization are easily sulfurized/vulcanized at elevated temperature[53,64,65]. This process turns out that PAN polymer pyrolysis mechanism is clear, but the state of sulfur in SPAN is not. Based one Raman and Fourier transform infrared spectroscopy (FTIR) analysis, the S-S bond and C-S bond are clearly observed in SPAN, and CNS^- fragment is also found by time-of-flight secondary ion mass spectrometry (ToF-SIMS). In thermogravimetric analysis (TGA), sulfur in SPAN cannot be completely removed even at 800 degree Celsius, which provide the evidence that sulfur is covalently bonded. After all these characterizations and analysis, we can construct that the short sulfur chain is covalently bonded to the cyclized and dehydrogenated PAN backbones through C-S and N-S bonds[83]. However, more evidence is needed to determine the exact chemical structure of SPAN.

Due to the chemical structure of SPAN, its electrochemical mechanism is fundamentally different from conventional lithium-sulfur batteries. In the first discharge, a significant voltage polarization (hysteresis) and large amount of irreversible capacity can be observed. Then, it shows a slightly sloped voltage plateau in the following discharge and charge processes, unlike lithium-sulfur batteries, while with excellent cyclability in carbonate-based electrolyte with 500-700 mAh g^{-1} specific capacity[61,83–85]. For further

development of this promising material, it is essential to identify the electrochemical properties of lithium-SPAN batteries.

Despite the unclear chemical structure and electrochemical mechanism of SPAN, the superior performances are verified and optimized by various groups. By improve the electrically conductive network, hundreds of stable cycles of SPAN cathode when paired with excess lithium were reported. While it is highly desirable to employ SPAN as the cathode material, the use of carbonate-based electrolyte creates significant stability issues at lithium metal anode. More efforts are needed to identify a proper electrolyte system which is suitable for both cathode and anode. FEC containing carbonate electrolyte and DBE based ether electrolyte were proposed to improve the cycle life of SPAN with limited lithium source[86]. Recently, Liu's group reported an excellent lithium-SPAN battery with over 900 cycles and 99.37% CE, which exhibited the best cycling performance to date[87].

After 18 years of research, SPAN has become a very promising cathode material candidate nowadays, targeting a 500 Wh kg^{-1} battery[20]. There are remaining challenges, including chemical structure, electrochemical mechanism, and cell level optimization on electrodes and electrolyte, but the promise of fabricating low cost and long cycle life lithium-ion batteries will be realized in the near future.

1.4 Silicon anode material

In the last two decades, lithium-ion batteries are considered to be an ideal energy storage device due to their high energy density and long cycle life, thus extensively applied in portable electronic devices, the energy grid and EVs. However, current lithium-ion battery technology can not satisfy the energy and power demand from current and future applications. Conventional commercial graphite anode, with a moderate theoretical capacity of 372 mA h g^{-1}, hardly meets the requirement of building a 500 Wh kg^{-1} battery. Therefore, developing higher energy density anode material is imperative for next generation batteries[40,88–92].

Among all the anode material, silicon has attracted most interest from researchers due to the following reasons[93–95]. Silicon possesses the highest theoretical specific capacity (4200 mA h g^{-1}, lithiated to $Li_{4.4}Si$), which is more than tenfold of the graphite anode material. Moreover, silicon exhibits an appropriate low discharge voltage at 0.4 V vs Li^+/Li. Third, silicon is cheap and abundant as the second richest element in earth crust. More importantly, it is also non-toxic and environmentally friendly[95–98].

However, the commercial application of silicon is hindered by the poor cycling stability due to the drastic volume expansion (~360% for $Li_{4.4}Si$), which causes series of severe destructive consequences[99–105]. First, particle pulverization compromises the integrity of the electrode material structure during cycling. Second, delamination happens in the conductive pathway induced by the interfacial stress. Third, there is continuous

electrolyte consumption during the SEI breaking and reforming. All these processes accelerate electrode structure collapse and capacity fading.

Strategies have been proposed by researchers to improve the silicon anode cycling performance, including size reduction and sophisticated structure control[102,103,106,107].

Generally, shifting silicon anode material size from bulk-scale to nano-scale is the most effective strategy to improve the cycling performance[108–111]. As reported, when the size of silicon is lower than the critical limit, it can fully relive the stress caused by lithiation and even maintain integrity without pulverization. The critical size limitation is about 150 nm for crystalline silicon and 870 nm for amorphous silicon. Based on this theory, 1D silicon nanowires or nanotubes have been developed which exhibited an improved cycling performance.

Sophisticated microstructure control of silicon is the other interest which attracted much attention[112–115]. In the past decades, thin-film engineering has played an important role to clarifying the stress evolution, which also has been applied into silicon anode. The patterned thin-film silicon reported by a few groups shows superior rate capability and stability. Porous structure is also considered as another effective strategy to alleviate the volume variation during cycling. Zhang's group proposed the synthesis method for porous silicon/carbon composite with 2-5 micrometer pores, which delivered 0.15 % capacity fading rate for 100 cycles. Shape-preserving shell structure attracts attention in silicon anode research as well. Liu's group developed yolk-shell design comprising a silicon nano

particle yolk and a 5-10 nm thick carbon shell, which shows excellent cycling stability for 1000 cycles.

Besides the volume change related problems of silicon, the calendar life related problems have been unveiled in the past few years. Lu's group investigated the calendar life and cycle life of SiO anode and discovered that the SiO anode capacity fading is time-dependent instead of cycling-number-dependent[101,116]. The parasitic reactions between anode and electrolyte are considered to be responsible for it, which need to be addressed for practical application of silicon anode.

After the major failure mechanisms of repaid capacity decay being well understood, an enhanced cycling performance improvement is possible. The efforts regarding the cycle life and calendar life have certainly made tremendous progress. It is expected that the continuous development of these key aspects of silicon material will accelerate the practical applications of silicon-based lithium-ion batteries.

Chapter 2: Lithium-free Hybrid Anodes for All-solid-state Batteries

2.1 Introduction

All-solid-state batteries (ASSBs) have emerged as promising next-generation batteries due to their potential to provide high energy density and enhanced safety[17,66,74,117–122]. Utilization of Li metal as the anode in ASSBs is the ideal choice as it has a high theoretical specific capacity (3860 mAh g^{-1}) and a low potential (-3.04 V vs standard hydrogen electrode [SHE]). However, challenges remain with regard to the stability of the Li metal anode, such as dendrite formation and large volume changes during cycling, which result in mechanical degradation at the interface between the anode and solid-state electrolyte (SSE)[5,6,8,14,123–125]. This degradation not only contributes to a significant reduction of cell life, but also leads to potential cell internal short circuits[126–130]. Strategies have been developed to analyze and resolve the interface issues caused by Li metal anode, such as adding self-healing component into SSE, softening SSE with polymers, engineering of interlayers, and rational control of Li metal deposition based on theoretical studies[5,8,9,13,21,35,38,123,131–141]. One particularly promising approach is to apply a 3D anode network, which hosts the deposited lithium metal, mitigates dendrites growing towards the SSE, minimizes the volume change, and helps maintaining the integrity of the interface[36,38,64,120,122,125,132,142–144].

3D anode as a Li metal host is a widely explored concept in liquid electrolyte batteries. The 3D design effectively mitigates the significant volume change of Li metal

during cycling[132,145]. However, unlike liquid cells where electrolytes can flow into the 3D network and conduct ions, it is difficult to extend these anode networks into ASSBs while maintaining ionic conducting pathways. An early example is the use of a porous garnet SSE as a 3D ionic framework for Li metal deposition[125,143]. The large contact area between Li metal and garnet SSE reduces local current density at the interface, producing a small overpotential and homogeneous Li metal deposition. The electronic pathway relies on lithium metal itself since the SSE network has no electronic conductivity. Various types of nickel foam and carbon matrix have also been examined as Li metal anode hosts, which improved the interfacial stability by maintaining anode structure during cycling[5,8,13,14,21,119,137]. However, these hosts, while electronically conducting, have limited to negligible ion conductivities. As a result, Li metal plating and stripping, which requires ion transport, needs to be initiated at the electrolyte interface where the formation of dendrites is still detrimental[8,123,124,143,146]. An ideal host is a mixed conducting 3D anode network that will effectively shift Li deposition away from the interface, thus extend cell cycle life[140].

We report here a 3D mixed conductive anode network composed of a mixture of lithiated graphite and LPS (Li_3PS_4, lithium thiophosphate) SSE, which is extremely easy to fabricate. Graphite, which is cheap and abundant, has demonstrated long cyclability with little volume change in all solid-state Li-ion batteries[135,138,146–148]. After lithiation, the product LiC_6 is thermodynamically stable with Li metal and has both electronic

conductivity and ionic conductivity. Moreover, LiC_6 is shown to be lithiophilic and can facilitate Li metal deposition[146,149,150], making it a desired material for 3D anode network in ASSBs. LPS SSE, with low Young's (~20 GPa) and shear (~7 GPa) elastic moduli can be densified at low temperature by mechanical compression, a distinct advantage over oxide-based electrolytes[11,135,151]. The 3D mixed conductive anode network is simply prepared by mixing graphite and LPS. Controlling the degree of compression generates electrodes with desired residual porosities. After uniformly distributing extra Li metal into the voids, a 3D graphite-lithium hybrid anode can be realized.

The other feature of the current work is the employment of a "lithium-free" design, in that the cell is fabricated as a conventional solid-state lithium-ion battery with $LiNi_{0.85}Co_{0.10}Al_{0.05}O_2$ (NCA) as the cathode and graphite as the anode. We gradually reduce the amount of graphite anode to intentionally induce lithium metal deposition, thus forming the hybrid graphite/lithium metal 3D anode. Such an approach enables an assessment of lithium cycling efficiency due to the limited amount of active lithium. In addition, the approach is compatible with a manufacturing process identical to that of solid-state lithium-ion batteries, enabling a gradual transition to solid state lithium metal batteries.

2.2 Experiment section

Materials and synthesis

All chemicals were purchased from Sigma-Aldrich unless specified and used without purification. All the cell fabrications and testing were performed inside Argon-filled glove box (MBRAUN, MB200B, H_2O < 0.5 ppm, O_2 < 0.5 ppm). High purity LPS powder was purchased from the NEI corporation (USA) and used as-is.

Anode composite: Graphite/LPS anode composite were prepared with graphite and LPS powder in a ratio of 1:1 by weight. The mixture was hand ground with an agate mortar for 20 minutes to make a homogeneous composite.

Cathode composite: A solution method was employed to coat $LiNbO_3$ on NCA particles. First, lithium ethoxide and niobium ethoxide were dissolved in anhydrous ethanol. NCA powder was then added into the solution and stirred for one hour. The dried powder was collected by evaporating the ethanol using a rotary evaporator followed by heat-treatment of the powder at 450 ℃ for one hour, yielding $LiNbO_3$ coated NCA. The coated powder was dried overnight at 100℃ under vacuum before transferring to the inside of the glove box for storage and fabrication of solid-state batteries. Then, NCA cathode composite was prepared with coated NCA, LPS, vapor growth carbon fiber (VGCF) in a ratio of 70:28:2. All components were hand ground to make a homogeneous mixture.

Characterizations and electrochemical analysis

The morphologies of the cycled anode were characterized using scanning electron microscopy (FEI Quanta 250 SEM) coupled with an energy dispersive X-ray spectrometer

(EDX) to determine the chemical composition of the samples. The samples were tested under 10 kV and 0.1 nA conditions. The cross-section images were collected using focused ion beam-scanning electron microscopy (FIB-SEM, FEI Scios, Scios DualBeam operating at 5 kV and 0.1 nA conditions. The cross-sections were first cut under 30 nA, followed by 0.1 nA surface cleaning process. All the samples were prepared inside an Ar environment glove box and sealed inside a bag made of aluminum laminate sheets. During quick transferring, the samples was briefly exposed to air.

The samples for XPS were prepared, cycled and loaded onto the XPS (PHI Quantera SXM) stage in an Ar environment glove box. The samples were transferred with a sealed bag made of aluminium laminate sheets (MTI) filled with argon. They were quickly transferred into the XPS (PHI Quantera SXM) instrument to minimize the air exposure. The samples were carried out using an Al K alpha (1486.6eV) source at 15 kV under a $<10^{-8}$ tor ultra-high vacuum condition. All the results were processed by CasaXPS and calibrated based on the adventitious carbon at 284.8 eV. All XPS measurements were collected using a charge neutralizer during acquisition. Survey scans were collected with a 1.0-eV step size and were followed by high-resolution scans with a step size of 0.125 eV for the C 1s, O 1s, Li 1s regions.

The electrolyte pellets were prepared using a 13 mm custom-made polyether ether ketone (PEEK) die mold and titanium (Ti) plungers. LPS electrolyte powder (150mg) was pressed at 400 MPa for 3 minutes with a hydraulic press inside the mold to get a ~800 μm

thick electrolyte pellet. Then, certain amount of cathode and anode materials were filled on both sides of the pellet and pressed at 400 MPa to get a three-layered pellet. Two Ti plungers were used as current collectors while the full cell was measured under a 90 MPa stacking pressure.

All the galvanostatic charge/discharge tests were inside a 35 °C oven, using LAND battery testers (Wuhan, China). The critical current density tests of Li-LPS-Li cell and 3D-LPS-3D cell were conducted with a 0.1 mA cm^{-2} increase each cycle until the cell short. The time for each charge and discharge process is 1 hour. For Li-Cu and Li-3D half-cell tests, the cell areal discharge capacity was fixed with a certain value, but cell charge process was controlled by voltage cut-off (1 V) to study the Coulombic efficiency of Li plating and stripping. The NCA-Cu and NCA-3D cells were conducted in a voltage range of 2.5 – 4.3 V vs. Li/Li^+ at room temperature with a current density of 0.1 mA cm^{-2}. Electrochemical impedance was measured using electrochemical impedance spectroscopy (EIS, BioLogic, VMP300t) in a frequency range from 7 MHz to 100 mHz.

2.3 Results and discussion

The design of a solid-state battery with a 3D lithium-graphite hybrid anode is schematically shown in Figure 2.1. When Li metal foil is used as the anode (Figure 2.1a), due to its volume change during cycling, the interface between the anode and the SSE layer

has to shift in the cell. Moreover, uneven Li metal deposition results in dendrites which can penetrate into the SSE layer, causing short circuits. In contrast, a 3D mixed conducting anode network composed of graphite and LPS SSE is shown in Figure 2.1b. During charge, after graphite is fully lithiated, lithium metal plates into the voids inside the 3D network, which is both electronically and ionically conducting. By shifting lithium metal deposition away from the interface between the anode and SSE, the interface maintains its integrity without reduced dendrite formation with cycling, resulting in an improved cycle performance.

To demonstrate the necessity of LPS SSE as the ion conductor in the anode network, a pure graphite anode with no LPS was tested in a half cell with a lithium metal counter electrode. The voltage profile in Figure 2.7 shows that after full lithiation of graphite and the voltage reached 0 V, an additional 1 mAh cm^{-2} of Li metal was deposited. To examine the Li metal distribution, the cell was disassembled and examined under scanning electron microscopy (SEM). Figure 2.7c shows an area where the electrolyte layer is partially removed in order to reveal the underlying graphite anode. Energy-dispersive X-ray spectroscopy (EDX) mapping (Figure 2.7d) shows that island features represented by the dashed white lines are rich in oxygen but with no other elements (C, P, and S). The high concentration of oxygen is usually correlated with lithium metal (absorbed during sample transfer). It is evident that Li metal was deposited at the interface between graphite and SSE. To examine whether lithium also deposits in the bulk of the graphite anode, the anode

surface was gently scratched to reveal the underlying layer (Figure 2.7b). While the top surface has a golden color, which is attributed to LiC_6[14,135,145,146,152], the underlayer appears to be black, indicative of poor lithiation due to a lack of ion conductivity (all lithium ions have to be transported through graphite itself). We thus conclude that pure lithiated graphite does not have sufficient ion conductivity to allow complete lithiation of the graphite layer and guide lithium metal deposition away from the anode/electrolyte interface.

We next examine the advantage of the 3D graphite/LPS host in preventing cell short circuit in terms of maximum lithium deposition capacity and cycling current (Figure 2.2). Figure 2.2a compares the voltage profiles of the Li/LPS/3D anode cell as compared to a baseline Li-Cu cell when lithium was continuously deposited until the cells experienced short circuit. The Li-Cu cell hard shorted after only ~2.2 mAh cm^{-2} of lithium was deposited. However, the 3D anode cell did not short after 3 mAh cm^{-2} of lithium deposition. We estimated the porosity of the 3D anode to be ~41% based on graphite mass loading (1.7 mg cm^{-2}) and electrode thickness (30 μm) observed by SEM in Figure 2.2b; a complete filling of the pores corresponds to ~3 mAh cm^{-2} capacity. The inflection point at ~0.5 mAh cm^{-2} on the discharge voltage profile of the 3D anode cell implies the end of graphite lithiation and the start of lithium metal plating.

Critical current density, defined as the maximum current density when cell shorting occurs, was measured to examine the effect of the 3D host. As shown in Figure 2.2d, for a

Li/LPS/Li symmetric cell, the short circuit occurred at 0.4 mA cm^{-2}. Each step is 30 min and the increment of current density at each step is 0.1 mA cm^{-2}. This is comparable to previously reported values[153,154]. To test the effectiveness of the 3D anode, a Li/3D/LPS/3D/Li cell was fabricated. As shown in Figure 2.2b, before critical current density test, 3 mAh cm^{-2} lithium metal capacity was first stripped from the left lithium chip and deposited into the 3D graphite region on the right through LPS SSE, followed by 1.5 mAh cm^{-2} lithium metal capacity being stripped back to the left 3D graphite electrode to fabricate a symmetric 3D hybrid graphite/lithium anode cell. The critical current density of the symmetric 3D anode cell was 1.4 mA cm^{-2}, when the cell showed signs of a soft short (Figure 2.2c). The significant improvement compared to a planar Li metal electrode provides further evidence of the benefit of the 3D anode to enhance battery stability.

SEM has been applied to examine the lithium deposition morphology. As shown in Figure 2.8, after 1 mAh/cm^2 lithium metal deposition on planar Cu, a lithium metal film was clearly observed between SE and Cu. Moreover, spike-shaped lithium penetrating into LPS SE was observed. After removing the top LPS SE layer, the morphology of lithium metal is shown in Figure 2.8b. The deposited lithium metal with various thickness are non-uniformly distributed on the surface of Cu, while some areas show bare Cu surface. As a comparison, we also disassembled the 3D anode cell after 0.5 mAh cm^{-2} of lithium metal deposition after graphite lithiation. SEM images of a tilted cross-section along with EDX mapping are shown in Figure 2.9a and 2.9b, respectively. The cross section is between the

two marked dashed lines, and the current collector side of the 3D anode is above the upper dashed line. In the EDX mapping images shown in Figure 2.9, the P and S signals represent the LPS SSE, and the carbon signal represents the lithiated graphite. The uniform distribution of lithiated graphite and SSE in the anode network are clearly observed. Similar to the analysis of Figure 2.7, the oxygen signal represents the summation of lithiated graphite and lithium metal due to brief exposure to air during sample transfer. We attribute the region with strong oxygen signals but weak carbon signals to metallic lithium.

To further verify this hypothesis, focus ion beam (FIB)-SEM has been applied to examine the cross-section as shown in Figure 2.3. The image for a fully lithiated graphite electrode but without further lithium metal deposition is shown in Figure 2.3a. The relatively dark region reflects a higher electronic conductivity, which are attributed to either lithiated graphite or lithium metal, and the relative light region represents the LPS solid electrolyte. In EDX mappings shown in Figure 2.3b, the S signals clearly represent LPS solid electrolyte, which is consistent with the light regions shown in SEM images, and the C signals represent lithiated graphite, which match well with the dark regions in the SEM. No lithium metal was founded in this electrode. In comparison, Figure 2.3c and 2.3d show the results for the over-lithiated 3D anode. The area with C signals in the EDX mapping is smaller than the dark region in SEM images. The rest of the dark region corresponds to strong O signals, which is attributed to lithium metal. Note that such methodology of identifying lithium metal has been previously reported. We thus conclude that the lithium

metal is deposited on the surface of lithiated graphite, which is uniformly distributed throughout the 3D electrode.

We also applied X-Ray Photoelectron Spectroscopy (XPS) to further examine whether the oxygen signal in the over-lithiated sample was indeed due to Li metal oxidation after air exposure. XPS is very sensitive to the air exposure since it can only probe the composition of ~10 nm near the surface[155]. The spectra in Figure 2.10 demonstrate that the over-lithiated 3D electrode sample has a much higher oxygen and Li signal compared to the pristine 3D anode (the anode only contains graphite and LPS). The atomic ratio for Li had been enhanced from 17.8% (pristine) to 31.7% (over-lithiated) while the O ratio had been increased from 4.0% (prostine) to 9.8% (lithiated). The Li ratio increase is attributed to the lithium metal deposition. Since there is no O element in our materials, the origin of O signal can only be attributed to the air exposure-induced adsorption and reaction. The high resolution XPS results for the pristine and over-lithiated anode further support this conclusion, which had been discussed in supporting information, Figure 2.10. These results support the conclusion that the accumulated SEM-EDX O signal in Figure 2.3d, is from the deposited lithium metal which had been oxidized in the ambient air environment.

To further understand the mechanism of lithiated graphite for facilitating 3D lithium metal deposition, we also investigated alternative materials as anode host. As shown in Figure 2.11, an LTO-based 3D anode host was fabricated and tested with a same cell configuration. LTO was chose since it is known to be stable at 0 V. after over-lithiation,

lithium metal particles were observed at the 3D anode/electrolyte interface, but no lithium metal was found inside the 3D LTO host. A plausible explanation is that lithiated graphite is much more lithiophilic than LTO[149,156], a quality that is essential for the success of the 3D anode concept.

The effect of lithium deposition and stripping capacity per cycle on the cycle life and coulombic efficiency (CE) of Li-Cu cells and Li-3D anode cells was examined next. As shown in Figure 2.4a, at a plating capacity of 0.25 mAh cm^{-2}, the Li-Cu cell only lasted 22 cycles with an average CE of ~ 91%. The CE is comparable to previously reported values and reflects the side reactions between LPS SSE and Li metal[11,136,153,154,157]. At the 22nd cycle, there is a clear hard short during lithium deposition, as evidenced by the sudden drop of cell voltage to 0 V. Increasing lithium deposition capacity to 0.5 mAh cm^{-2} and 0.75 mAh cm^{-2} results in hard shorts in 16 cycles and 8 cycles, respectively. However, with 3D anodes, the cell life was significantly extended in the same tests. As shown in the voltage profiles in Figure 2.4b-d, the graphite anodes were first fully lithiated and de-lithiated to confirm the graphite capacity. The electrode is then lithiated with a capacity beyond the storage capacity of graphite in the form of lithium metal. To facilitate comparison with the baseline Li-Cu cells, the lithium metal capacity is chosen to be 0.25, 0.5, and 0.75 mAh cm^{-2} as well and the corresponding anode specific capacities normalized to the weight of graphite are 382, 479, and 864 mAh g^{-1}, respectively. Figure 2.4b shows the results from the 3D anode with a total capacity of 0.75 mAh cm^{-2} where 0.5 mAh cm^{-2}

is attributed to lithium storage in graphite while 0.25 mAh cm^{-2} as lithium metal. This cell cycled for more than 60 cycles without shorting, in contrast to the 22 cycles for the Li-Cu cell with the same 0.25 mAh cm^{-2} lithium metal capacity. Moreover, the average CE also increased to >94%. Likewise, 3D anodes with lithium metal capacities of 0.5 mAh cm^{-2} and 0.75 mAh cm^{-2} were cycled for more than 40 cycles without shorting, a vast improvement over their Li-Cu baseline counterparts. (Figure 2.4c, d). The highly improved cycling performance demonstrates the positive effects of hybrid anode on electrochemical cycling stability.

Post-mortem analysis was performed on the cell corresponding to the data shown in Figure 2.4b in order to understand its degradation mechanism. Figure 2.13 shows the cross-sectional SEM image for the cell after 20 cycles and the anode is in lithiated state. Based on the EDX mapping images shown in Figure 2.13b and 2.13c, we concluded that the lithium and graphite distribution remained uniform as a 3D composite, similar to the results shown in Figure 2.2b before extended cycling. However, the electrochemical impedance spectroscopy (EIS) results shown in Figure 2.14 provided a plausible explanation for the cell degradation. In Figure 2.14a, a Li/LPS/Li symmetric cell was tested first to understand the Li/LPS interface behavior after cycling. The semi-circles shown in Figure 2.14a correspond to the bulk electrolyte impedance and the interface impedance between LPS and lithium. After 20 cycles, as the fitted values shown in Figure 2.14a, the R_{bulk} increased from 1000 Ohm to 1641 Ohm and the $R_{interface}$ increased from 166.9 Ohm

to 525.4 Ohm, implying the instability of LPS vs lithium. Results for the Li/3D cell are shown in Figure 2.14b. Again, the semi-circle corresponds to bulk electrolyte impedance and the interface impedance between LPS and both electrodes, while the low frequency feature is attributed to the Li^+ diffusion process in the 3D anode[158,159]. After 20 cycles, the R_{bulk} increased from 1079 Ohm to 2156 Ohm, and $R_{interface}$ increased from 29.4 Ohm to 465.2 Ohm. The diffusion tail also bended down, implying the Li^+ diffusion in 3D anode appeared to have deteriorated after cycling. As reported previously, the stability of LPS vs Li metal is the likely reason for both electrolyte bulk impedance and the interface impedance increase and slower diffusion[47,70,122,158–160].

The 3D anode is then employed to construct all solid-state full cells with $LiNbO_3$ coated NCA as the cathode[161–163]. A Cu-NCA cell is used as the control for comparison. Note that both configurations are "lithium free" with no pre-lithiation of the anode. Previous reports have shown that the $LiNbO_3$ coating greatly improves the compatibility between NCA and the LPS electrolyte. Figure 2.15 show SEM and EDX analysis of the coated NCA material. The uniform distribution of Nb indicates that the coating process was successful. The cycling stability of NCA was first measured in Li-NCA cells with excess lithium capacity (Figure 2.16). The electrode shows an initial capacity of 170 mAh g^{-1} which gradually degrades to 120 mAh g^{-1} after 50 cycles at a current density of 0.1 mA cm^{-2} between 2.5-4.3 V. This capacity retention is comparable to previous reports and further improvement in coating quality can certainly help enhance its stability[4,9,10,13,16].

The performance of the NCA-Cu cells with different areal capacities is shown in Figure 2.5. Figure 2.5a shows the capacity retention and voltage profile evolution of a cell with a capacity of 0.25 mAh cm^{-2}. Due to the irreversible capacity of NCA during the 1st cycle, there was excess lithium stored at the anode at the end of cell discharge. Consequently, the cell operates as the one with excess active lithium when cell degradation is mainly due to gradual cathode capacity loss. After about 6 cycles, the degradation of the CE and cycling capacity accelerated, implying the excess lithium was consumed due to the instability of deposited Li metal with the electrolyte. Starting with the 7th cycle, the cell capacity retention reflects the consumption of active lithium. The cell ran out of lithium in ~40 cycles, with a calculated efficiency of 94.8% per cycle. Similar performance trends were observed for NCA cathodes with capacities of 0.5 mAh cm^{-2} and 0.75 mAh cm^{-2} as shown in Figure 2.5b and 4c. Both cells suffered more rapid capacity loss with respective efficiencies of 94.7% and 92.2%. The poor cycling performance indicate that the consumption of active lithium at the anode/electrolyte is substantial.

The 3D-NCA cells delivered much improved performance (Figure 2.6). At a graphite anode capacity/NCA cathode capacity (G/N) ratio of 4/3, the graphite-NCA full cell is a lithium-ion battery involving no lithium metal deposition. As the G/N ratio decreases below one, lithium metal starts to deposit on the surface of graphite, and it turns to a hybrid anode battery. As shown in the Figure 2.17, the cell energy density increases about two times as the G/N ratio decreases from 2 to 0.4, implying the significant

improvement in energy density by introducing lithium into the 3D host. As shown in Figure 2.6a, the cell shows a cycling stability comparable to the Li-NCA cell, indicating that the graphite/LPS interface is quite stable. The excess lithium provided by the NCA cathode during the first charging process was apparently sufficient to compensate for any parasitic loss on the anode. Such stability is likely attributed to the limited volume change of the graphite anode. We then reduced the G/N ratio to 2:3 when 0.5 mAh cm^{-2} capacity was expected to be stored in graphite and 0.25 mAh cm^{-2} was as lithium metal, which is corresponding to ~390 mAh g^{-1} effective graphite specific capacity. This capacity ratio can be confirmed by analyzing the cell discharge profile. When anode metallic lithium is exhausted and lithium is deintercalated from the graphite, the anode potential will increase which results in an inflection point on the discharge profile, as the marked region in the voltage profiles. Depending on the G/N ratio, the average discharge voltage of the NCA-3D cell will be slightly lower than NCA-Li or NCA-Cu. This 3D-NCA cell retained 38% of its capacity after more than 80 cycles with a 98.8% average CE, a vast improvement over the case of Cu-NCA shown in Figure 2.6a, which lost all its capacity within 40 cycles. Increasing the total areal capacity to 1 mAh cm^{-2}, which includes 0.5 mAh cm^{-2} of lithium metal capacity and 0.5 mAh cm^{-2} of graphite capacity, corresponds to a G/N ratio of of 2:4 and ~520 mAh/g graphite specific capacity. As shown in Figure 2.6c, the cell capacity retention is 36% after 70 cycles with a 98.5% average CE. Further increasing the areal capacity to 1.25 mAh cm^{-2} increases the G/N ratio to 2/3 and the effective graphite specific

capacity to ~650 mAh g^{-1}. This cell retained 27% of its capacity after 55 cycles with a 97.5% average CE as shown in Figure 2.6d. The employment of a 3D anode greatly improved both cell life and CE. As shown by the EIS analysis in Figure 2.18, improvements in the compatibility between Li and LPS are needed to realize longer cycle life.

2.4 Conclusion

We have shown that over-lithiated graphite can serve as a convenient 3D host for lithium metal plating in a solid-state battery, thus moving most of the deposited lithium away from the interface between anode and SSE. This design significantly improves critical current density and cycle life in half cells. Moreover, this design enables the fabrication of "lithium-free" solid state 3D-NCA cells. By simply adjusting the graphite to NCA mass ratio, lithium metal is plated in the porous framework formed by the 3D lithiated graphite and LPS electrolyte. These cells show much improved cycle life and CE as compared to the baseline cells using planar copper current collectors. This work clearly illustrates the benefits of depositing Li metal away from the interface in a 3D mixed conductive network. With further improvement in electrolyte stability and microstructure design, the 3D anode approach provides a convenient, promising pathway towards a high energy density, long-life and low-cost all solid-state batteries.

2.5 Figures

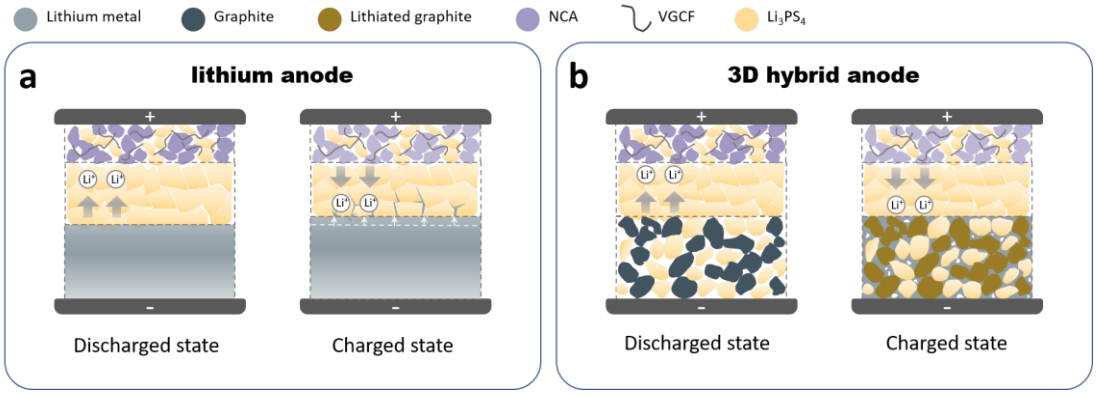

Figure 2.1 All solid-state lithium metal battery (a) schematic of an all solid-state battery with lithium metal as anode. (b) schematic of an all solid-state battery with hybrid 3D anode.

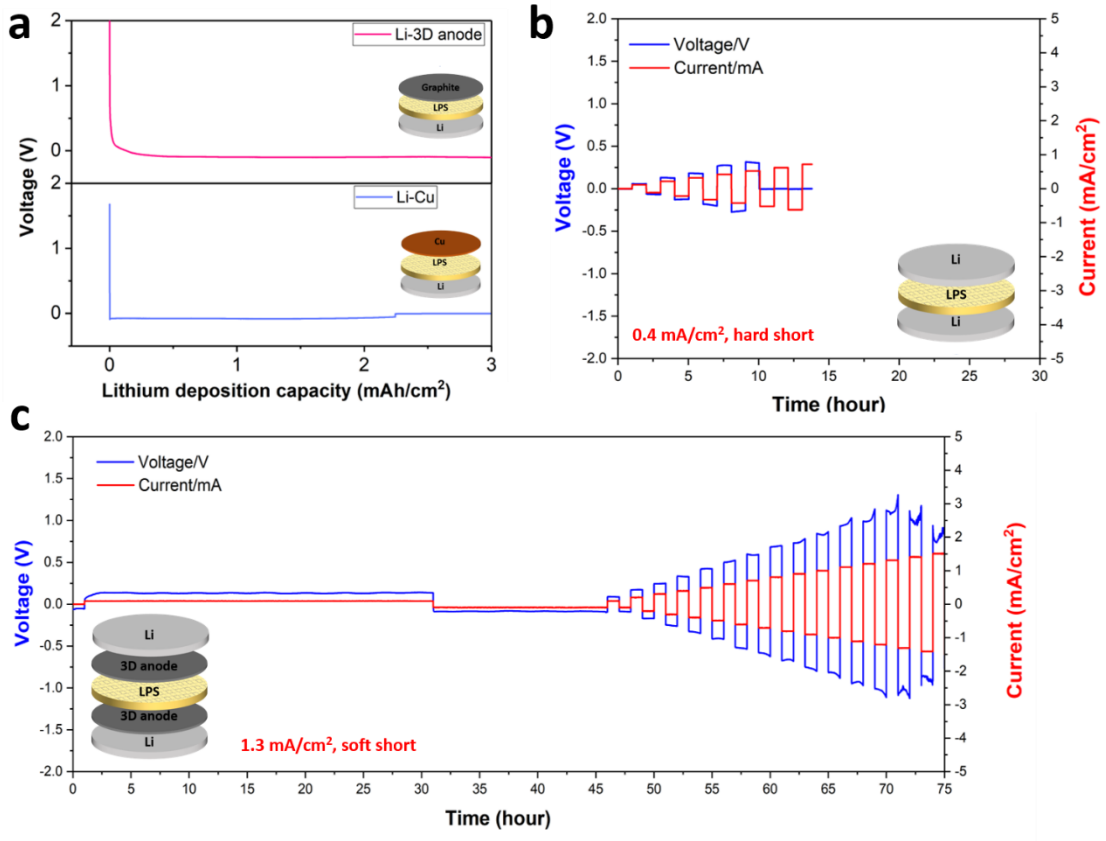

Figure 2.2 Direct Li plating on Li metal anode and 3D anode. (a) Voltage profiles of Li deposition in Li-3D anode cell and Li-Cu cell. (b) SEM image and (c) EDX mappings of cross-section of Li-3D anode cell after 1 mA cm^{-2} lithium deposition.

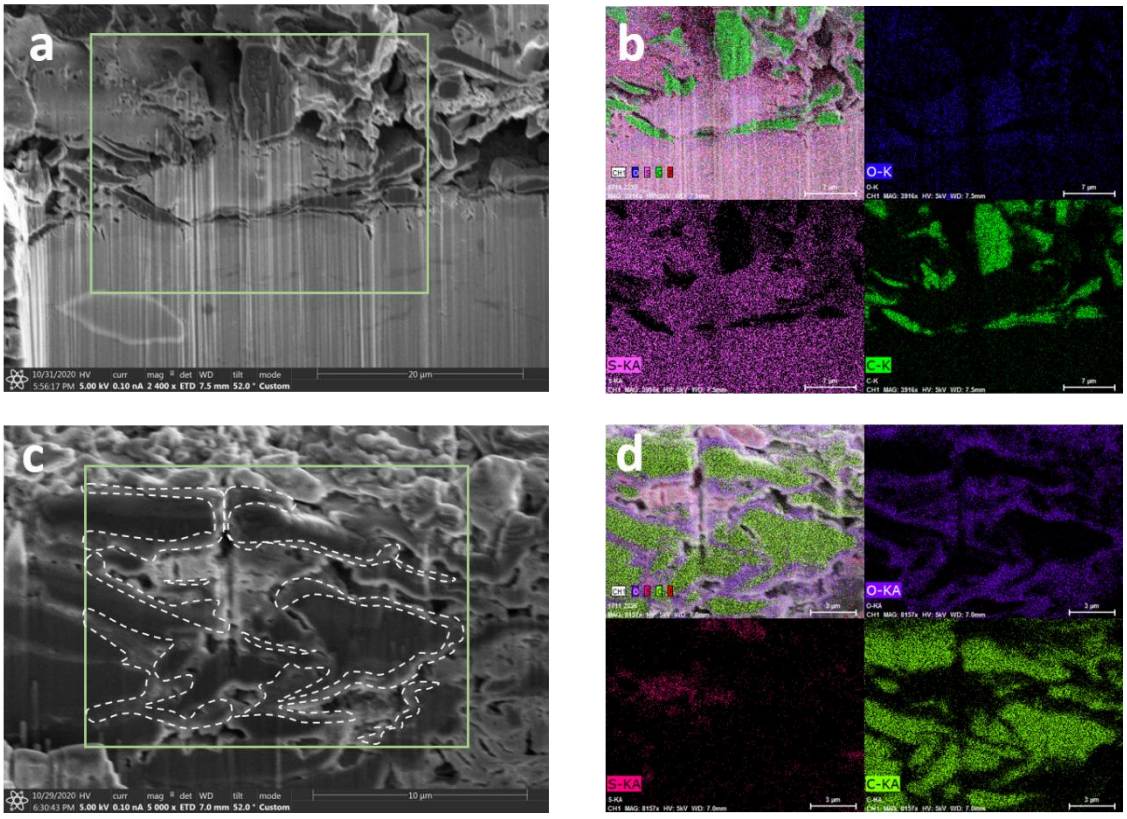

Figure 2.3 (a) SEM image and (b) EDX mappings of cross-section of Li-3D anode cell after lithiation to 0 V, (c) SEM image and (d) EDX mappings of cross-section of Li-3D anode cell after lithiation and 1 mA cm^{-2} lithium deposition.

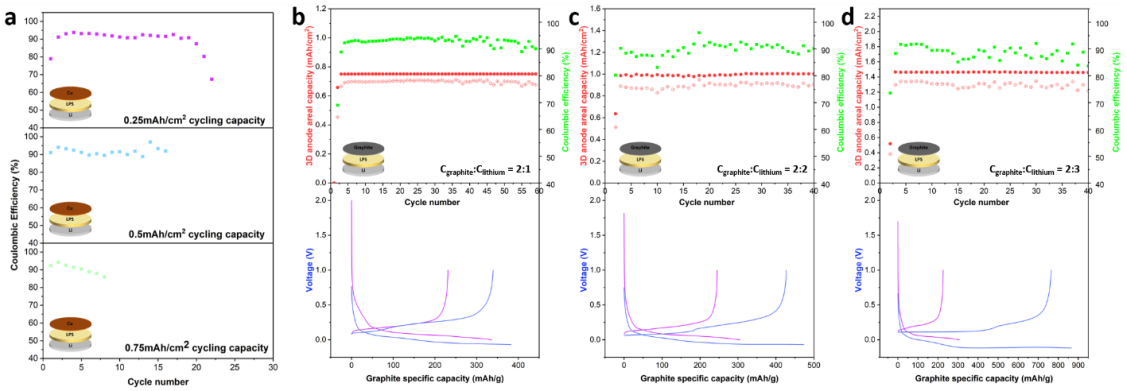

Figure 2.4 Electrochemical performance of the Li-Cu cells and Li-3D anode cells. (a) Coulombic efficiency of Li-Cu cell with 0.25 mA cm^{-2}, 0.5 mA cm^{-2}, 0.75 mA cm^{-2} lithium deposition capacity. (b) performance and voltage profiles of Li-3D anode cell with 0.75 mA cm^{-2} cycling capacity, 0.25 mA cm^{-2} capacity stored as lithium metal in anode. (c) performance and voltage profiles of Li-3D anode cell with 1 mA cm^{-2} cycling capacity, 0.5 mA cm^{-2} capacity stored as lithium metal in anode. (d) performance and voltage profiles of Li-3D anode cell with 1.25 mA cm^{-2} cycling capacity, 0.75 mA cm^{-2} capacity stored as lithium metal in anode.

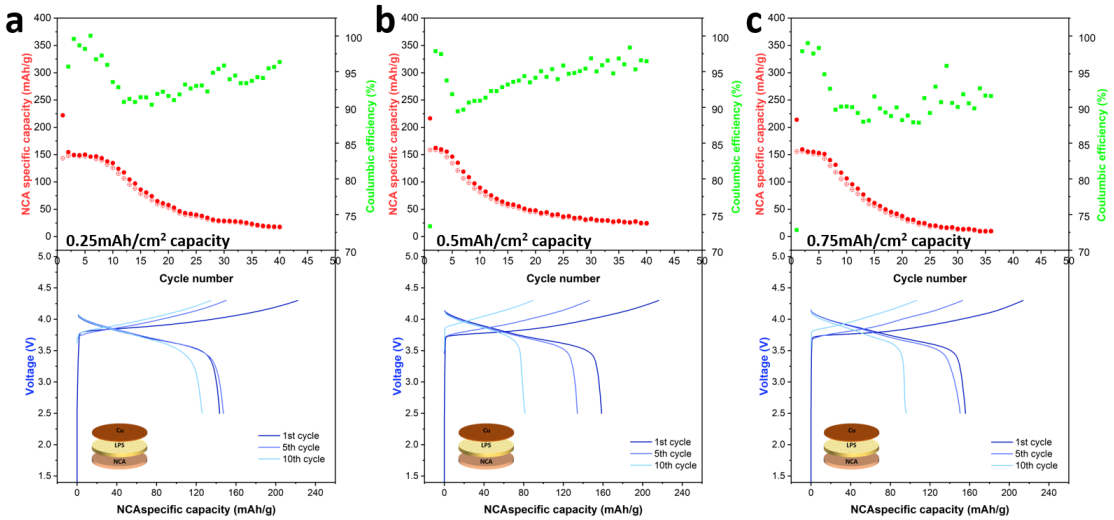

Figure 2.5 Electrochemical performance of NCA-Cu cells. (a) cycling performance and voltage profiles of the NCA-Cu cell with 0.25 mAh cm^{-2} areal deposition capacity. (b) cycling performance and voltage profiles of the NCA-Cu cell with 0.5 mAh cm^{-2} areal deposition capacity. (c) cycling performance and voltage profiles of the NCA-Cu cell with 0.75 mAh cm^{-2} areal deposition capacity.

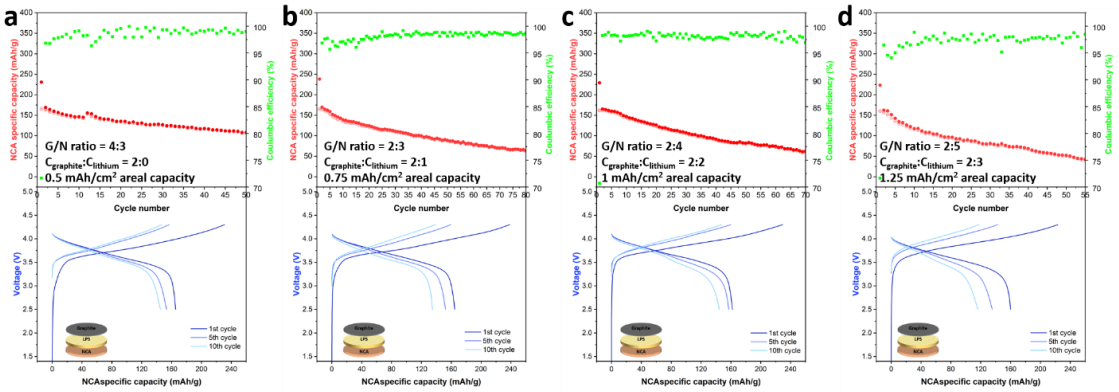

Figure 2.6 Electrochemical performance of NCA-3D anode cells. (a) cycling performance and voltage profiles of the NCA-3D anode cell with G/N ratio = 4:3, no capacity stored as lithium in anode. (b) cycling performance and voltage profiles of the NCA-3D anode cell with G/N ratio = 2:3, 0.25 mAh cm^{-2} capacity stored as lithium metal in anode. (c) cycling performance and voltage profiles of the NCA-3D anode cell with G/N ratio = 2:4, 0.5 mAh cm^{-2} capacity stored as lithium metal in anode. (d) cycling performance and voltage profiles of the NCA-3D anode cell with G/N ratio = 2:5, 0.75 mAh cm^{-2} capacity stored as lithium metal in anode.

2.6 Supporting information

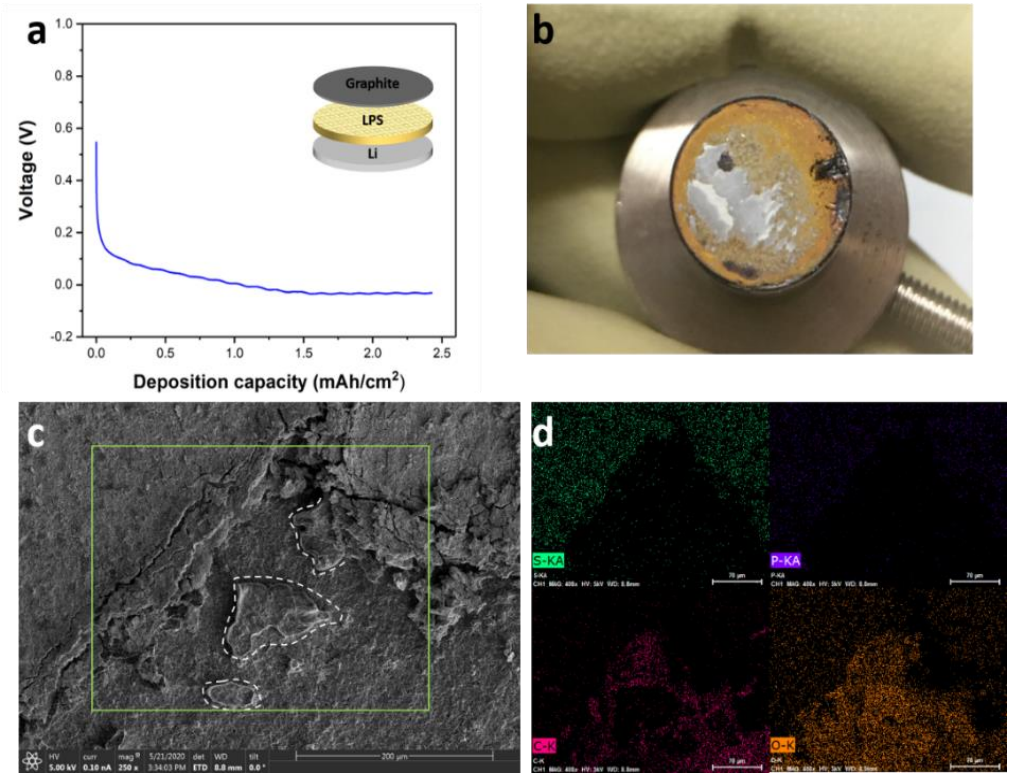

Figure 2.7 a) voltage profile of lithium plating on graphite anode in Li-graphite cell. b) image of the surface of dissembled graphite anode after lithium plating. c) SEM image and d) EDX mapping of an area from the dissembled anode.

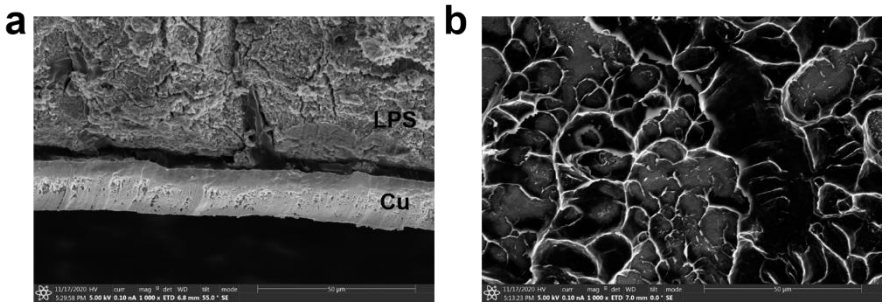

Figure 2.8 SEM images of (a) cross section and (b) top view of lithium metal deposition on the Cu current collector with LPS SE.

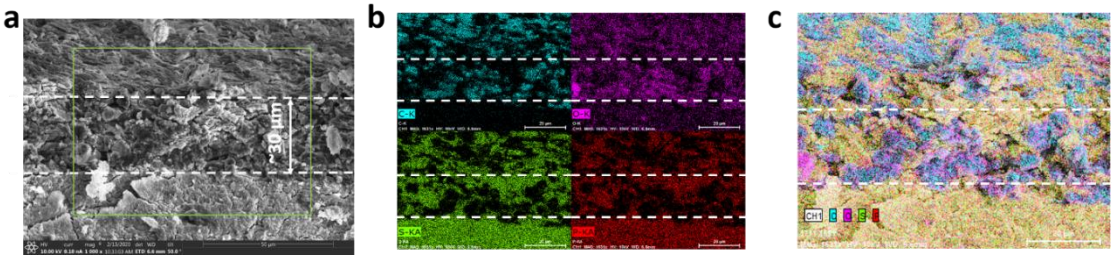

Figure 2.9 EDX mapping of the tilted cross section image of Li-3D anode cell after 1mA cm^{-2} lithium deposition.

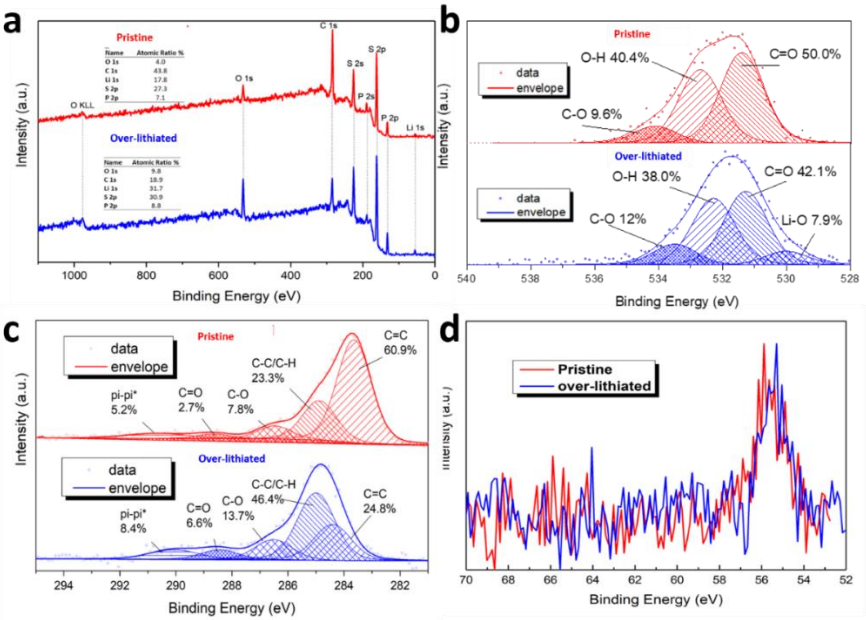

Figure 2.10 (a) XPS full scan spectra, (b) O 1s spectra, (f) C 1s spectra and (g) Li 1s spectra of pristine 3D anode and over-lithiated 3D anode.

In the O 1s XPS spectra shown in Figure S4b, only the over-lithiated sample has the Li-O component peak at 530 eV, which suggests it should be the metallic lithium being oxidized by air. Moreover, in the C 1s peak, as shown in Figure S4c, the sp2 carbon (<284.5 eV), had decreased from 60.9% (as-prepared) to 24.8% (over-lithiated) while the sp3 carbon (284.8 eV) increased from 23.3% (as-prepared) to 46.4% (over-lithiated). Similar phenomena had been reported previously[164], and attributed to lithium being oxidized by oxygen. This oxidized lithium can be partially coordinated by the pi-electron from graphites, thus shifting these sp2 carbon electrons signals to a higher binding energy in XPS. Moreover, in the Li 1s XPS in Supporting Information, Figure S4d, after lithiation, even though the peak is close to the as-prepared samples Li 1s peak, which indicated all the lithium atoms are the oxidized state at the <10nm surface. The fitting for the Li 1s peaks were not performed for its low signal to noise ratio due to its low relative sensitive factor. In the Li 1s XPS, a slight binding energy down shift had been observed in the over lithiated sample. A plausible explanation is that the oxidized lithium in the over-lithiated sample had been partially coordinated with graphite, consistent with what the C1s results suggested[164]. In the XPS of the over lithiated graphite, the enhanced O and Li signals in the survey spectrum, the appearance of the Li-O composition as shown by the O 1s peak, and decreased sp2 carbon signal in the C 1s peak, all suggest the deposited Lithium metal in graphite had been fully oxidized due to the air exposure. These results support the conclusion that the accumulated SEM-EDX O signal in Figure 2d, is from the deposited lithium metal which had been oxidized in the ambient air environment.

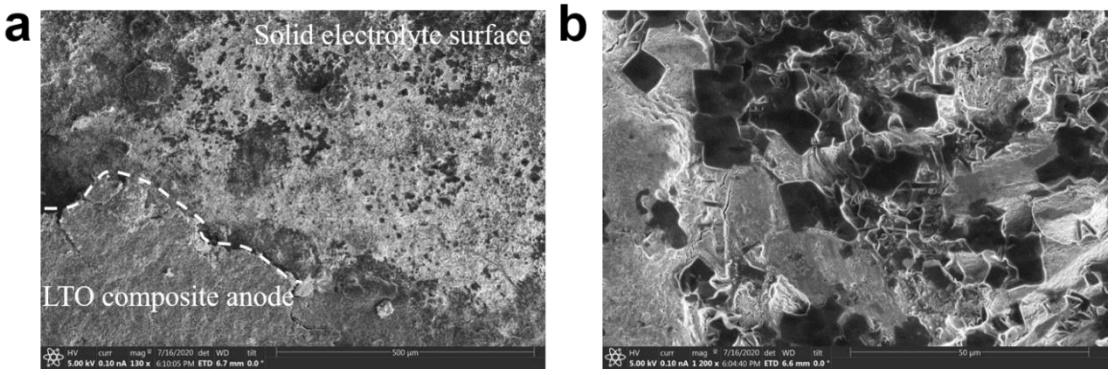

Figure 2.11 SEM images of the interface between anode and SE after over-lithiation in LTO-based anode composite cell.

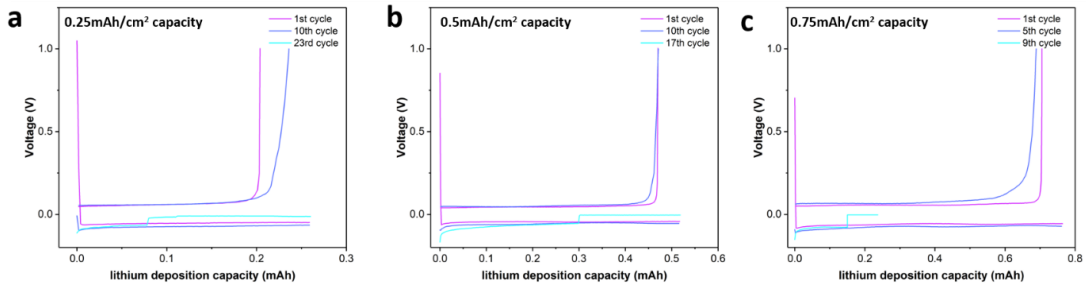

Figure 2.12 Voltage profiles of Li-Cu cells shown in Figure 2.3 with a) 0.25 mAh cm-2, b) 0.5 mAh cm-2, c) 0.75 mAh cm-2 areal Li plating capacity.

Figure 2.13 a) SEM image and b), c) EDX mapping of tilted cross section of hybrid anode after 20 cycles, which is same cell as shown in Figure 2.3b.

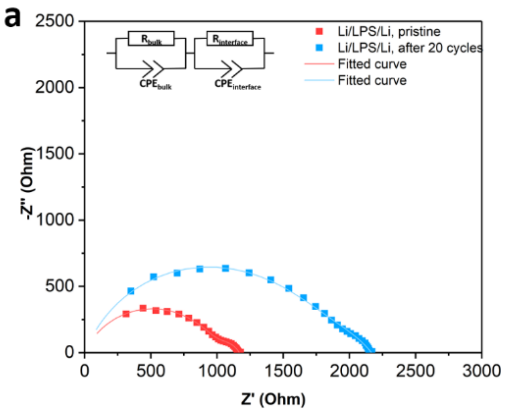

Pristine	R_{bulk}	1000 Ohm
	$R_{interface}$	166.9 Ohm
After 20 cycles	R_{bulk}	1641 Ohm
	$R_{interface}$	525.4 Ohm

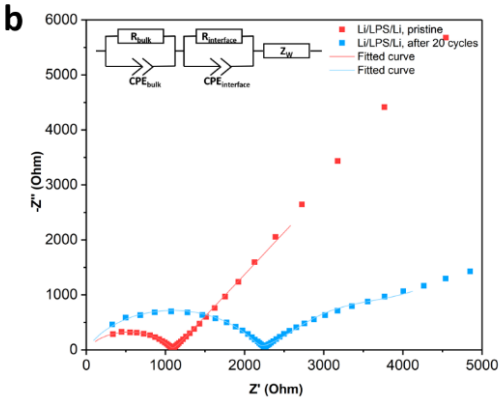

Pristine	R_{bulk}	1079 Ohm
	$R_{interface}$	29.4 Ohm
After 20 cycles	R_{bulk}	2156 Ohm
	$R_{interface}$	465.2 Ohm

Figure 2.14 Impedance plots with fitted curves of a) a Li-Li symmetric cell and b) a Li-3D anode cell before and after 20 cycles. The fitted values of Rbulk and Rinterface are listed in the table. The measurements were performed at 25 dc in a frequency range from 7 MHz to 10 mHz.

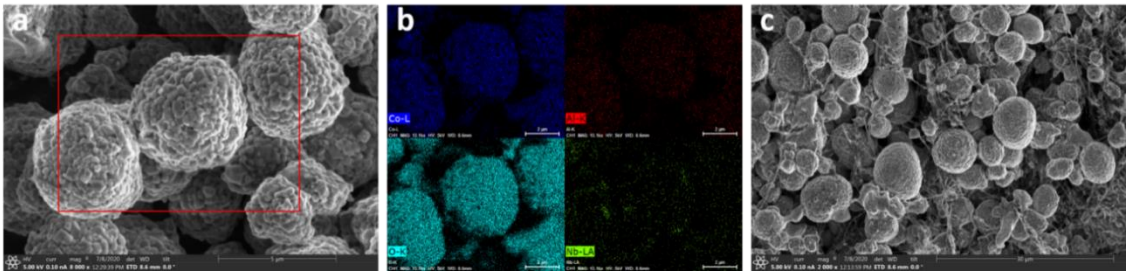

Figure 2.15 a) SEM image and b) EDX mapping of coated NCA cathode material, c) SEM image of NCA cathode composite.

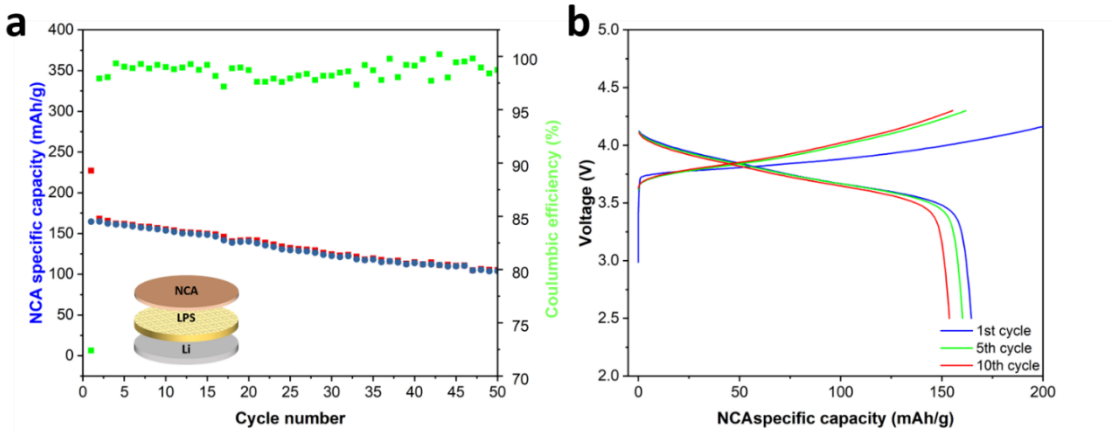

Figure 2.16 a) Cycling performance and b) voltage profiles of NCA-Li cell with LPS SSE. The cycling current density is 0.1 mAcm-2 in a range of 2.5 - 4.3 V.

G/N ratio	Weight of anode /mg	Weight of SE /mg	Weight of cathode /mg	Average voltage /V	Energy density /Wh g^{-1}
3	57.27	200	20	3.5	26.5
3	57.27	20	20	3.5	75.6
2	39.18	20	20	3.5	83.8
3/2	28.63	20	20	3.5	94.0
1	19.09	20	20	3.5	107.1
2/3	12.73	20	20	3.55	141.4
2/4	9.54	20	20	3.62	153.4
2/5	7.63	20	20	3.68	162.2
Li metal	50	20	20	3.75	87.5

Figure 2.17. Energy density projection of NCA-3D anode cells with different G/N ratios*

*NCA-3D cell information: SE: weight :20 mg, thickness: ~100 μm.
Graphite anode: specific capacity 220 mAh/g
NCA Cathode: specific capacity 150 mAh/g
Anode composition: LPS 50wt%, graphite 50wt%
Cathode composite composition: NCA 70wt%, LPS 28wt% and VGCF ((vapor growth carbon fiber).) 2wt%

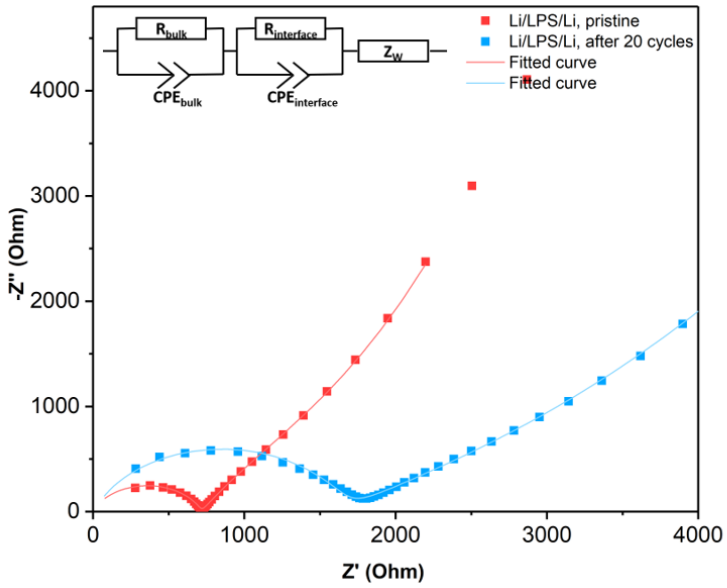

Pristine	R_{bulk}	715.6 Ohm
	$R_{interface}$	1485 Ohm
After 20 cycles	R_{bulk}	1627 Ohm
	$R_{interface}$	6055 Ohm

Figure 2.18 Photo of a flow battery hardware designed and fabricated in house.

2.7 Acknowledgments

This work has been supported by the Advanced Research Projects Agency-Energy, U.S. Department of Energy, under Contract No. DE-AR0000781.

Text, tables, and figures in this chapter, in full, are reprints of submitted publication materials: Xing Xing, Yejing Li, Haodong Liu, Zhaohui Wu, Sicen Yu, Hohn Holobek,

Hongyao Zhou and Ping Liu*, “lithium-free 3d hybrid anode for all-solid-state batteries" The dissertation author was the primary researcher for the data presented and was the primary author of this publication.

Chapter 3: Cathode electrolyte interface enabling stable Li-S batteries

3.1 Introduction

Lithium-sulfur (Li-S) batteries are being extensively studied due to their high theoretical energy density of 2600 Wh/kg and low cost of sulfur[165]. In order to make a long cycle life battery, both electrodes have to be highly reversible and free of side reactions with the electrolyte, and the electrolyte should not promote further parasitic crosstalk between the two electrode reactions[45–47]. There are two classes of Li-S batteries under development.

In the first class, elemental sulfur acts as the active material. Ether-based electrolytes such as LiTFSI-DOL/DME (Lithium bis(trifluoromethanesulfonyl) imide-dioxolane/dimethoxyethane) are preferred over carbonate-based ones because the discharge of sulfur generates polysulfide species, Li_2S_n (n=2-8) that react with carbonates but are relatively inert among ethers. The high solubility of polysulfides leads to the widely studied crossover phenomenon, resulting in sulfur (and corresponding capacity) loss at the surface of lithium metal as well as in electrolytes[165]. Addition of an additive, $LiNO_3$ in particular, has been found to be highly effective in protecting the lithium metal surface from polysulfide attacks allowing for a longer cycle life[160,166]. Indeed, previous work has shown that the polysulfide and the nitrate appear to act synergistically, resulting in a more robust solid electrolyte interface (SEI) on lithium which is rich in Li_2SO_x species[167,168].

A second class of Li-S batteries employs a sulfurized polyacrylonitrile (SPAN)[70]. This material is readily synthesized by reacting elemental sulfur and polyacrylonitrile (PAN), and is electrically conducting, alleviating the need for large amounts of carbon in the electrode as in the case of elemental sulfur. Specific capacities of 400-700 mAh/g are often achieved with a sulfur content of 30-45 wt%[68,74,81,169]. Unlike elemental sulfur, SPAN is a highly stable material in carbonate-based electrolyte only, demonstrating a cycle life of up to 1000 cycles[170–172]. SPAN is one of the most stable cathode materials ever identified; the material does not appear to trigger any sulfur dissolution mechanism into the carbonate electrolyte. When used in common ether-based electrolytes, however, the material appears to revert to the solution chemistry of elemental sulfur and polysulfides[86]. The mechanism of SPAN as a cathode material is still a subject of study[84].

While it is highly desirable to employ SPAN due to its cycling stability and potential low cost, the use of carbonate electrolytes creates significant stability issues at the lithium anode. Intensive research using carbonate electrolytes has shown that lithium metal suffers from dendrite growth, low columbic efficiency (CE) of a maximum of ~92%, and a rapid loss of active lithium. In contrast, ether-based electrolytes, such as LiTFSI-DOL/DME, have consistently shown much higher CE (~98%) and generally dendrite-free morphology for lithium metal deposits. Highly concentrated ether-based electrolytes have achieved efficiencies of > 99%[173–175]. This has resulted in recent efforts to identify ether-based electrolytes suitable for the reversible cycling of SPAN[86,176,177].

This work investigates ether-based electrolytes that enable robust cathode electrolyte interface (CEI) and solid electrolyte interface (SEI) layer formations, leading to highly reversible cycling. A promising concentrated ether electrolyte with LiTFSI and $LiNO_3$ as co-salts is identified for a highly stable Li-SPAN battery $LiNO_3$ is hypothesized to encourage the formation of a robust SEI for lithium metal anodes and CEI for SPAN cathodes, while the high salt concentration discourages the dissolution of polysulfide to reduce the consumption of $LiNO_3$. Indeed, a CEI that contains crystalline LiF and $LiNO_2$ is observed for the first time. Finally, a successful Li-SPAN battery with limited lithium supply is demonstrated, which not only confirms the high efficiency cycling of the lithium electrode, but also points to the possibility of high energy density rechargeable batteries.

3.2 Experiment section

SPAN material synthesis

All chemicals were purchased from Sigma-Aldrich unless specified otherwise and used without purification. To synthesize SPAN material, elemental sulfur and polyacrylonitrile (Mw = 150,000) were hand milled in a ratio of 4:1 to ensure homogeneous mixing. The mixed samples were heated in an argon-filled furnace at 450°C for 6 hours with a ramp rate of 2 °C/min, then allowed to cool to room temperature[169].

Electrolyte preparation and solubility tests

Ethylene carbonate (EC), dimethyl carbonate (DMC), 1,3-dioxolane (DOL), 1,2-dimethoxyethane (DME) were purchased from BASF and used as received. The five electrolytes of 1 M LiTFSI/EC-DMC(1:1, v/v), 1 M LiTFSI/DOL-DME(1:1, v/v), 4 M LiTFSI/DOL-DME(1:1, v/v), 1 M LiTFSI/DOL-DME(1:1, v/v) with 0.5 M $LiNO_3$, and 4 M LiTFSI/DOL-DME(1:1, v/v) with 0.5 M $LiNO_3$ were prepared by dissolving predetermined amounts of LiTFSI and $LiNO_3$ salts into mixed solvents and stirred to achieve stable and clear solutions. Solubility tests were performed by adding 0.25 M Li_2S_6 (which corresponds to 0.25 M Li_2S and 1.25 M sulfur) into the respective prepared electrolyte. Photographs of the solutions were taken after 24 hours. The solubility was measured by ultraviolet-visible spectrometry (UV-vis) after 200x dilution with a 1:1 DOL/DME mixture solvent. All the processes were performed in an argon-filled glove box with a water concentration < 1 ppm.

Electrochemical characterizations

Coulombic efficiency of lithium deposition/stripping tests were determined by Li-Cu cells in chosen electrolyte, using LAND battery testers (Wuhan, China). Typically, a constant capacity of lithium (1 mAh/cm^2) was deposited on Cu foil at a constant current density 0.5 mA/cm^2, and then stripped at the same current density to a cut-off voltage of 1.0 V vs Li/Li^+[118].

SPAN cathode was prepared with SPAN powder, Super-P and PVDF in a ratio of 70:15:15 mixed in N-methyl pyrrolidinone (NMP) solvent and cast on carbon coated Al foil. After drying in a vacuum oven at 80 °C overnight, the SPAN cathode loading was around 1.5 mg/cm^2. Fixed amount of electrolyte (~34 μL/cm^2) is added into each coin cell to guarantee the completely wetting of the separator and electrodes. The electrolyte/SPAN ratio is 22 μL/mg. The cycling performance tests of using excess lithium source were carried out in different electrolytes assembled with lithium discs (MTI, 250 μm thickness) and Celgard separators (Celgard, USA). Galvanostatic charge/discharge was conducted in a fixed voltage range of 1 – 3 V vs. Li/Li$^+$ at room temperature with 100 mA/g current density based on SPAN weight.

Limited capacity anodes were prepared electrochemically by using Li-Cu cells. 2 mAh/cm^2 lithium was deposited onto Cu foil in selected electrolyte at a current density of 0.1 mA/cm^2[178]. After deposition, the cells were disassembled to separate the anode. The anodes were rinsed with ~10 ml of solvent; the cell deposited with 1 M LiTFSI/EC-DMC (1:1, v/v) electrolyte was rinsed with DMC and the cell deposited with 4 M LiTFSI/DOL-DME (1:1, v/v) + 0.5 M $LiNO_3$ electrolyte was rinsed with DME. Rinsed anodes were dried in vacuum and then coupled with SPAN cathode in the same electrolyte as that used for the lithium depositing cell. The following galvanostatic charge/discharge was conducted in a fixed voltage range of 1 – 3 V vs. Li/Li$^+$ at room temperature with 100 mA/g current density based on SPAN weight.

Structure characterizations

The morphologies of the cycled lithium anode surface were characterized using scanning electron microscopy (FEI Quanta 250 SEM) coupled with an energy dispersive X-ray spectrometer (EDS) to determine the chemical composition of the samples. The crystal structures of the cycled cathode surface were examined by X-ray diffraction (XRD) and acquired using a Bruker D2 phaser diffractometer with a Bragg-Brentano θ-2θ geometry and a Cu Kα source (λ = 1.54 Å). Samples were sealed inside the glovebox with Kapton tape and scanned at a rate of 0.02° s^{-1}. Micrographs were recorded on a field emission gun (FEG) JEM-2100F cryo-transmission electron microscopy (TEM), equipped with a OneView camera and operated at 200 keV. The TEM samples were loaded onto the cooling holder inside glovebox and transferred to the TEM system with continuously flowing argon gas. The images were taken when the temperature of samples reached about 100 K.

3.3 Results and discussion

Four electrolyte compositions are chosen to facilitate the examination of the effect of $LiNO_3$ addition and salt concentration in Li-SPAN cell; their electrochemical performance is shown in Figure 3.1a. The cell with the 1 M LiTFSI electrolyte shows rapid capacity degradation, where only 66.5% capacity remains after 20 cycles. The coulombic

efficiency (CE), defined as the ratio of discharge capacity to charge capacity immediately before the step, is less than 50%. This instability is in sharp contrast to the materials outstanding cycling stability in 1 M LiTFSI in EC/DMC with negligible capacity decay over 100 cycles along with close to 100% CE (Figure 3.6). In the dilute ether electrolyte, the voltage profiles are also different. The Li-SPAN cell only shows a sloped voltage plateau in the discharging and charging voltage profile as shown in Figure 3.6. However, in the voltage profile of 1 M LiTFSI ether-based electrolyte cell (Figure 3.1b), there is a voltage plateau at ~2.1V during discharge indicating that the active material displays a behavior similar to that of elemental sulfur[165]. This leads to the well-known shuttle effect which manifests as both irreversible sulfur loss from SPAN cathode due to polysulfide dissolution and as low coulombic efficiency due to reactions between lithium and polysulfides on the anode surface[166]. SPAN exhibits an ultrahigh charge capacity of ~2300 mAh/g in the 1 M LiTFSI electrolyte as a consequence of the shuttle effect[46,47,165,168]. The dissolved low order polysulfides was oxidized to high order polysulfides, which diffuse to anode surface and get reduced back to low order polysulfides by lithium metal, causing this apparent high capacity during charge.

Increasing electrolyte concentration to 4 M leads to a reduced rate in capacity decay (81.2% after 20 cycles), although the capacity retention is still far inferior to that observed in carbonate electrolytes. The voltage profile in Figure 3.2.1b no longer shows the distinctive plateau corresponding to the elemental surface redox chemistry. However, CE

values are below 99% for the first 20 cycles, indicating the presence of irreversible reactions. The CE reaches over 99.4% after 20 cycles, indicating that the polysulfide shuttle effect is significantly suppressed.

The addition of $LiNO_3$ is found to have a more significant impact on capacity retention and CE. In the 1 M LiTFSI + 0.5 M $LiNO_3$ cell, CE increases to close to 100% after 23 cycles and capacity retention is 84.2% after 100 cycles. When 4 M LiTFSI is used in combination with 0.5 M $LiNO_3$, cell performance is further improved, achieving 89.4% capacity retention after 100 cycles and a stable CE of 100% after only 6 cycles. As has been previously reported[168], the presence of $LiNO_3$ can effectively stabilize the lithium anode surface, via the in-situ formation of a SEI layer, which inhibits the shuttle effect and improves CE. The presence of polysulfide in the solution might actually act synergistically to improve the efficacy of the layer[179]. Noticeably, the ~2.1 V plateau during discharge is also eliminated even in a 1 M LiTFSI electrolyte solution in the presence of $LiNO_3$ as shown in Figure 3.1b. A possible explanation is that $LiNO_3$ suppresses the formation of polysulfides from the SPAN cathode during cycling, which is carefully examined later.

In order to understand the respective roles of $LiNO_3$ and high salt concentration in determining cell performance, we first analyzed their impact on the lithium metal electrode cycling performance and established that a combination of high salt concentration and $LiNO_3$ additive enables highly stable lithium metal cycling with good Coulombic efficiency.

The CE tests for lithium metal plating/stripping in different concentrations of electrolytes are performed at a current density of 0.5 mA/cm^2 and a capacity of 1 mAh/cm^2 in Li-Cu cells and the results are shown in Figure 3.7. Also included for comparison are the CE results of the carbonate-based electrolyte (1 M LiTFSI - EC/DMC). The carbonate-based electrolyte has an average CE of 91.6% over 40 cycles, similar to previous reports[175]. The low CE reflects the high reactivity between lithium and the organic carbonates[45,180]. The 1 M LiTFSI ether electrolyte has a CE value averaging around only 80%, even worse than the carbonate. However, raising the salt concentration to 4 M leads to an average CE of 95.3%. With the $LiNO_3$ additive, high average CEs are achieved in both 1 M (98.1%) and 4 M (98.0%) ether-based electrolytes, suggesting that the $LiNO_3$ plays a critical role in enabling high efficiency lithium metal cycling[117,181].

We next examine how the electrolyte composition affects polysulfide dissolution. 0.25 M Li_2S_6 is dissolved in the four electrolytes described in Figure 3.1. Figure3.8a shows a high solubility of polysulfide in dilute DOL/DME electrolyte as indicated by the dark-brown color. In contrast, the light-yellow color in concentrated DOL/DME indicates a much lower solubility. To further quantify the solubility, UV-Vis spectra of the solutions are obtained as shown in Figure 3.8b. The signals were taken after the solutions were diluted by 200x. The absorption peaks at 475, 420, and 617 nm correspond to S_6^{2-}, S_4^{2-}, and $S_3^{\cdot-}$, respectively[66]. Based on the calibration curves shown in Figure 3.8c and d, the calculated concentration of polysulfide in 1 M LiTFSI - DOL/ DME is 0.2312 M, which is

consistent with the starting solution of 0.25 M. However, after raising the LiTFSI concentration to 4 M, the solubility drops to only 0.0041 M, clearly demonstrating the effective suppression of polysulfides dissolution. By adding 0.5 M $LiNO_3$ into the concentrated electrolyte, polysulfide solubility is further reduced to 0.0017M. We hypothesize that the reduced solubility is due to Le Châtelier's principle of solubility, although a systematic study using molecular dynamics calculation would help to reveal the actual solution structure, a subject of future study. Therefore, it is concluded that both LiTFSI and $LiNO_3$ help suppress dissolution of polysulfides effectively.

Post-mortem analysis of the cells after cycling is then performed in order to better understand the underlying mechanism. The morphologies of cycled lithium metal anode surface in Li-SPAN cells are evaluated with SEM. As shown in Figure 3.9, in 1 M LiTFSI electrolyte, non-dendritic lithium metal is observed but the uniformity is poor and voids are clearly present. However, in the concentrated electrolyte with $LiNO_3$ addition, lithium metal particles are big, uniform and highly compact. EDS in Figure 3.10 confirms that a combination of high salt concentration and $LiNO_3$ leads to the lowest sulfur accumulation on the anode surface, which is consistent with effective polysulfide dissolution suppression and the protective function of $LiNO_3$.

XPS measurements are carried out to further characterize the chemical composition of the respective cycled lithium anode surface. In S_{2p} spectra Figure 3.11, the double peaks at 167.9 eV and 161.3 eV are assigned to Li_2SO_x and Li_2S/Li_2S_2 based on

previous reports[160,166]. The major difference in the spectra in Figure 3.11a and S6b is the intensity of Li_2S/Li_2S_2 peaks. The addition of $LiNO_3$ greatly reduces the amount of sulfides on the anode surfaces. Previous work has established that Li_2S/Li_2S_2 can be oxidized by NO_3^- into Li_2SO_x on the lithium surface, which is a more effective conducting SEI component in Li-S batteries[182]. This observation is consistent with the results of N1s spectra (Figure 3.12b). The $Li_2N_xO_y$ and $Li_2N_2O_2$ peaks confirm the reduction products from $LiNO_3$. In the 4M LiTFSI electrolyte, both Li_2S_2/Li_2S and Li_2SO_x peaks decrease, indicating fewer polysulfides migrate from cathode to anode. The addition of $LiNO_3$ produces the least amount of sulfides on the anode surface. Therefore, the concentrated electrolyte with $LiNO_3$ produces less sulfur-containing and more conductive components on the lithium anode surface, which is consistent with SEM-EDS results.

The surface structure of the cathode is then examined after cycling. Figure 3.2 shows the S2p XPS results obtained on as-harvested electrodes. The double peaks at around 164.8eV are assigned to the C-S and S-S bonds in the SPAN material based on previous reports[172]. The addition of $LiNO_3$, however, appears to reduce the signal, indicating that the SPAN is likely covered with a protection layer. This is most evident for the electrode tested in 1 M LiTFSI with $LiNO_3$ (Figure 3.2b) where the signals from the SPAN material are completely absent. To confirm this hypothesis, the samples were ion etched and examined again. The results (Figure 3.3) show an increase of the peak intensities for every electrode, with the electrode cycled in $LiNO_3$-based electrolyte experiencing the most

significant increase. The S2p spectra also reveals that the surface of the cathode is populated with Li_2SO_x and Li_2S/Li_2S_2 species as well. Comparing Figure 3.2a and b, the addition of $LiNO_3$ in 1 M ether electrolyte leads to greatly reduced sulfide (Li_2S/Li_2S_2) to sulfate (Li_2SO_x) ratios. A similar conclusion can be reached when comparing Figure 3.2c and d for concentrated salt solutions. Thus, the Li_2S/Li_2S_2 components are oxidized by $LiNO_3$ into Li_2SO_x components on the surface of the cathode, leading to the formation of a CEI layer. Furthermore, this CEI layer has N containing species as well, as shown by the N1s spectra in Figure 3.13.

We then use TEM to further examine the surface structure of the cathode cycled in 4M LiTFSI with $LiNO_3$ addition. SPAN itself is an amorphous material as shown in Figure 3.14. After cycling, a surface layer is observed with a thickness of ~27 nm (Figure 3.3a). The presence of lattice fringes indicate that the surface layer is crystalline. Selected area electron diffraction (SAED) identifies the phases to be LiF and $LiNO_2$. To further confirm this finding, XRD measurements are taken of the electrode. Surprisingly, weak but clearly visible peaks are obtained (Figure 3.3d) which index to LiF and $LiNO_2$. Our XPS, TEM, and XRD results confirmed the presence of $LiNO_2$ in the CEI layer, which is a reduction product of $LiNO_3$. Previous work has shown $LiNO_3$ is reduced at below 1.6 V. Although $LiNO_2$ has solubility in ether, the high salt concentration employed in the current study has promoted its precipitation on the SPAN cathode surface. This is the first time a CEI layer has been directly observed and identified on a SPAN cathode. The presences of the CEI

layer is essential to enabling stable cycling of SPAN in ether-based electrolytes, including in dilute solutions where polysulfide solubility is high. This protection mechanism explains our observation in Figure 3.1b that the polysulfide discharge plateau at ~ 2.1 V and the shuttle effect are absent when the electrolyte contains 0.5 M $LiNO_3$. The CEI prevents the discharge products of SPAN from being exposed to large amounts of the electrolyte and effectively suppress the formation of soluble polysulfides.

It is thus shown that the 4 M LiTFSI with 0.5 M $LiNO_3$ in DOL/DME electrolyte enables stable Li-SPAN cells by suppressing polysulfide dissolution and forms protective layers on both the cathode and the anode. Its effect on high efficiency Li metal cycling, however, is not examined by the test results shown in Figure 3.1, where a 250 μm thick lithium metal anode is used. Within the 100 cycles, the supply of active lithium does not determine capacity retention. Rather, the data confirms that SPAN can cycle reversibly in this ether-based electrolyte with good coulombic efficiency. The performance of a cell is then evaluated where the lithium anode has a limited capacity so that consumption of lithium will eventually lead to capacity fade. This testing methodology is also mandated by the desire to design high energy density cells in which a large amount of excess lithium is both costly and detrimental to cell energy density. A capacity of 2 mAh/cm^2 of lithium was electrochemically deposited on Cu current collectors in both carbonate-based (1 M LiTFSI - EC/DMC) and ether-based (4 M LiTFSI - DOL/DME with $LiNO_3$) electrolytes to serve as limited-capacity lithium anodes. Based on the first cycle efficiency of Li-Cu

cells shown in Figure 3.7, the expected active lithium capacity deposited (C_d) on Cu foil was 1.85 mAh/cm^2 in carbonate electrolyte and 1.89 mAh/cm^2 in ether electrolyte. These lithium anodes were then reassembled in coin cells with the same respective electrolytes as the ones used for lithium deposition but now with SPAN as the cathodes. For both electrolytes, the limited lithium full cell had an initial discharge capacity of 745-755 mAh/g based on SPAN weight (Figure 3.4b). This indicates that the amount of Li^+ stripping from the anode during the initial discharge process is the same for both cells. The irreversible transformation during the first lithiation cycle is a well-known phenomenon although unexplained as shown by 1st discharge curves in Figure 3.4b[70,81], which caused another 0.2-0.3 mAh/cm^2 capacity (C_1) loss based on the mass loading (m) of 1.5 mg/cm^2. After the irreversible formation cycle, the estimated capacity ratio between the negative lithium and the positive SPAN electrodes are 2.01 and 1.85 for the two cells, respectively.

As shown in Figure 3.5a, the ether-based electrolyte enables far more stable cycling than the carbonate, maintaining 427.4 mAh/g after 100 cycles while the capacity of the cell with carbonate electrolyte degraded to zero in 60 cycles. However, both capacity loss profiles show a change in slope as a function of cycle number. The initial slow decay primarily reflects the loss of capacity of the cathode since excess lithium is available. In other words, the cells are cathode limited. After a certain number of cycles when the excess lithium was consumed, the cells become anode limited. The slope of the decay curve reflects the active lithium loss rate.

In the carbonate-based electrolyte, the excess lithium appears to have been consumed after 20 cycles when acceleration of capacity loss is accompanied by a deteriorating efficiency. At this point, the measured cathode capacity is 460 mAh/g (C_r), when the total capacity for the anode and the cathode are balanced. The lithium cycling efficiency can be calculated using the following equation:

$$CE_{Li} = 1 - \frac{C_c/(n-1)}{\overline{S_c} * m} \qquad \text{Eq. 1}$$

Where n is cycle number, $\overline{S_c}$ is the average specific capacity of the cathode, m is the areal mass loading of the cathode, and C_c is the consumed lithium capacity. C_c can in turn be calculated by

$$C_c = C_d - C_1 - C_r \qquad \text{Eq. 2}$$

where C_d is deposited lithium capacity, C_1 is first cycle irreversible capacity and C_r is the remaining capacity. For the carbonate-based electrolyte cell, C_c is calculated to be 0.89 mAh/cm^2 based on Eq.2 for the first 20 cycles, and CE_{Li} is determined to be 93.9% based on Eq.1, given $\overline{S_c}$ is 495 mAh/cm^2. A similar calculation is performed a for the ether-based electrolyte. C_c for 60 cycles is 0.85 mAh/cm^2 and CE_{Li} is 98.2%, given $\overline{S_c}$ is 525 mAh/cm^2. Both calculated CE values based on data from the cathode limited region are consistent with measured values in Li-Cu cell. In the anode limited region, the cycle number and capacity deterioration have a power law relationship. In this case, CE_{Li} can be estimated using the equation below:

$$CE_{Li} = \sqrt[n2-n1]{S_{c,n2}/S_{c,n1}} \qquad \text{Eq. 3}$$

where $S_{c,n}$ is the specific capacity of the n^{th} cycle. Based on Eq.3, the CE_{Li} is calculated to be 91.2% between 30th and 50th cycle when the cell is operated in the lithium-limited region in carbonate-based electrolyte. In contrast, the corresponding CE_{Li} for the concentrated ether electrolyte is 99.5 % between the 70th and 90th cycle. The high lithium cycling efficiency during the full cell tests indicate the formation of a stable SEI layer on the anode surface. Moreover, it also demonstrates that a robust CEI layer forms on the cathode surface, inhibiting the side reactions of lithium metal with polysulfides which might have migrated from cathode.

3.4 Conclusion

In summary, we report a concentrated ether-based electrolyte with $LiNO_3$ as a co-salt for stable-cycling Li-SPAN batteries. While the high concentration helps to reduce polysulfide solubility, the role of $LiNO_3$ is more critical. It participates in the formation of protective layers on both the anode (SEI) and the cathode (CEI). Most remarkably, a crystalline CEI layer is directly observed by TEM and identified by SAED and XRD. This observation helps explain the finding that addition of $LiNO_3$ even aids in suppressing polysulfide dissolution in a dilute ether-based electrolyte (1M LiTFSI). We note that such a protection mechanism is likely more effective on SPAN rather than on common S/C composite cathodes due to the much smaller volume change. Finally, we conclusively

demonstrate the impact of high efficiency lithium cycling in a Li/SPAN cell with limited lithium supply. Our work shows the benefits of developing electrolyte compositions for the formation of both SEI and CEI coatings for rechargeable lithium metal batteries. For the Li/SPAN cell, ether-based electrolytes provide a promising pathway towards a long-life, low cost technology.

3.5 Figures

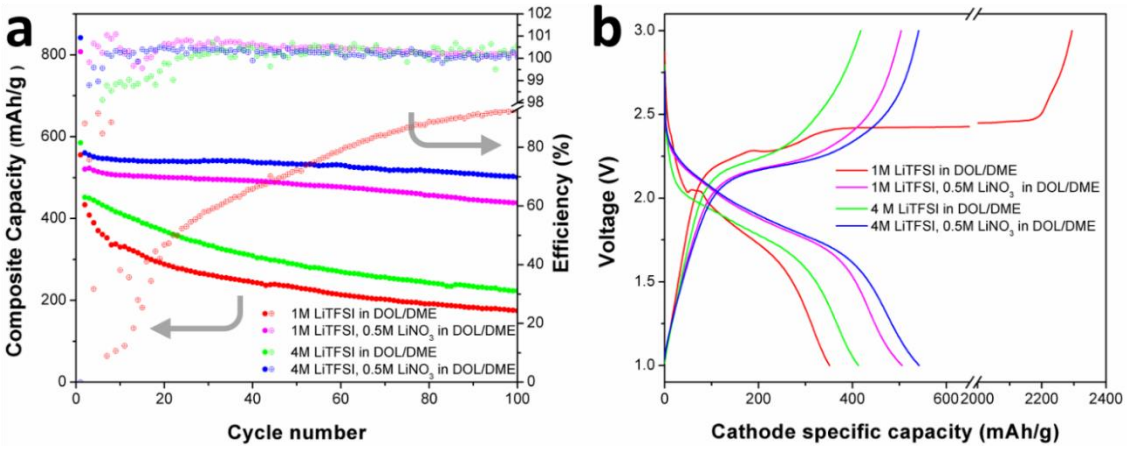

Figure 3.1 Evaluation of Li-SPAN cell performance with great excess capacity lithium anode. (a) Cycling performance at a current density of 100 mA/g, and (b) 10th discharge and charge voltage profiles of SPAN cathode with lithium anode in different electrolyte.

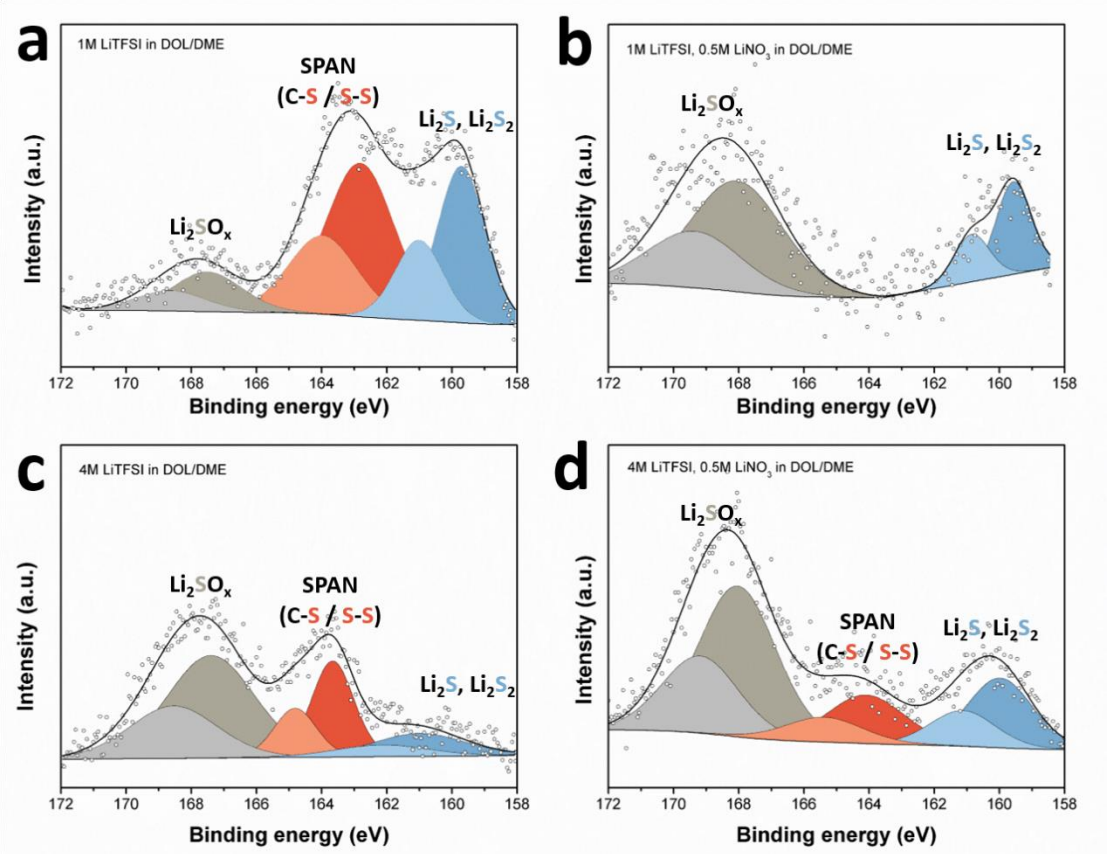

Figure 3.2 CEI composition identification of the SPAN cathode. XPS S2p spectra of SPAN cathode surface cycled in (a) 1 M LiTFSI in DOL/DME, (b) 1 M LiTFSI and 0.5 M $LiNO_3$ in DOL/DME, (c) 4 M LiTFSI in DOL/DME, (d) 4 M LiTFSI and 0.5 M $LiNO_3$ in DOL/DME.

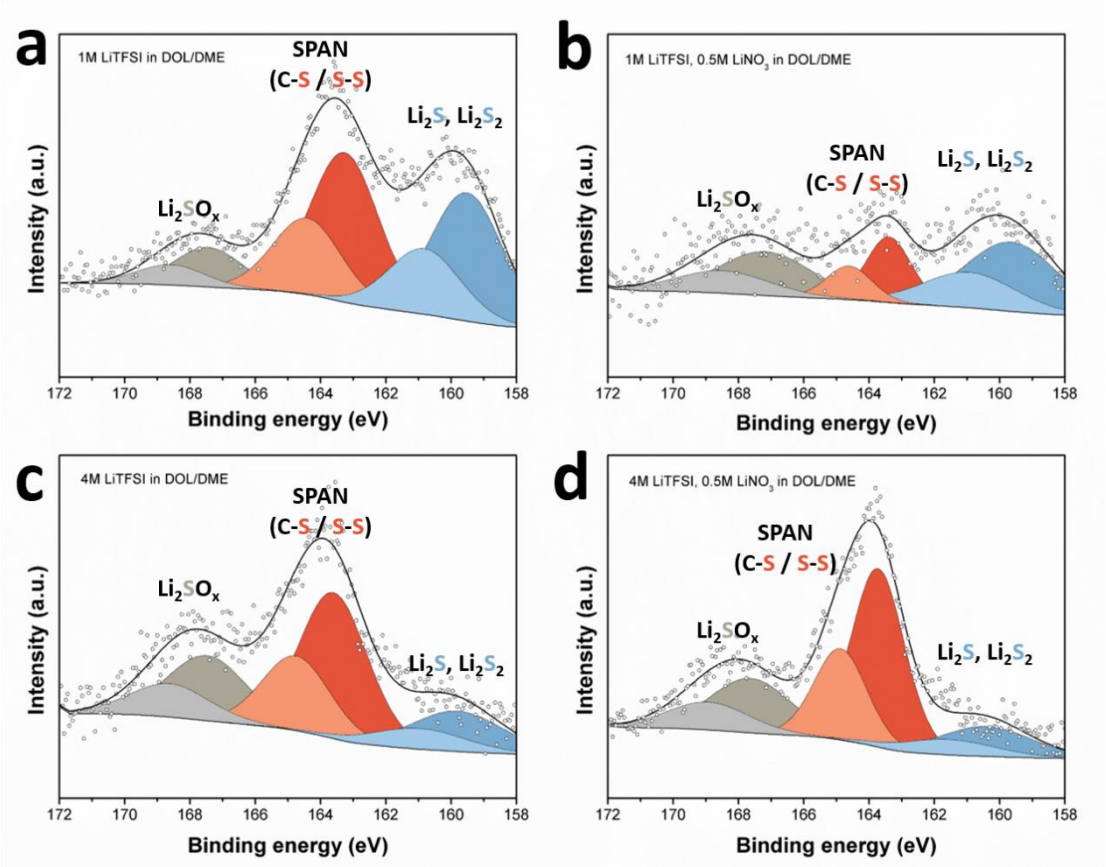

Figure 3.3 CEI composition identification of SPAN cathode surface after etching. XPS S2p spectra of ion etched cycled SPAN cathode surface in (a) 1 M LiTFSI in DOL/DME, (b) 1 M LiTFSI and 0.5 M $LiNO_3$ in DOL/DME, (c) 4 M LiTFSI in DOL/DME, (d) 4 M LiTFSI and 0.5 M $LiNO_3$ in DOL/DME. The etching condition was 10 keV for 300s.

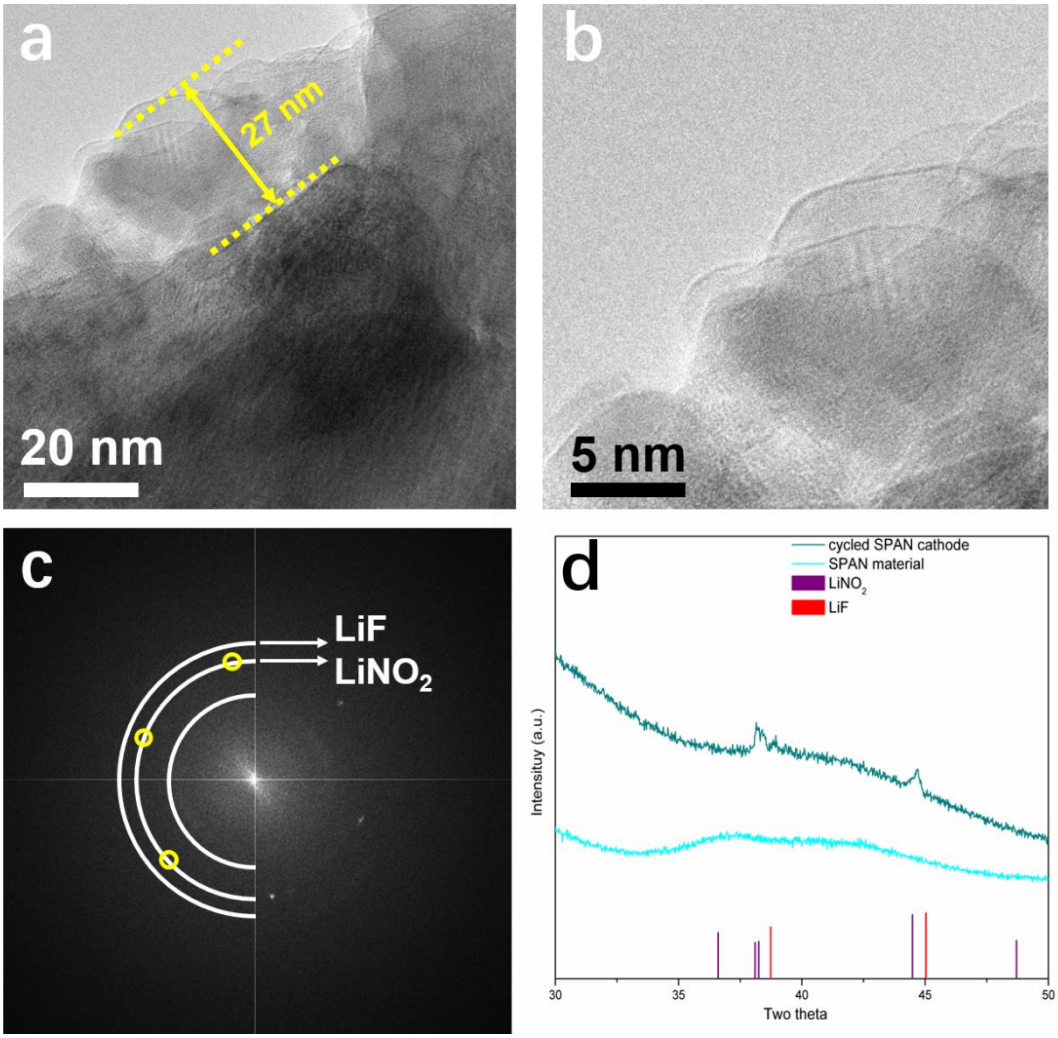

Figure 3.4 CEI layer structure observation and identification. (a) Cyro-TEM images of SPAN covered with a CEI layer; (b) expanded view of image in (a) near the surface region; (c) selected area electron diffraction (SAED) image and (d) XRD spectra of SPAN cathode after 10 cycles with 4M LiTFSI and 0.5M $LiNO_3$ in DOL/DME electrolyte.

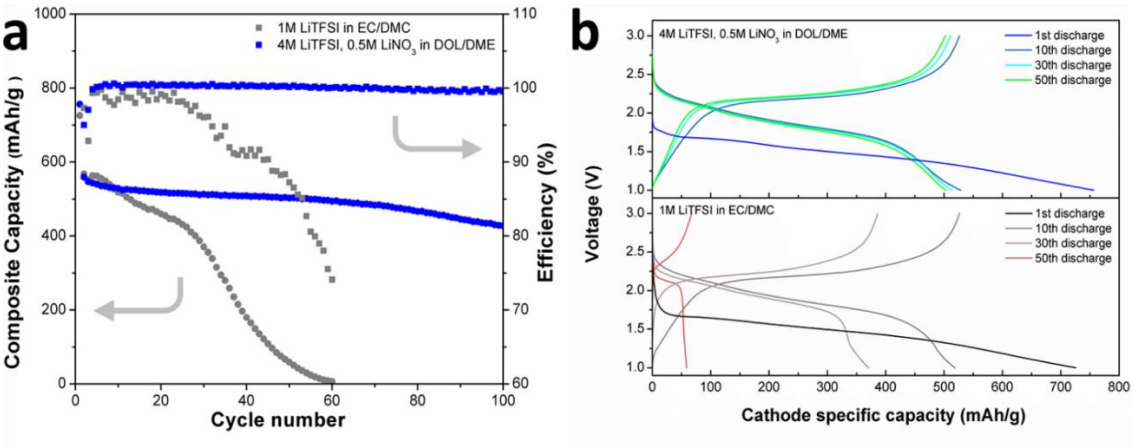

Figure 3.5 Evaluation of full cell performance with limited lithium capacity anode. (a) Cycling performance at a current density of 100 mA/g, and (b) 10^{th},30^{th}, 50^{th} discharge and charge voltage profiles of SPAN cathode with deficient lithium anode in different electrolyte.

3.6 Supporting information

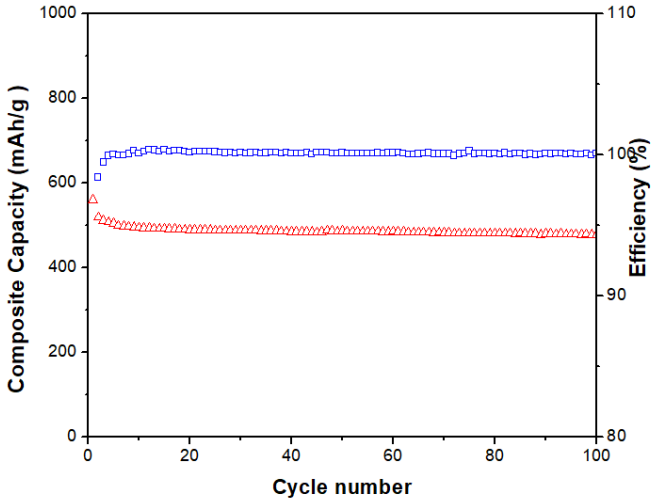

Figure 3.6 Cycling performance of SPAN cathode with lithium anode in 1M LiTFSI EC/DMC electrolyte.

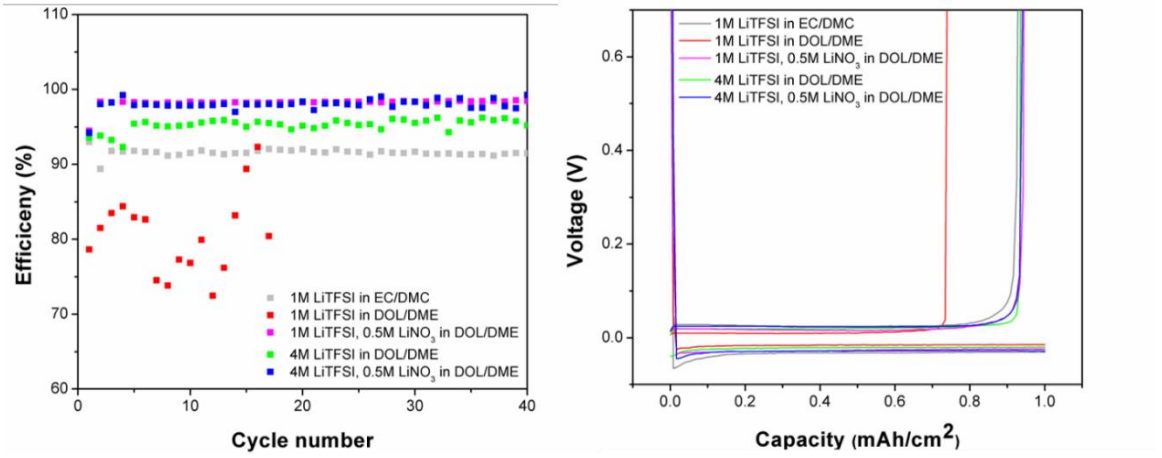

Figure 3.7 Electro-chemical evaluation of electrolytes. CE tests of Li-Cu cells with different electrolyte (current density and capacity of lithium deposition are 0.5 mA/cm^2 and 1 mAh/cm^2).

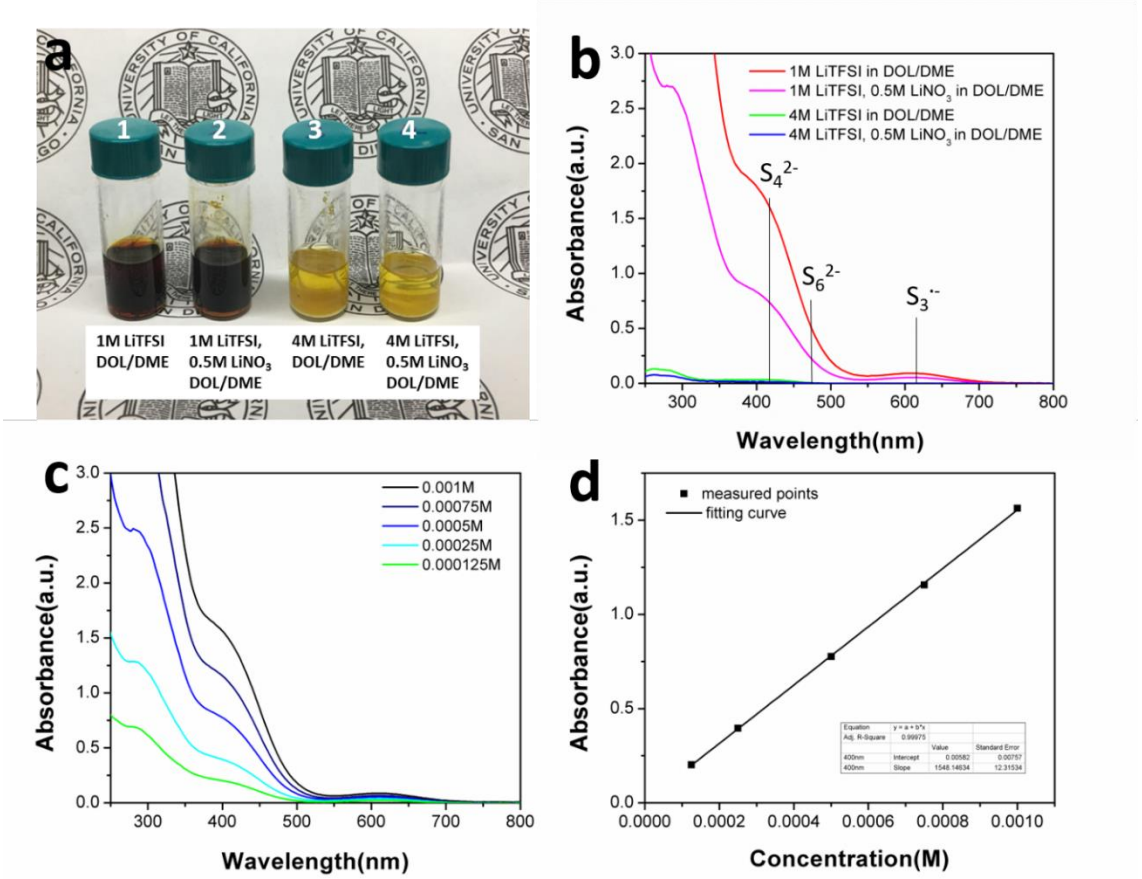

Figure 3.8 A) Photograph of 0.25 M Li_2S_6 in 1 M LiTFSI in DOL/DME, 1 M LiTFSI and 0.5 M $LiNO_3$ in DOL/DME, 4 M LiTFSI in DOL/DME, 4 M LiTFSI and 0.5 M $LiNO_3$ in DOL/DME (from left to right). (B) The corresponding UV/Vis spectra of 0.25 M Li_2S_6 in electrolytes after dilution (C) (D)UV/Vis spectra with different concentration Li_2S_6 in DOL/DME and fitting curve. UV band attribution: S_6^{2-} at 475 nm, S_4^{2-} at 420 nm, $S_3^{\bullet-}$ at 617 nm.

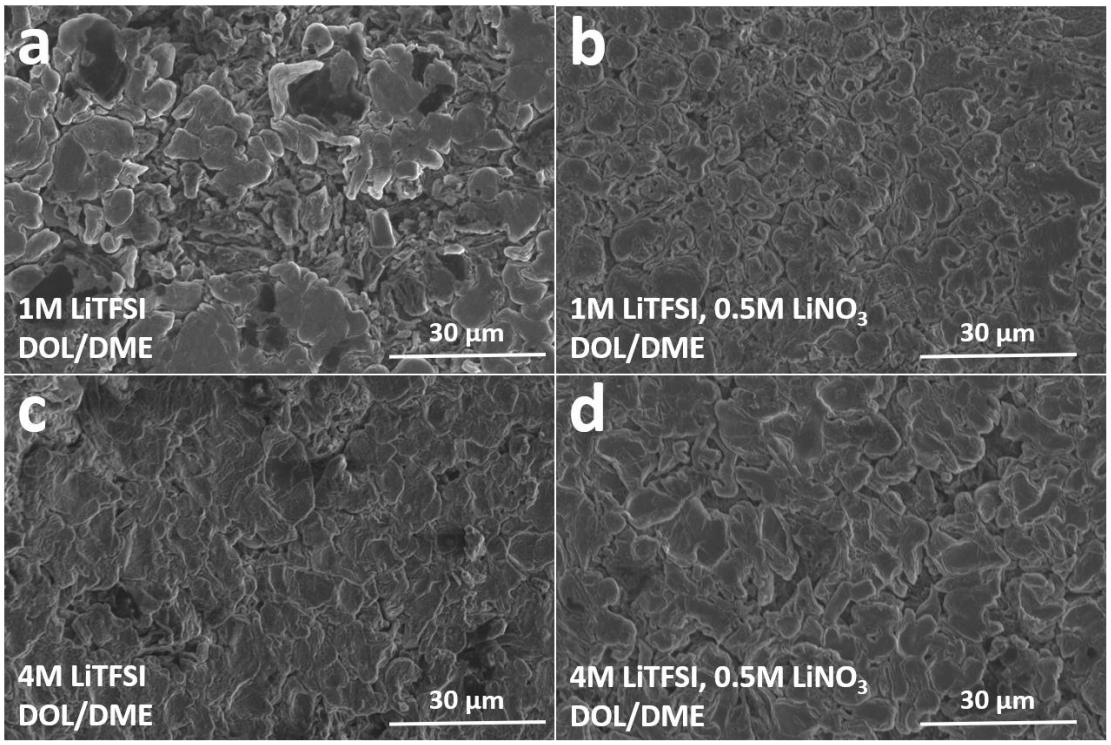

Figure 3.9 Top view SEM images of cycled lithium anode surface in (A) 1M LiTFSI in DOL/DME, (B) 1M LiTFSI and 0.5M $LiNO_3$ in DOL/DME, (C) 4M LiTFSI in DOL/DME, (D) 4M LiTFSI and 0.5M $LiNO_3$ in DOL/DME.

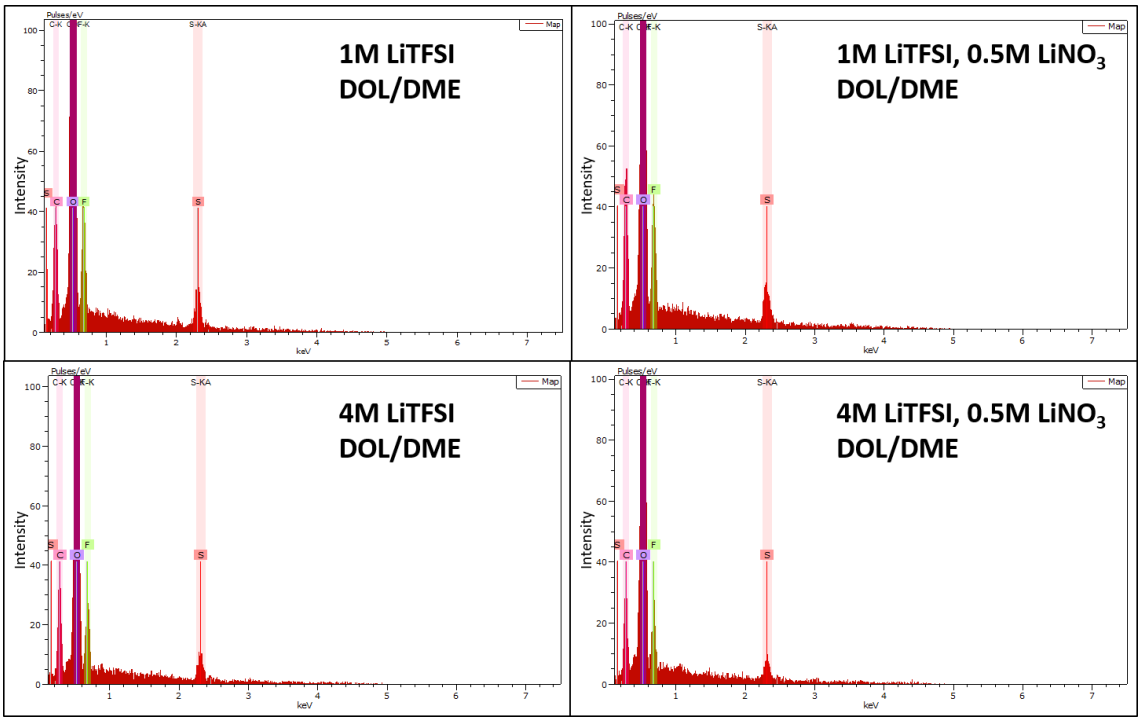

Figure 3.10 EDS of cycled lithium anode surface in (A) 1 M LiTFSI in DOL/DME, (B) 1 M LiTFSI and 0.5 M $LiNO_3$ in DOL/DME, (C) 4 M LiTFSI in DOL/DME, (D) 4 M LiTFSI and 0.5 M $LiNO_3$ in DOL/DME.

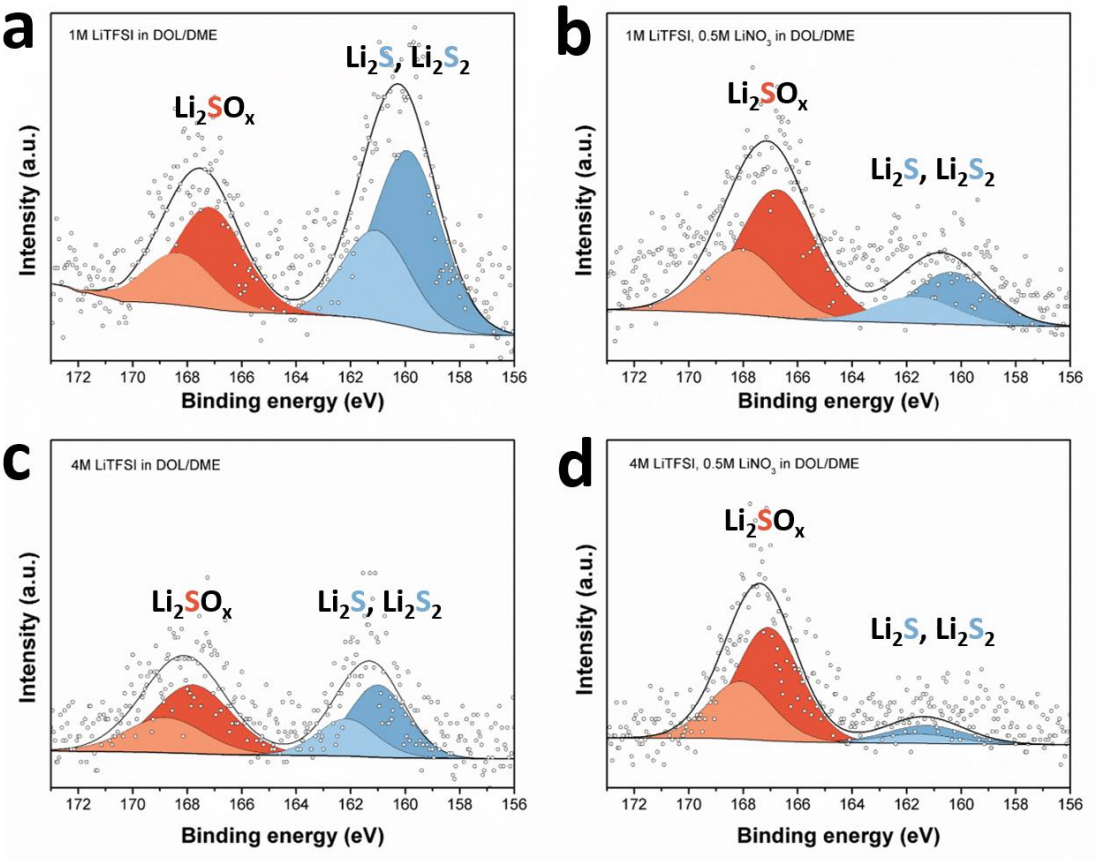

Figure 3.11 XPS S2p spectra of cycled lithium anode surface in (A) 1 M LiTFSI in DOL/DME, (B) 1 M LiTFSI and 0.5 M $LiNO_3$ in DOL/DME, (C) 4 M LiTFSI in DOL/DME, (D) 4 M LiTFSI and 0.5 M $LiNO_3$ in DOL/DME.

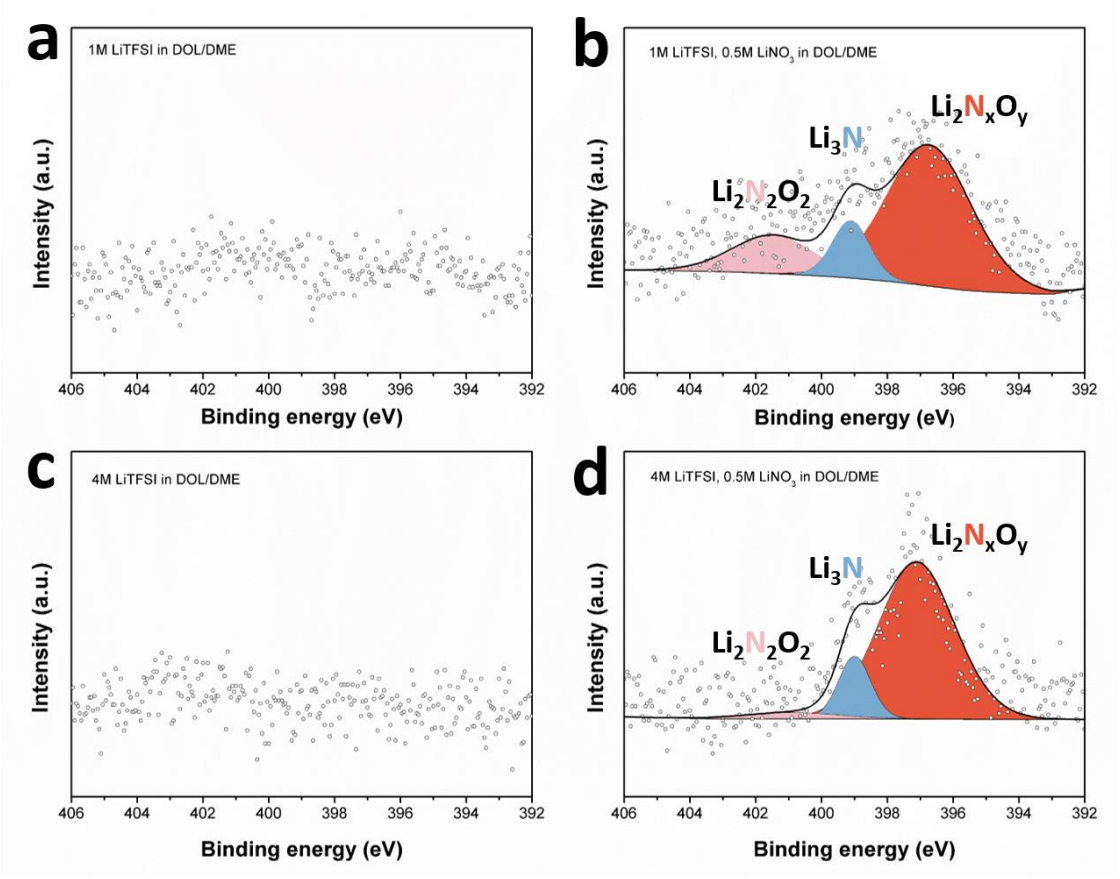

Figure 3.12 XPS N1s spectra of cycled lithium anode surface in (A) 1 M LiTFSI in DOL/DME, (B) 1 M LiTFSI and 0.5 M $LiNO_3$ in DOL/DME, (C) 4 M LiTFSI in DOL/DME, (D) 4 M LiTFSI and 0.5 M $LiNO_3$ in DOL/DME.

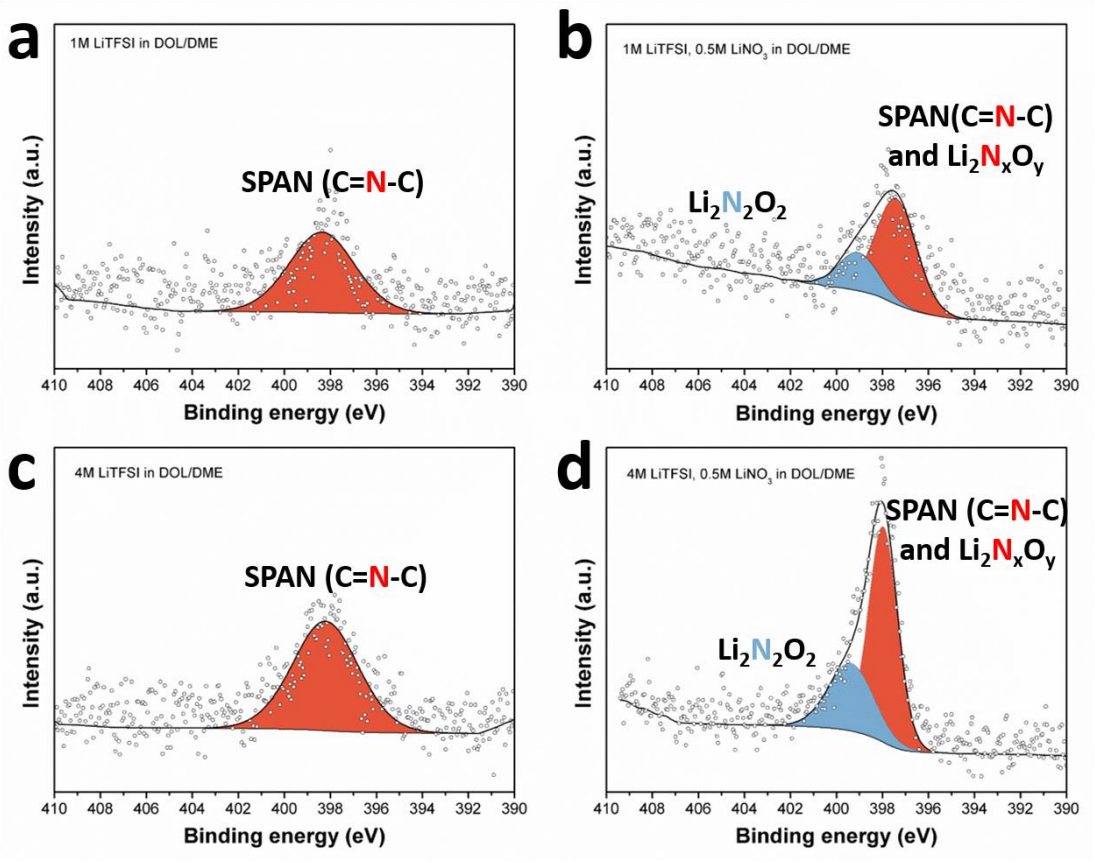

Figure 3.13 XPS N1s spectra of cycled SPAN cathode surface in (A) 1 M LiTFSI in DOL/DME, (B) 1 M LiTFSI and 0.5 M $LiNO_3$ in DOL/DME, (C) 4 M LiTFSI in DOL/DME, (D) 4M LiTFSI and 0.5 M $LiNO_3$ in DOL/DME.

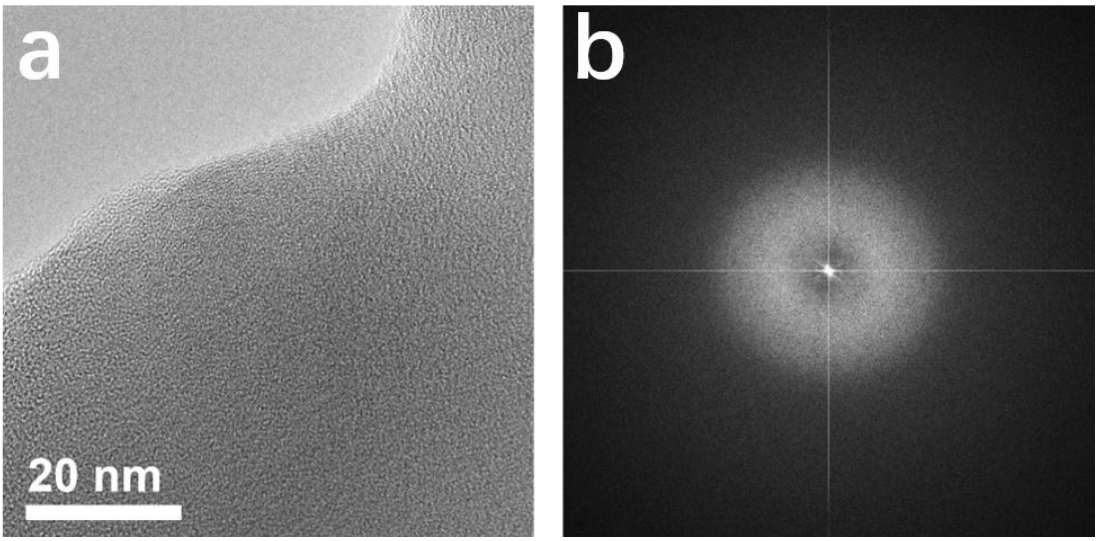

Figure 3.14 (A) TEM image and (B) selected area electron diffraction (SAED) image of raw SPAN powder.

Material	Areal loading mg/cm²	Current density	Sulfur content	Reversible specific capacity mAh/g
$S_{1-x}Se_x$/C[1]	0.8-1.5	0.2 A/g	50%	553(1106)
S/PAN/$Mg_{0.6}Ni_{0.4}O$[2]	1.23	0.1 C	38.5%	470.8(1223)
SVF[3]	6.37	0.2C	37.78%	474(1255)
SPAN[4]	1	0.2 C	45%	571.5(1270)
MSPAN[5]	2.45	0.1 C	45.87%	609.14(1330)
$Se_{0.06}$SPAN[6]	1-3	0.4 A/g	40.9%	546 (1334)
SPAN[7]	0.38	0.1 A/g	45.6%	620(1360)
SPAN[8]	1.2	0.33 A/g	46%	657.8(1430)
SPAN/RGO[9]	2-2.8	0.1 C	44%	645.5(1467)
pPAN-S/GNS[10]	N/A	0.07 A/g	47%	700 (1500)
SPAN/CNT[11]	2.1-2.6	0.13 A/g	40%	644 (1610)
This work	**1.5**	**0.1 A/g**	**41.16%**	**560.3 (1361.2)**

Figure 3.15 A summary of the specific capacities of SPAN materials.

Elemental	C	H	N	O	S
contents	40.08 %	0.30 %	14.83 %	3.40 %	41.16 %

Figure 3.16 Elemental analysis of synthesized SPAN raw material.

3.7 Acknowledgements

This work was supported by the Office of Vehicle Technologies of the U.S. Department of Energy through the Advanced Battery Materials Research (BMR) Program (Battery500 Consortium) under Contract No. DE-EE0007764.

Chapter 3, in full, is a reprint of materials published in the following paper: Xing Xing, Yejing Li, Xuefeng Wang, Victoria Petrova, Haodong Liu* and Ping Liu*, “Cathode electrolyte interface enabling stable Li-S batteries" *Energy Storage Materials.*, **2019**, 21, 474-480. The dissertation author was the primary author for the data presented and was the primary author of this publication. The permissions to reproduce this material were granted by the Elsevier B.V., copyright 2019.

Chapter 4: Long Calendar Life Silicon Composite Thin Film Anode

4.1 Introduction

In the last two decades, lithium-ion batteries (LIBs) have been considered as an ideal energy storage system due to their high energy density and long cycle life, thus extensively applied in portable electronic devices, the energy grid and EVs. However, current commercial graphite-based anode material, with a moderate theoretical capacity of 372 mAh g^{-1}, cannot satisfy the energy and power demand of current and future applications[14,135,137,152,156]. Therefore, development of higher energy density anode material is imperative for next generation batteries.

Silicon (Si) has become a promising candidate anode material for high energy density LIBs for a few reasons. First, Si possesses the highest theoretical specific gravimetric capacity (4200 mAh g^{-1}, lithiated to $Li_{4.4}Si$) and volumetric capacity (9786 mAh cm^{-3})[94,97,100,183,184]. Second, Si exhibits a low discharge potential at an average of 0.4 V vs Li^+/Li. The increased potential compared to graphite reduces the likelihood of lithium metal plating and alleviate the major safety concern on short-circuit. Third, Si is the second richest element in the earth crust, implying its potential to achieve low-cost and be environmentally friendly[101,106,107,116].

In order to substitute graphite with Si-based anode in commercial batteries, its lifetime, as one of the most important characteristics, should be well understood. The lifetime of LIBs includes both cycle life and calendar life. The cycle life of LIBs is determined by testing the reversible capacity retention during continuous cycling. The

calendar life of LIBs is tested by measuring the capacity retention after the cells rest at certain state of charge and temperatures.

Currently, the drastic volume change of Si (~360% for $Li_{4.4}Si$) hinders its cycle life[93,96,98,102,104]. The induced stress and strain due to this volume variation cause severe material collapse and electrical isolations. The electrode structure integrity deteriorates due to the gradual pulverization after cycling. In addition, there would be delamination and disconnection between electrode and substrate due to the interfacial stress. Moreover, continuous solid electrolyte interface (SEI) breaking and reformation at anode surface due to volume change cause a continuous consumption of electrolyte and active lithium ions. All these processes accelerate the electrode degradation on capacity and efficiency. Various strategies have been investigated to solve this problem including the use of nanomaterials and sophisticated microstructure controls which have significantly improved the cycle life.

However, the poor calendar life of Si anode has become another obstacle towards commercialization. Previous studies have suggested that the cycle life of LIBs using graphite anodes was generally attributed to the lithium consuming parasitic reactions between anode and electrolyte. Similar observations were reported for the calendar life of LIBs using Si-based anodes and the impact of state of charge on the calendar life was also studied. Lu at el. reported that the capacity of the Si-based electrode was found to decrease not only with cycles but also with rest time, due to the Li ion consuming parasitic reactions

on anode surface[101,116]. They claimed that time, not cycle count, is the dominant contributor to the capacity fading. In this case, the calendar life of Si-based anode needs to be optimized for the future commercial applications of Si anode.

In this work, we proposed a multilayer Si-based anode to ensure both cycle life and calendar life. In order to confine the volume change of Si as well as mitigate the parasitic reactions, a physical confinement and barrier would be a desirable solution. An ideal protection material would be chosen based on a few criteria. First, as a protection layer, it is expected to possess both electronic and ionic conductivity to ensure fast charge transport. Second, a stable solid electrolyte interface (SEI) on the protection layer is expected to ensure the cycling efficiency. In addition, it is desirable that the protection material could control meaningful capacity.

A disordered rock salt $Li_{3+x}V_2O_5$ (LVO) has been reported as a fast-charging anode material by Liu's group[185]. As an anode material, it performs over 1000 charge-discharge cycles with negligible capacity decay, implying the stable SEI on the surface of LVO. An exceptional rate capability is observed that delivers over 40% capacity in 20 seconds. Considering the high current density, high electronic and ionic conductivities are expected. In addition, it delivers over 120 mAh g^{-1} capacity at about 0.6 V vs. Li/Li^+, which perfectly matches the cycling voltage range of Si anode. As a result, LVO is an ideal protection material for Si anode, in order to extend the cell cycle life and calendar life.

In this work, a thorough comparison of cycle life and calendar life is performed between Si anode and Si-LVO multilayer anode. The structure of Si-LVO after cycling have been examined, which further demonstrates the LVO protection function on maintaining the structure integrity. Indeed, the designed multilayer anode not only shows excellent cycle life and calendar life, but also points out a new strategy on anode material optimization towards long life LIBs.

4.2 Experiment section

Thin film fabrication

All materials were purchased from Sigma-Aldrich unless specified otherwise and used without purification.

The thin films were deposited via electron-beam evaporation. As prepared Si or Vanadium Oxide (V_2O_5) powder was placed into a graphite crucible as target material. The Cu foil was attached onto the substrate holder after cleaning as deposition substrate. The deposition rate was set as 0.2 nm/s for all materials. The film thickness was monitored by a quartz crystal microbalance during deposition. After deposition, V_2O_5 containing film was treated at 350dc for 4 hours to complete crystalization before being assembled into cells. The annealed films were punched into 13 mm diameter circle and directly used as electrode for coin cell fabrications.

Electrochemical characterizations

All the electrochemical tests are performed in coin cells, and the fabrications were operated inside an Ar-filled glove box with water content less than 1 ppm.

Ethyl methyl carbonate (EMC), ethylene carbonate (EC), dimethyl carbonate (DMC), vinylene carbonate (VC), fluoroethylene carbonate (FEC) were purchased from BASF and used as received. The electrolyte was prepared by dissolving predetermined amounts of $LiPF_6$ into pre-mixed solvents and stirred to achieve stable and clear solutions. The weight contents of all compositions in the electrolyte are 40 % EMC, 24 % EC, 16% DMC, 5% FEC, 1% VC and 14% $LiPF_6$.

Cycling performance of thin film electrode tests were measured with Li counter electrodes in 2032-type coin cells, using LAND battery testers (Wuhan, China). Typically, a flooded amount of electrolyte and a separator (Celgard) were applied. A 250 μm thick lithium metal chip was used as anode material. The cut-off voltage is 0.01 V - 2 V. First of all, the Li-thin film cells underwent 3 formation cycles at current density of 0.02 mA/cm^2 for first 3 cycle, then multi cycling tests were applied to the cells at 0.06 mA/cm^2 current density.

The calendar life tests were performed when the electrode was in its discharged (lithiated) state. At certain cycle, the cell was discharged to fully lithiate the thin film material, and then the cycling current was cut off. The cell was rested at room temperature

or 55ºC. After 24 hours, the cell was set back to cycle with same cycling conditions. Same operation was repeated to reproduce a calendar life test data.

Structure characterization

X-ray diffractometry (XRD, Bruker, D2 Phaser) with Cu-Kα radiation was conducted to analyze crystal structure of the thin films. The morphology of the cycled lithium anode surface was characterized using scanning electron microscopy (FEI Quanta 250 SEM) coupled with an energy dispersive X-ray spectrometer (EDX) to determine the chemical composition of the samples. 5 kV and 0,1 mA condition were applied during SEM tests.

4.3 Results and discussion

Si and V_2O_5 multilayer thin films were deposited on Cu substrate via e-beam evaporation. A 200 nm thick Si thin film on Cu substrate was chosen as the baseline anode material. In order to physically protect the Si film, 300 nm thick V_2O_5 film was deposited on both top and bottom of the Si film, followed by an annealing process to achieve crystalline phase of V_2O_5. The crystalline structures of deposited thin films have been confirmed by XRD. As shown in Figure 4.5, The multilayer only showed Cu related peaks before annealing, implying the amorphous structure of V_2O_5 after deposition. However, crystalline structure showed up after the annealing process as the arrow indicated. As

previously reported, the crystalline phase of V_2O_5 is expected to deliver considerable mixed conductivity with highly reversible cycling capacity[185]. Thus, the Si-V_2O_5 multiplayer film was expected to have excellent electrochemical cycling performance.

SEM was performed to further analyze the structure of the multilayer film. As shown in the top-view image in Figure 4.1a, the top surface of the multilayer film was quite smooth after annealing without any cracks or delamination. The multilayer film thickness was measured as well via cross-sectional SEM image shown in Figure 4.1b. The total thickness was about 800 nm, which is consistent with the value that e-beam evaporator sensor indicated. Elemental analysis was applied to determine the composition of the thin film. As shown in Figure 4.1c and 4.1d, element Si signals were concentrated at the center of the film, and element V signals located at the top and bottom surface, implying an expected sandwich structure of Si and V_2O_5. We thus conclude that the multilayer deposition design has been successfully achieved.

The baseline Si thin film was tested in a Li- Si thin film cell and shown in Figure 4.2a and 4.2b. At first discharge, the cell showed over 3300 mAgh/g specific capacity with a ~0.2 V average voltage, corresponding to about 0.19 mAh/cm^2 anode areal capacity. However, due to the large irreversible capacity, after 3 formation cycles, there were only ~1600 mAh/g specific capacity of Si left. The cell capacity retention is about 36% after 100 cycles, corresponding to 0.08 mAh/cm^2 anode areal capacity. This fast capacity decay was also observed in the voltage profiles shown in Figure 4.2b. The plausible explanation

is that the parasitic reaction not only decrease the cell capacity, but also increase the resistance of the cell. After 100 cycles, the cell was disassembled to check the morphology of the Si thin film. As shown in Figure 4.5, the Si film could not maintain its integrity and it was fully delaminated from Cu substrate. This observation is consistent with previously reported results and provides explanation for the poor electrochemical behavior. In summary, the Si thin film has a limited cycle life due to fast cycling capacity degradation as well as a severe structure mechanical failure.

In comparison, the multilayer film was also tested in Li-thin film cells. As shown in Figure 4.2c and 4.2d, there is an irresistible capacity loss after 1st discharge, causing the specific capacity based on total composite weight decreasing from 790 mAh/g to 510 mAh/g. As noted in the 1st discharge voltage profile, there were multiple short voltage plateaus between 2.5 V and 0.5 V, which corresponds to the V_2O_5 lithiation process[185]. Thus, the irreversible capacity at 1st discharge theoretically came from both Si and V_2O_5. Starting from 1st charge, the voltage profile was quite smooth between 0.01 V and 2 V, due to the combined lithiation processes of Si and V_2O_5. As shown in Figure 4.2c, there was 0.16 mAh/cm^2 highly reversible areal capacity, doubling the baseline Si thin film anode. More significantly, starting from 4th cycle, the cell maintained about 100% of the capacity after 100 cycles, which is indeed remarkable. The excellent cyclability of the multilayer deposition confirms our hypothesis that the V_2O_5 protection improves the Si-based anode cycle life.

To verify the improvements from V_2O_5 protection on calendar life, a cell-resting tests were performed. Same cell configurations as cycle life tests applied to the tests. After 3 formation cycle at a small current density, the cells were cycled at C/5 rate. After the 5^{th} discharge, the cells were disconnected from the battery tester, and rested at elevated temperature, 55ºC for 24 hours, followed by a cooling down process for about 1 hour. The cells were then started with the 5^{th} charging process. Same processes were repeated one more time before turning back to constant current cycles. As shown in Figure 4.3a and 4.3b, a Li-Si thin film cell started with over 2000 mAh/g discharge specific capacity at 5^{th} discharge. However, after resting at elevated temperature, there was only ~1000 mAh/g specific capacity left, with a less than 50% CE. The same capacity was maintained at the 6^{th} cycle, followed by continuous capacity decay during subsequent constant current cycling. Moreover, as we noted that, at discharged state, the potential of Si anode was supposed to be similar to that of Li metal. However, over 0.6 V open circuit voltage (OCV) was observed before 5^{th} and 6^{th} charging after resting, implying a large loss of Li-ion. As a conclusion, both the OCV increase and the CE decrease indicated that the parasitic reactions between anode and electrolyte severely affect the calendar life of the Si-based anode.

As shown in Figure 4.3c and 4.3d, the Li-multilayer thin film cells showed a significantly improved calendar life. With V_2O_5 protection, the cell showed a ~520 mAh/g reversible specific after 3 formation cycles. After the resting processes at elevated

temperature, the CE was 86% for 5th cycle and 87% for 6th cycle, significantly improved from baseline Si thin film cells. Moreover, there was no capacity decay in the following constant current cycles, even showing a slight capacity recovery. In Figure 4.3d, the OCV at the beginning of the 5th charge and 6th charge are around 0.4 V, implying the minimum amount of Li-ion loss. Clearly, with V_2O_5 protection, same thickness Si thin film anode displayed a highly improved calendar life.

In order to further evaluate calendar life, more tests were performed at room temperature. As shown in Fugire 4.4, the charge and discharge areal capacity of Si thin film in the first 3 formation cycles are ~0.14 mAh/cm^2. However, starting from 4th cycle, the areal capacity was only ~0.05 mAh/cm^2. The large capacity decrease implies the poor kinetics of the Si thin film, which is consistent with the data shown in Figure 2. Starting from 4th cycle, as shown in Figure 4.4, each cycle-test consisted of 10 repeating cycles and a 24-hour rest at the discharged state. Si thin film cell showed a clear decreasing trend in both CE and capacity retention. In addition to the quick capacity decay at non-rest cycles, the average CE at rest cycle was only about 92%, resulting from severe parasitic reactions. After 53 cycles, the Si thin film anode cell only maintained 0.03 mAh/cm^2 areal capacity.

The same calendar life test methodology was applied to multilayer thin film cells as well. As shown in Figure 4.4b, the first 3 formation cycle delivered 0.13 mAh/cm^2 areal capacity, which dropped to 0.09 mAh/cm^2 at 4th cycle due to current density increase. As a reminder, Si thin film cell lost over 65% capacity at 4th cycle. Moreover, the average CE of

rest cycle was about 96%, a significant improvement from Si thin film cell rest tests. After 53 cycles, there was 0.08 mAh/cm^2 capacity remaining. In summary, an improved calendar life from multilayer thin film cells was demonstrated at both elevated temperature and room temperature.

However, as we noticed, there was capacity loss of Li-multilayer cells after long cycles. In order to understand the decay mechanism and further improve the cell performance, SEM has been performed for dissembled cycled cells. As shown in Figure 4.6, the multilayer film was wrinkled and partially delaminated from Cu substrate after cycling. These observations provide the evidence for the reason of the slight capacity decay. In Figure 4.6b, the EDX mapping clearly displayed the multilayer film structure after cycleing , implying the three layers were still adhered well while delaminated from substrate together. This observation confirmed the V_2O_5 function as a physical barrier and confinement. If the volume expansion, which caused the delamination, could be eliminated, the cycling behavior would be optimized. Further work will be performed on the structure configuration optimizations.

4.4 Conclusion

In summary, we report a multi-layered Si-based thin film composite anode, thus achieving a long life, high capacity anode in LIBs. V_2O_5 as a mixed conductive anode material is demonstrated as a protection material for Si. With V_2O_5 as physical confinement

and barrier, the performance loss triggered by Si volume change and parasitic reactions with electrolyte are significantly minimized. Longer cycle life and calendar life of Si-based anode material were achieved compared to baseline Si thin film cells. This work provides a simple and novel method for high energy density, long life Si anode towards commercial applications. However, delamination and wrinkles were found after cycling, thus more microstructure optimizations are needed to further improve the performance of multilayer anode.

4.5 Figures

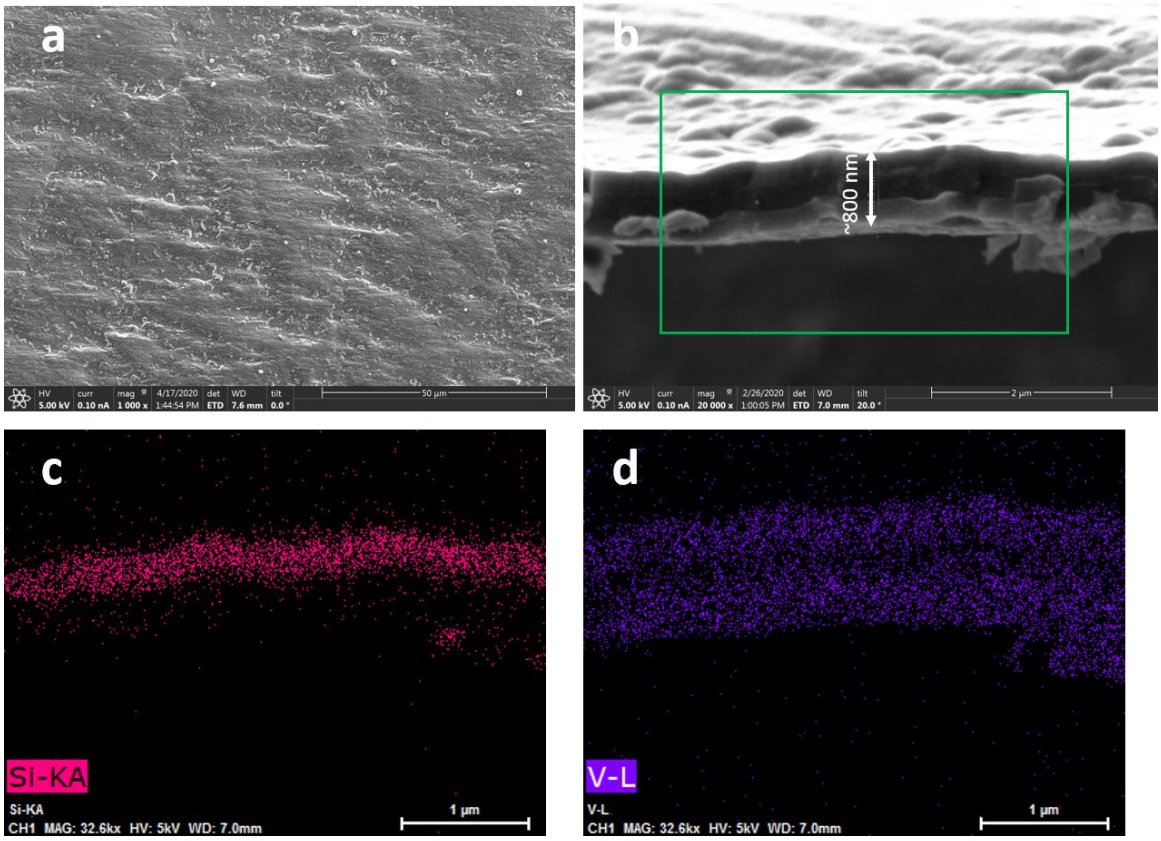

Figure 4.1 (a), (b) SEM images and (c), (d) EDX mappings of multilayer deposition thin film. The Si layer thickness is 200 nm and the two V2O5 film thickness are 300 nm.

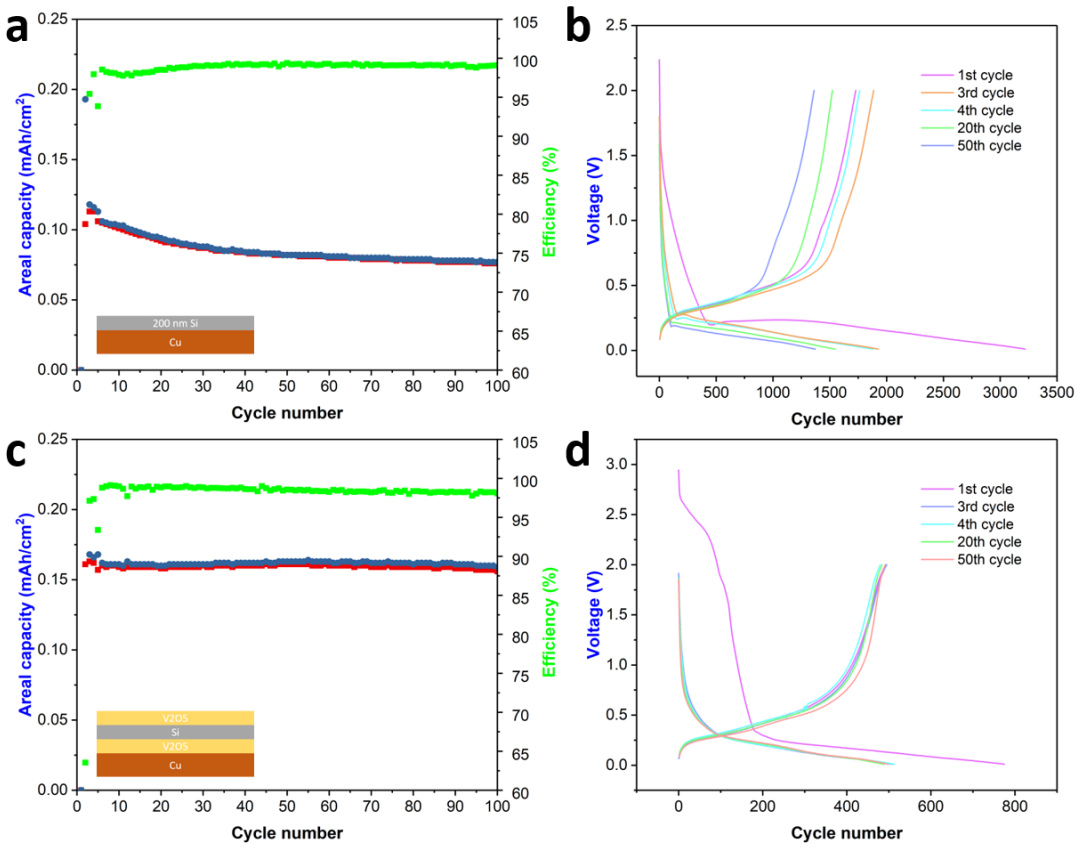

Figure 4.2 Cycling performance of (a) Si thin film, (c) multilayer deposition thin film half-cell, voltage profiles of (b) Si thin film, (d) multilayer deposition thin film half-cell. 0.02 mA/cm^2 for first 3 cycle, then 0.06mA/cm^2.

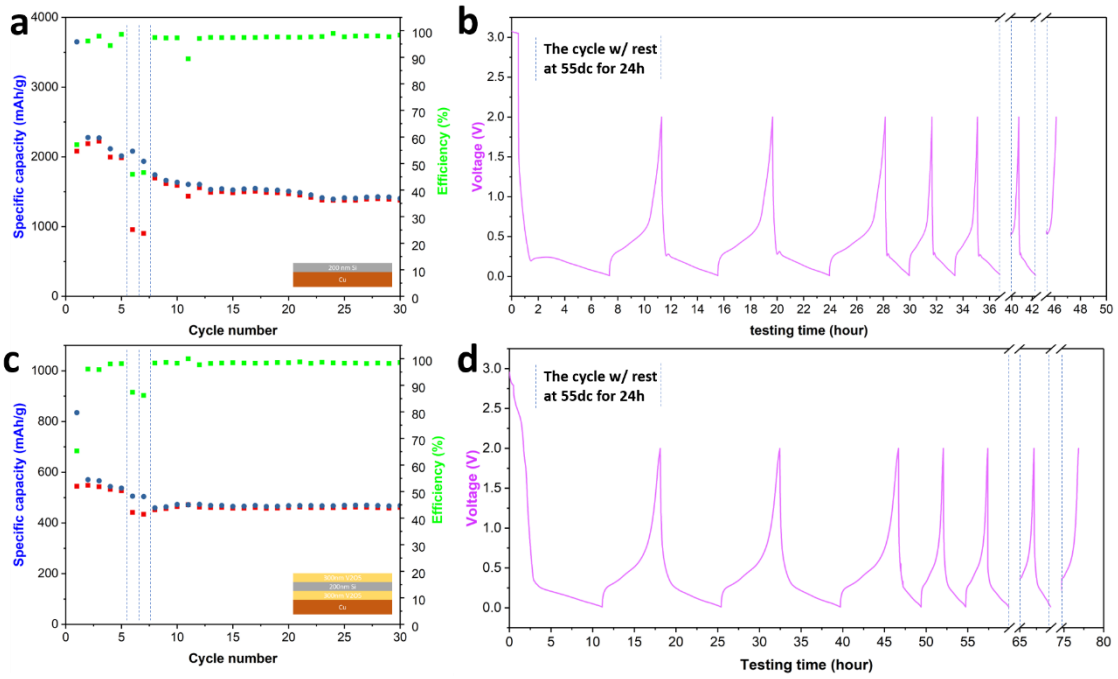

Figure 4.3 Calendar life test at elevated temperature. Cycling performance of (a) Si thin film, (c) multilayer deposition thin film half-cell, voltage profiles of (b) Si thin film, (d) multilayer deposition thin film half-cell. 0.02 mA/cm^2 for first 3 cycle, then 0.06mA/cm^2. The cells were tested at 55dc for 24 hours at discharged state for the calendar life test, and after cooling down, the cells were charged at room temperature.

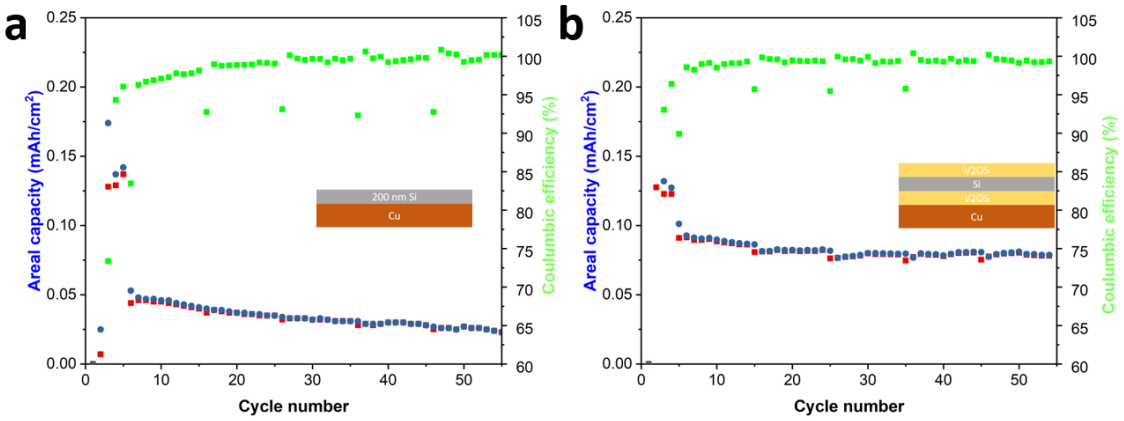

Figure 4.4 Calendar life test at room temperature. Cycling performance of (a) Si thin film, (c) multilayer deposition thin film half-cell.0.02 mA/cm^2 for first 3 cycle, then 0.06mA/cm^2. The cells were rested at room temperature for 24 hours at certain cycled at discharged state.

4.6 Supporting information

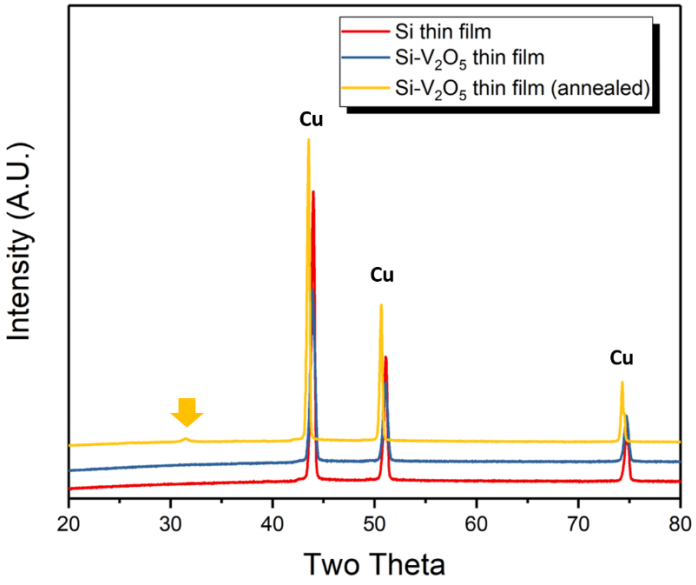

Figure 4.5 XRD spectra of Si thin film, Si-V_2O_5 thin film and Si-V_2O_5 thin film after annealing.

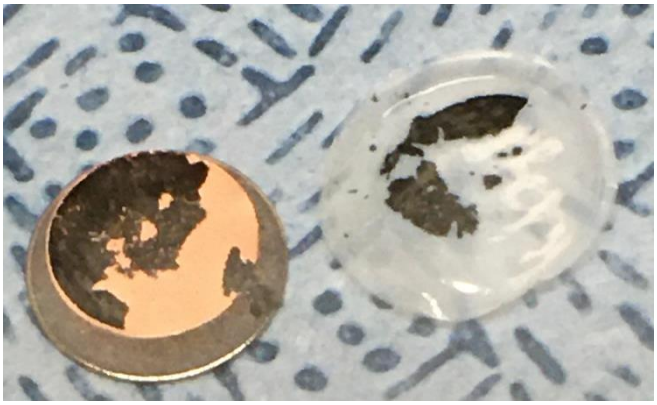

Figure 4.6 Photography of disassembled Si thin film cell after cycles.

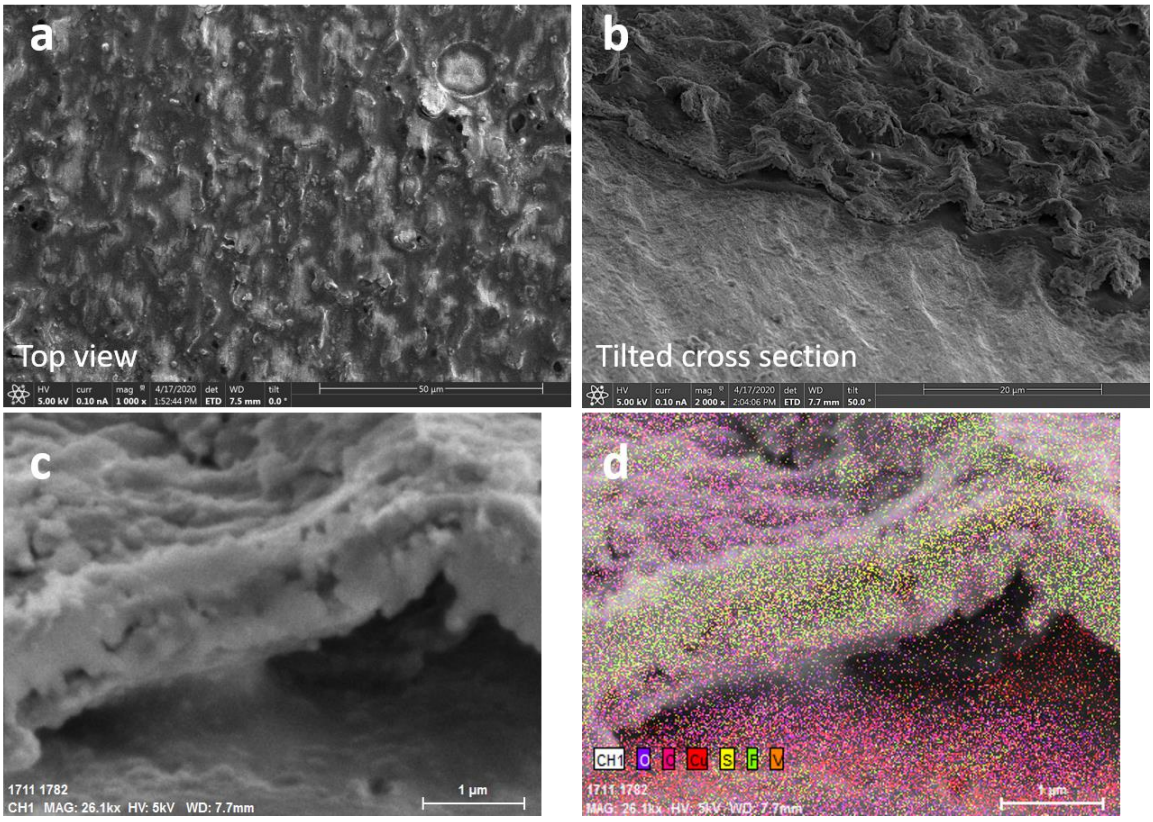

Figure 4.6 (a), (b), (c) SEM images and (d) EDX mapping of cycled multilayer deposition thin film cell after cycles

References

[1] S. Xin, Y. You, S. Wang, H. C. Gao, Y. X. Yin, Y. G. Guo, *ACS Energy Lett.* **2017**, *2*, 1385.

[2] A. Manthiram, X. Yu, S. Wang, *Nat. Rev. Mater.* **2017**, *2*, 1.

[3] C. Sun, J. Liu, Y. Gong, D. P. Wilkinson, J. Zhang, *Nano Energy* **2017**, *33*, 363.

[4] F. Wu, G. Yushin, *Energy Environ. Sci.* **2017**, *10*, 435.

[5] Y. Guo, H. Li, T. Zhai, *Adv. Mater.* **2017**, *29*, 1.

[6] C. Yang, K. Fu, Y. Zhang, E. Hitz, L. Hu, *Adv. Mater.* **2017**, *29*, 1.

[7] Q. Liu, Z. Geng, C. Han, Y. Fu, S. Li, Y. bing He, F. Kang, B. Li, *J. Power Sources* **2018**, *389*, 120.

[8] Z. Gao, H. Sun, L. Fu, F. Ye, Y. Zhang, W. Luo, Y. Huang, *Adv. Mater.* **2018**, *30*, 1.

[9] L. Fan, S. Wei, S. Li, Q. Li, Y. Lu, *Adv. Energy Mater.* **2018**, *8*, 1.

[10] X. Judez, G. G. Eshetu, C. Li, L. M. Rodriguez-Martinez, H. Zhang, M. Armand, *Joule* **2018**, *2*, 2208.

[11] Ö. U. Kudu, T. Famprikis, B. Fleutot, M. D. Braida, T. Le Mercier, M. S. Islam, C. Masquelier, *J. Power Sources* **2018**, *407*, 31.

[12] M. Falco, S. Ferrari, G. B. Appetecchi, C. Gerbaldi, *Mol. Syst. Des. Eng.* **2019**, *4*, 850.

[13] S. A. Pervez, M. A. Cambaz, V. Thangadurai, M. Fichtner, *ACS Appl. Mater. Interfaces* **2019**, *11*, 22029.

[14] H. Wang, D. Yu, C. Kuang, L. Cheng, W. Li, X. Feng, Z. Zhang, X. Zhang, Y. Zhang, *Chem* **2019**, *5*, 313.

[15] S. Xia, X. Wu, Z. Zhang, Y. Cui, W. Liu, *Chem* **2019**, *5*, 753.

[16] M. Du, K. Liao, Q. Lu, Z. Shao, *Energy Environ. Sci.* **2019**, *12*, 1780.

[17] Z. Wu, Z. Xie, A. Yoshida, Z. Wang, X. Hao, A. Abudula, G. Guan, *Renew. Sustain. Energy Rev.* **2019**, *109*, 367.

[18] T. Famprikis, P. Canepa, J. A. Dawson, M. S. Islam, C. Masquelier, *Nat. Mater.* **2019**,

18, 1278.

[19] R. Chen, Q. Li, X. Yu, L. Chen, H. Li, *Chem. Rev.* **2020**, *120*, 6820.

[20] S. Randau, D. A. Weber, O. Kötz, R. Koerver, P. Braun, A. Weber, E. Ivers-Tiffée, T. Adermann, J. Kulisch, W. G. Zeier, F. H. Richter, J. Janek, *Nat. Energy* **2020**, *5*, 259.

[21] Y. Xiao, Y. Wang, S. H. Bo, J. C. Kim, L. J. Miara, G. Ceder, *Nat. Rev. Mater.* **2020**, *5*, 105.

[22] M. Winter, R. J. Brodd, *Chem. Rev.* **2004**, *104*, 4245.

[23] V. Murray, D. S. Hall, J. R. Dahn, *J. Electrochem. Soc.* **2019**, *166*, A329.

[24] J. Liu, Z. Bao, Y. Cui, E. J. Dufek, J. B. Goodenough, P. Khalifah, Q. Li, B. Y. Liaw, P. Liu, A. Manthiram, Y. S. Meng, V. R. Subramanian, M. F. Toney, V. V. Viswanathan, M. S. Whittingham, J. Xiao, W. Xu, J. Yang, X. Q. Yang, J. G. Zhang, *Nat. Energy* **2019**, *4*, 180.

[25] T. T., *MRS Proc.* **1988**, *135*.

[26] H. Gerischer, C. W. Tobias, *Advances in electrochemical science and engineering*; 2008; Vol. 1.

[27] D. E. Fenton, J. M. Parker, P. V. Wright, *Polymer (Guildf).* **1973**, *14*, 589.

[28] P. Knauth, H. L.Tuller, *J. Am. Ceram. Soc.* **2002**, *85*, 1654.

[29] H. Li, Z. Wang, L. Chen, X. Huang, *Adv. Mater.* **2009**, *21*, 4593.

[30] Kato Y, Hori S, Saito T, Suzuki K, Hirayama M, Mitsui A, Yonemura M, Iba H, R. Kanno, *Nat. Energy* **2016**, *1*, 1.

[31] J. Li, C. Ma, M. Chi, C. Liang, N. J. Dudney, *Adv. Energy Mater.* **2015**, *5*.

[32] G. Oh, M. Hirayama, O. Kwon, K. Suzuki, R. Kanno, *Chem. Mater.* **2016**, *28*, 2634.

[33] F. Han, J. Yue, C. Chen, N. Zhao, X. Fan, Z. Ma, T. Gao, F. Wang, X. Guo, C. Wang, *Joule* **2018**, *2*, 497.

[34] Y. G. Lee, S. Fujiki, C. Jung, N. Suzuki, N. Yashiro, R. Omoda, D. S. Ko, T. Shiratsuchi, T. Sugimoto, S. Ryu, J. H. Ku, T. Watanabe, Y. Park, Y. Aihara, D. Im, I. T. Han, *Nat. Energy* **2020**, *5*, 299.

[35] H. D. Lim, H. K. Lim, X. Xing, B. S. Lee, H. Liu, C. Coaty, H. Kim, P. Liu, *Adv. Mater. Interfaces* **2018**, *5*, 1.

[36] H. D. Lim, X. Yue, X. Xing, V. Petrova, M. Gonzalez, H. Liu, P. Liu, *J. Mater. Chem. A* **2018**, *6*, 7370.

[37] Y. Li, X. Wang, H. Zhou, X. Xing, A. Banerjee, J. Holoubek, H. Liu, Y. S. Meng, P. Liu, *ACS Energy Lett.* **2020**, *5*, 955.

[38] S. Sen Chi, Y. Liu, N. Zhao, X. Guo, C. W. Nan, L. Z. Fan, *Energy Storage Mater.* **2019**, *17*, 309.

[39] K. Jeddi, M. Ghaznavi, P. Chen, *J. Mater. Chem. A* **2013**, *1*, 2769.

[40] K. Yan, Z. Lu, H. W. Lee, F. Xiong, P. C. Hsu, Y. Li, J. Zhao, S. Chu, Y. Cui, *Nat. Energy* **2016**, *1*.

[41] S. Kim, C. Jung, H. Kim, K. E. Thomas-Alyea, G. Yoon, B. Kim, M. E. Badding, Z. Song, J. M. Chang, J. Kim, D. Im, K. Kang, *Adv. Energy Mater.* **2020**, *10*.

[42] T. Krauskopf, B. Mogwitz, C. Rosenbach, W. G. Zeier, J. Janek, *Adv. Energy Mater.* **2019**, *9*.

[43] J. Park, D. Kim, W. A. Appiah, J. Song, K. Taek, K. Taek, J. Oh, J. Young, Y. Lee, M. Ryou, Y. Min, *Energy Storage Mater.* **2019**, *19*, 124.

[44] X. Yang, X. Li, K. Adair, H. Zhang, X. Sun, *Structural Design of Lithium–Sulfur Batteries: From Fundamental Research to Practical Application*; Springer Singapore, 2018; Vol. 1.

[45] Y. He, Z. Chang, S. Wu, H. Zhou, *J. Mater. Chem. A* **2018**, *6*, 6155.

[46] R. Kumar, J. Liu, J. Y. Hwang, Y. K. Sun, *J. Mater. Chem. A* **2018**, *6*, 11582.

[47] T. Ould Ely, D. Kamzabek, D. Chakraborty, M. F. Doherty, *ACS Appl. Energy Mater.* **2018**, *1*, 1783.

[48] J. Guo, Z. Yang, Y. Yu, L. A. Archer, **2013**.

[49] J. Fanous, M. Wegner, J. Grimminger, M. Rolff, M. B. M. Spera, M. Tenzer, M. R. Buchmeiser, *J. Mater. Chem.* **2012**, *22*, 23240.

[50] L. Yin, J. Wang, J. Yang, Y. Nuli, *J. Mater. Chem.* **2011**, *21*, 6807.

[51] L. Zhou, B. Schumann, Y. NuLi, J. Yang, J. Wang, W. Wei, *Electrochem. commun.* **2011**, *13*, 399.

[52] L. Wang, J. Zhao, X. He, C. Wan, *Electrochim. Acta* **2011**, *56*, 5252.

[53] J. Fanous, M. Wegner, J. Grimminger, Ä. Andresen, M. R. Buchmeiser, *Chem. Mater.* **2011**, *23*, 5024.

[54] L. Wang, X. He, J. Ren, W. Pu, J. Li, J. Gao, *Ionics (Kiel).* **2010**, *16*, 689.

[55] X. He, J. Ren, L. Wang, W. Pu, C. Jiang, C. Wan, *J. Power Sources* **2009**, *190*, 154.

[56] W. Pu, C. Wan, C. Jiang, X. He, L. Wang, J. Ren, *Ionics (Kiel).* **2008**, *15*, 477.

[57] W. Pu, X. He, J. Wang, L. Wang, C. Jiang, J. Ren, C. Wan, *Ionics (Kiel).* **2007**, *14*, 335.

[58] C. Ding, A. Konarov, M.-R. Babaa, P. Chen, Z. Bakenov, Y. Zhao, Y. Zhang, *J. Electrochem. Soc.* **2013**, *160*, A1194.

[59] L. Wang, X. He, W. Sun, J. Li, J. Gao, G. Tian, J. Wang, S. Fan, *RSC Adv.* **2013**, *3*, 3227.

[60] T. N. L. Doan, M. Ghaznavi, Y. Zhao, Y. Zhang, A. Konarov, M. Sadhu, R. Tangirala, P. Chen, *J. Power Sources* **2013**, *241*, 61.

[61] J. Fanous, M. Wegner, M. B. M. Spera, M. R. Buchmeiser, *J. Electrochem. Soc.* **2013**, *160*, A1169.

[62] L. Wang, X. He, J. Li, J. Gao, J. Guo, C. Jiang, C. Wan, *J. Mater. Chem.* **2012**, *22*, 22077.

[63] M. Chen, L. Wang, J. Li, C. Jiang, X. He, J. Gao, *Electrochim. Acta* **2012**, *72*, 114.

[64] L. Yin, J. Wang, F. Lin, J. Yang, Y. Nuli, *Energy Environ. Sci.* **2012**, *5*, 6966.

[65] C. R. Stoldt, J. E. Trevey, J. R. Gilsdorf, P. Liu, S.-H. Lee, *J. Electrochem. Soc.* **2012**, *159*, A1019.

[66] M. U. M. Patel, M. Gaberscek, R. Dominko, R. Demir-Cakan, M. Morcrette, J.-M. Tarascon, *ChemSusChem* **2013**, *6*, 1177.

[67] J. K. Pugh, X. Zhang, R. Kostecki, T. J. Richardson, P. N. Ross, *J. Electrochem. Soc.* **2002**, *148*, A1341.

[68] X. He, Y. Wang, C. Wan, C. Jiang, J. Wang, J. Ren, *J. Power Sources* **2004**, *138*, 271.

[69] X. G. Yu, J. Y. Xie, J. Yang, H. jiang Huang, K. Wang, Z. S. Wen, *J. Electroanal. Chem.* **2004**, *573*, 121.

[70] J. Wang, J. Yang, C. Wan, K. Du, J. Xie, N. Xu, *Adv. Funct. Mater.* **2003**, *13*, 487.

[71] V. This, C. These, *Adv. Mater.* **2002**, *14*, 963.

[72] X. Yu, J. Xie, J. Yang, K. Wang, *J. Power Sources* **2004**, *132*, 181.

[73] X. Yu, J. Xie, Y. Li, H. Huang, C. Lai, K. Wang, *J. Power Sources* **2005**, *146*, 335.

[74] J. Wang, Y. S. He, J. Yang, *Adv. Mater.* **2015**, *27*, 569.

[75] Y. Wang, L. Xu, M. Wang, W. Pang, X. Ge, *Macromolecules* **2014**, *47*, 3901.

[76] K. Jeddi, K. Sarikhani, N. T. Qazvini, P. Chen, *J. Power Sources* **2014**, *245*, 656.

[77] T. N. L. Doan, M. Ghaznavi, A. Konarov, Y. Zhang, P. Chen, *J. Solid State Electrochem.* **2014**, *18*, 69.

[78] J. Li, K. Li, M. Li, D. Gosselink, Y. Zhang, P. Chen, *J. Power Sources* **2014**, *252*, 107.

[79] A. Konarov, D. Gosselink, T. N. L. Doan, Y. Zhang, Y. Zhao, P. Chen, *J. Power Sources* **2014**, *259*, 183.

[80] J. Wang, L. Yin, H. Jia, H. Yu, Y. He, J. Yang, C. W. Monroe, *ChemSusChem* **2014**, *7*, 563.

[81] S. S. Zhang, *Front. Energy Res.* **2013**, *1*, 1.

[82] Z. Bakenov, Y. Zhang, A. Yermukhambetova, Y. Zhao, P. Chen, *J. Mater. Chem. A* **2012**, *1*, 295.

[83] Z. Q. Jin, Y. G. Liu, W. K. Wang, A. B. Wang, B. W. Hu, M. Shen, T. Gao, P. C. Zhao, Y. S. Yang, *Energy Storage Mater.* **2018**, *14*, 272.

[84] S. S. Zhang, *Energies* **2014**, *7*, 4588.

[85] C. Kim, Q. Wang, N. Subba Reddy, H. Kim, G. B. Cho, J. H. Ahn, K. W. Kim, H. S. Ryu, Y. Kim, S. H. Yeon, H. J. Ahn, *J. Ceram. Process. Res.* **2015**, *16*, 199.

[86] J. Zhou, Y. Guo, C. Liang, L. Cao, H. Pan, J. Yang, J. Wang, *Chem. Commun.* **2018**, *54*, 5478.

[87] H. Liu, J. Holoubek, H. Zhou, A. Chen, N. Chang, Z. Wu, S. Yu, Q. Yan, X. Xing, Y. Li, T. A. Pascal, P. Liu, *Mater. Today* **2020**, *xxx*, 7.

[88] X. Ren, S. Chen, H. Lee, D. Mei, M. H. Engelhard, S. D. Burton, W. Zhao, J. Zheng, Q. Li, M. S. Ding, M. Schroeder, J. Alvarado, K. Xu, Y. S. Meng, J. Liu, J. G. Zhang, W. Xu, *Chem* **2018**, *4*, 1877.

[89] X. B. Cheng, R. Zhang, C. Z. Zhao, Q. Zhang, *Chem. Rev.* **2017**, *117*, 10403.

[90] D. Lin, Y. Liu, Y. Cui, *Nat. Nanotechnol.* **2017**, *12*, 194.

[91] K. Xu, *Chem. Rev.* **2014**, *114*, 11503.

[92] P. Albertus, S. Babinec, S. Litzelman, A. Newman, *Nat. Energy* **2018**, *3*, 16.

[93] A. Mukanova, A. Jetybayeva, S. T. Myung, S. S. Kim, Z. Bakenov, *Mater. Today Energy* **2018**, *9*, 49.

[94] M. Ko, S. Chae, J. Cho, *ChemElectroChem* **2015**, *2*, 1645.

[95] M. Salah, P. Murphy, C. Hall, C. Francis, R. Kerr, M. Fabretto, *J. Power Sources* **2019**, *414*, 48.

[96] T. W. Kwon, J. W. Choi, A. Coskun, *Chem. Soc. Rev.* **2018**, *47*, 2145.

[97] X. Chen, H. Li, Z. Yan, F. Cheng, J. Chen, *Sci. China Mater.* **2019**, *62*, 1515.

[98] W. F. Ren, Y. Zhou, J. T. Li, L. Huang, S. G. Sun, *Curr. Opin. Electrochem.* **2019**, *18*, 46.

[99] Z. Liu, Q. Yu, Y. Zhao, R. He, M. Xu, S. Feng, S. Li, L. Zhou, L. Mai, *Chem. Soc. Rev.* **2019**, *48*, 285.

[100] X. Xiao, P. Liu, M. W. Verbrugge, H. Haftbaradaran, H. Gao, *J. Power Sources* **2011**, *196*, 1409.

[101] W. Lu, L. Zhang, Y. Qin, A. Jansen, *J. Electrochem. Soc.* **2018**, *165*, A2179.

[102] W. An, B. Gao, S. Mei, B. Xiang, J. Fu, L. Wang, Q. Zhang, P. K. Chu, K. Huo, *Nat. Commun.* **2019**, *10*, 1.

[103] Z. Xiao, C. Lei, C. Yu, X. Chen, Z. Zhu, H. Jiang, F. Wei, *Energy Storage Mater.* **2020**, *24*, 565.

[104] Y. He, X. Yu, Y. Wang, H. Li, X. Huang, *Adv. Mater.* **2011**, *23*, 4938.

[105] X. Zuo, J. Zhu, P. Müller-Buschbaum, Y. J. Cheng, *Nano Energy* **2017**, *31*, 113.

[106] Y. Zhang, N. Du, D. Yang, *Nanoscale* **2019**, *11*, 19086.

[107] G. Berckmans, L. De Sutter, M. Marinaro, J. Smekens, J. Jaguemont, M. Wohlfahrt-Mehrens, J. van Mierlo, N. Omar, *Electrochim. Acta* **2019**, *306*, 387.

[108] S. Martinet, *Nanosci. Technol.* **2016**, 471.

[109] H. Wu, Y. Cui, *Nano Today* **2012**, *7*, 414.

[110] R. Teki, R. Krishnan, T. C. Parker, T. M. Lu, M. K. Datta, P. N. Kumta, N. Koratkar, *Small* **2009**, *5*, 2236.

[111] U. Kasavajjula, C. Wang, A. J. Appleby, *J. Power Sources* **2007**, *163*, 1003.

[112] S. K. Soni, B. W. Sheldon, X. Xiao, M. W. Verbrugge, A. Dongjoon, H. H., G. Huajian, *J. Electrochem. Soc.* **2011**, *159*, A38.

[113] V. A. Sethuraman, M. J. Chon, M. Shimshak, V. Srinivasan, P. R. Guduru, *J. Power Sources* **2010**, *195*, 5062.

[114] B. Peng, F. Cheng, Z. Tao, J. Chen, *J. Chem. Phys.* **2010**, *133*.

[115] T. L. Kulova, A. M. Skundin, Y. V. Pleskov, E. I. Terukov, O. I. Kon'kov, *J. Electroanal. Chem.* **2007**, *600*, 217.

[116] K. Kalaga, M. T. F. Rodrigues, S. E. Trask, I. A. Shkrob, D. P. Abraham, *Electrochim. Acta* **2018**, *280*, 221.

[117] H. Liu, X. Yue, X. Xing, Q. Yan, J. Huang, V. Petrova, H. Zhou, P. Liu, *Energy Storage Mater.* **2019**, *16*, 505.

[118] H. Liu, X. Wang, H. Zhou, Q. Yan, H.-D. Lim, X. Xing, Y. S. Meng, P. Liu, *ACS Appl. Energy Mater.* **2018**, *1*, 1864.

[119] Y. J. Nam, D. Y. Oh, S. H. Jung, Y. S. Jung, *J. Power Sources* **2018**, *375*, 93.

[120] X. B. Cheng, R. Zhang, C. Z. Zhao, F. Wei, J. G. Zhang, Q. Zhang, *Adv. Sci.* **2015**,

3, 1.

[121] Y. Zhu, Y. Qian, **2015**, *8*.

[122] J. T. Lee, Y. Zhao, H. Kim, W. Il Cho, G. Yushin, *J. Power Sources* **2014**, *248*, 752.

[123] C. Yang, L. Zhang, B. Liu, S. Xu, T. Hamann, D. McOwen, J. Dai, W. Luo, Y. Gong, E. D. Wachsman, L. Hu, *Proc. Natl. Acad. Sci. U. S. A.* **2018**, *115*, 3770.

[124] Y. Q. Li, J. C. Li, X. Y. Lang, Z. Wen, W. T. Zheng, Q. Jiang, *Adv. Funct. Mater.* **2017**, *27*, 1.

[125] B. Liu, L. Zhang, S. Xu, D. W. McOwen, Y. Gong, C. Yang, G. R. Pastel, H. Xie, K. Fu, J. Dai, C. Chen, E. D. Wachsman, L. Hu, *Energy Storage Mater.* **2018**, *14*, 376.

[126] J. A. Lewis, F. J. Q. Cortes, M. G. Boebinger, J. Tippens, T. S. Marchese, N. Kondekar, X. Liu, M. Chi, M. T. McDowell, *ACS Energy Lett.* **2019**, *4*, 591.

[127] W. Zhang, D. Schröder, T. Arlt, I. Manke, R. Koerver, R. Pinedo, D. A. Weber, J. Sann, W. G. Zeier, J. Janek, *J. Mater. Chem. A* **2017**, *5*, 9929.

[128] L. Porz, T. Swamy, B. W. Sheldon, D. Rettenwander, T. Frömling, H. L. Thaman, S. Berendts, R. Uecker, W. C. Carter, Y. M. Chiang, *Adv. Energy Mater.* **2017**, *7*, 1.

[129] Y. J. Nam, K. H. Park, D. Y. Oh, W. H. An, Y. S. Jung, *J. Mater. Chem. A* **2018**, *6*, 14867.

[130] Y. Song, L. Yang, W. Zhao, Z. Wang, Y. Zhao, Z. Wang, Q. Zhao, H. Liu, F. Pan, *Adv. Energy Mater.* **2019**, *9*, 1.

[131] T. Yersak, J. R. Salvador, R. D. Schmidt, M. Cai, *ACS Appl. Energy Mater.* **2019**, *2*, 3523.

[132] H. Ye, S. Xin, Y. X. Yin, J. Y. Li, Y. G. Guo, L. J. Wan, *J. Am. Chem. Soc.* **2017**, *139*, 5916.

[133] T. Yoshinari, R. Koerver, P. Hofmann, Y. Uchimoto, W. G. Zeier, J. Janek, *ACS Appl. Mater. Interfaces* **2019**, *11*, 23244.

[134] N. Riphaus, B. Stiaszny, H. Beyer, S. Indris, H. A. Gasteiger, S. J. Sedlmaier, *J. Electrochem. Soc.* **2019**, *166*, A975.

[135] J. Duan, W. Wu, A. M. Nolan, T. Wang, J. Wen, C. Hu, Y. Mo, W. Luo, Y. Huang,

Adv. Mater. **2019**, *31*, 1.

[136] S. Wenzel, S. J. Sedlmaier, C. Dietrich, W. G. Zeier, J. Janek, *Solid State Ionics* **2018**, *318*, 102.

[137] K. Tantratian, D. Cao, A. Abdelaziz, X. Sun, J. Sheng, A. Natan, L. Chen, H. Zhu, *Adv. Energy Mater.* **2020**, *10*, 1.

[138] M. Cengiz, H. Oh, S.-H. Lee, *J. Electrochem. Soc.* **2019**, *166*, A3997.

[139] D. Cao, X. Sun, Q. Li, A. Natan, P. Xiang, H. Zhu, *Matter* **2020**, *3*, 57.

[140] Y. Chen, Z. Wang, X. Li, X. Yao, C. Wang, Y. Li, W. Xue, D. Yu, S. Y. Kim, F. Yang, A. Kushima, G. Zhang, H. Huang, N. Wu, Y. W. Mai, J. B. Goodenough, J. Li, *Nature* **2020**, *578*, 251.

[141] X. Li, L. Jin, D. Song, H. Zhang, X. Shi, Z. Wang, L. Zhang, L. Zhu, *J. Energy Chem.* **2020**, *40*, 39.

[142] F. Han, A. S. Westover, J. Yue, X. Fan, F. Wang, M. Chi, D. N. Leonard, N. J. Dudney, H. Wang, C. Wang, *Nat. Energy* **2019**, *4*, 187.

[143] S. Xu, D. W. McOwen, C. Wang, L. Zhang, W. Luo, C. Chen, Y. Li, Y. Gong, J. Dai, Y. Kuang, C. Yang, T. R. Hamann, E. D. Wachsman, L. Hu, *Nano Lett.* **2018**, *18*, 3926.

[144] K. N. Wood, K. X. Steirer, S. E. Hafner, C. Ban, S. Santhanagopalan, S. H. Lee, G. Teeter, *Nat. Commun.* **2018**, *9*, 1.

[145] H. Liu, X. Yue, X. Xing, Q. Yan, J. Huang, V. Petrova, H. Zhou, P. Liu, *Energy Storage Mater.* **2019**, *16*, 505.

[146] Y. Zhang, B. Liu, E. Hitz, W. Luo, Y. Yao, Y. Li, J. Dai, C. Chen, Y. Wang, C. Yang, H. Li, L. Hu, *Nano Res.* **2017**, *10*, 1356.

[147] Q. Zhang, D. Cao, Y. Ma, A. Natan, P. Aurora, H. Zhu, *Adv. Mater.* **2019**, *31*, 1.

[148] K. H. Park, Q. Bai, D. H. Kim, D. Y. Oh, Y. Zhu, Y. Mo, Y. S. Jung, *Adv. Energy Mater.* **2018**, *8*, 1.

[149] J. Duan, Y. Zheng, W. Luo, W. Wu, T. Wang, Y. Xie, S. Li, J. Li, Y. Huang, *Natl. Sci. Rev.* **2020**, *7*, 1208.

[150] Z. Liang, D. Lin, J. Zhao, Z. Lu, Y. Liu, C. Liu, Y. Lu, H. Wang, K. Yan, X. Tao, Y. Cui, *Proc. Natl. Acad. Sci. U. S. A.* **2016**, *113*, 2862.

[151] H. D. Lim, X. Yue, X. Xing, V. Petrova, M. Gonzalez, H. Liu, P. Liu, *J. Mater. Chem. A* **2018**, *6*, 7370.

[152] L. Höltschi, F. Jud, C. Borca, T. Huthwelker, C. Villevieille, V. Pelé, C. Jordy, M. El Kazzi, P. Novák, *J. Electrochem. Soc.* **2020**, *167*, 110558.

[153] F. Han, J. Yue, X. Zhu, C. Wang, *Adv. Energy Mater.* **2018**, *8*, 6.

[154] N. Zhang, X. Long, Z. Wang, P. Yu, F. Han, J. Fu, G. Ren, Y. Wu, S. Zheng, W. Huang, C. Wang, H. Li, X. Liu, *ACS Appl. Energy Mater.* **2018**, *1*, 5968.

[155] P. J. Cumpson, *J. Electron Spectros. Relat. Phenomena* **1995**, *73*, 25.

[156] P. Shi, T. Li, R. Zhang, X. Shen, X. B. Cheng, R. Xu, J. Q. Huang, X. R. Chen, H. Liu, Q. Zhang, *Adv. Mater.* **2019**, *31*, 1.

[157] L. Xu, S. Tang, Y. Cheng, K. Wang, J. Liang, C. Liu, Y. C. Cao, F. Wei, L. Mai, *Joule* **2018**, *2*, 1991.

[158] J. Huang, *Electrochim. Acta* **2018**, *281*, 170.

[159] T. Krauskopf, H. Hartmann, W. G. Zeier, J. Janek, *ACS Appl. Mater. Interfaces* **2019**, *11*, 14463.

[160] W. Li, H. Yao, K. Yan, G. Zheng, Z. Liang, Y. M. Chiang, Y. Cui, *Nat. Commun.* **2015**, *6*, 1.

[161] F. Xin, H. Zhou, X. Chen, M. Zuba, N. Chernova, G. Zhou, M. S. Whittingham, *ACS Appl. Mater. Interfaces* **2019**, *11*, 34889.

[162] N. Özer, C. M. Lampert, *Sol. Energy Mater. Sol. Cells* **1995**, *39*, 367.

[163] M. I. Yanovskaya, E. P. Turevskaya, A. P. Leonov, S. A. Ivanov, N. V. Kolganova, S. Y. Stefanovich, N. Y. Turova, Y. N. Venevtsev, *J. Mater. Sci.* **1988**, *23*, 395.

[164] C. N. Taylor, J. Dadras, K. E. Luitjohan, J. P. Allain, P. S. Krstic, C. H. Skinner, *J. Appl. Phys.* **2013**, *114*.

[165] A. Manthiram, Y. Fu, S. H. Chung, C. Zu, Y. S. Su, *Chem. Rev.* **2014**, *114*, 11751.

[166] S. Xiong, K. Xie, Y. Diao, X. Hong, *J. Power Sources* **2014**, *246*, 840.

[167] S. S. Zhang, *J. Power Sources* **2016**, *322*, 99.

[168] S. S. Zhang, *Electrochim. Acta* **2012**, *70*, 344.

[169] S. Wei, L. Ma, K. E. Hendrickson, Z. Tu, L. A. Archer, *J. Am. Chem. Soc.* **2015**, *137*, 12143.

[170] J. Wang, Y. Guo, J. Yang, J. Zhou, Y. Nuli, Z. Chen, C. Liang, *Electrochim. Acta* **2018**, *282*, 555.

[171] W. Wang, Z. Cao, G. A. Elia, Y. Wu, W. Wahyudi, E. Abou-Hamad, A. H. Emwas, L. Cavallo, L. J. Li, J. Ming, *ACS Energy Lett.* **2018**, *3*, 2899.

[172] R. K. Zenn, K. Müller, S. Warneke, M. Frey, R. E. Dinnebier, M. R. Buchmeiser, A. Hintennach, *ACS Energy Lett.* **2017**, *2*, 595.

[173] J. T. Lee, Y. Zhao, S. Thieme, H. Kim, M. Oschatz, L. Borchardt, A. Magasinski, W. Il Cho, S. Kaskel, G. Yushin, *Adv. Mater.* **2013**, *25*, 4573.

[174] L. Suo, Y. S. Hu, H. Li, M. Armand, L. Chen, *Nat. Commun.* **2013**, *4*, 1.

[175] R. Miao, J. Yang, Z. Xu, J. Wang, Y. Nuli, L. Sun, *Sci. Rep.* **2016**, *6*, 2.

[176] S. Ma, P. Zuo, H. Zhang, Z. Yu, C. Cui, M. He, G. Yin, **2019**, 5267.

[177] X. Chen, L. Peng, L. Wang, J. Yang, Z. Hao, J. Xiang, K. Yuan, Y. Huang, B. Shan, L. Yuan, J. Xie, *Nat. Commun.* 1.

[178] K. Yan, Z. Lu, H. W. Lee, F. Xiong, P. C. Hsu, Y. Li, J. Zhao, S. Chu, Y. Cui, *Nat. Energy* **2016**, *1*.

[179] W. Li, H. Yao, K. Yan, G. Zheng, Z. Liang, Y. M. Chiang, Y. Cui, *Nat. Commun.* **2015**, *6*, 1.

[180] H. Liu, H. Zhou, B. S. Lee, X. Xing, M. Gonzalez, P. Liu, *ACS Appl. Mater. Interfaces* **2017**, *9*, 30635.

[181] B. D. Adams, E. V. Carino, J. G. Connell, K. S. Han, R. Cao, J. Chen, J. Zheng, Q. Li, K. T. Mueller, W. A. Henderson, J. G. Zhang, *Nano Energy* **2017**, *40*, 607.

[182] S. W. Chien, M. B. Sullivan, M.-F. Ng, C. Zhou, Z. Liu, T. S. A. Hor, A. Yu, L. Zhou, D. Geng, Y. Zong, N. Ding, J. Yang, *Sci. Rep.* **2016**, *6*, 1.

[183] E. S. Science, **2020**, *2020*, 7.

[184] J. Li, A. K. Dozier, Y. Li, F. Yang, Y.-T. Cheng, *J. Electrochem. Soc.* **2011**, *158*, A689.

[185] H. Liu, Z. Zhu, Q. Yan, S. Yu, X. He, Y. Chen, R. Zhang, L. Ma, T. Liu, M. Li, R. Lin, Y. Chen, Y. Li, X. Xing, Y. Choi, L. Gao, H. S. yun Cho, K. An, J. Feng, R. Kostecki, K. Amine, T. Wu, J. Lu, H. L. Xin, S. P. Ong, P. Liu, *Nature* **2020**, *585*, 63.